300
5-16-80

Dr. 1514

AMORPHOUS THIN FILMS FOR SOLAR-CELL APPLICATIONS

Final Report for September 11, 1978—September 10, 1979

By
D. E. Carlson          J. I. Pankove
I. Balberg             D. L. Staebler
R. S. Crandall         H. A. Weakliem
B. Goldstein           R. Williams
J. J. Hanak

February 1980

Work Performed Under Contract No. AC03-78ET21074

MASTER

RCA Laboratories
Princeton, New Jersey
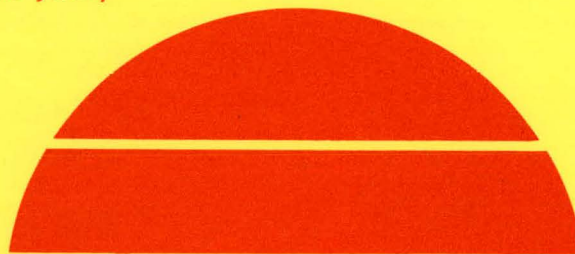
# U.S. Department of Energy

**Solar Energy**

## DISCLAIMER

This report was prepared as an account of work sponsored by an agency of the United States Government. Neither the United States Government nor any agency Thereof, nor any of their employees, makes any warranty, express or implied, or assumes any legal liability or responsibility for the accuracy, completeness, or usefulness of any information, apparatus, product, or process disclosed, or represents that its use would not infringe privately owned rights. Reference herein to any specific commercial product, process, or service by trade name, trademark, manufacturer, or otherwise does not necessarily constitute or imply its endorsement, recommendation, or favoring by the United States Government or any agency thereof. The views and opinions of authors expressed herein do not necessarily state or reflect those of the United States Government or any agency thereof.

# DISCLAIMER

**Portions of this document may be illegible in electronic image products. Images are produced from the best available original document.**

# AMORPHOUS THIN FILMS FOR SOLAR-CELL APPLICATIONS

D.E. Carlson
I. Balberg
R.S. Crandall
B. Goldstein
J.J. Hanak
J.I. Pankove
D.L. Staebler
H.A. Weakliem
R. Williams

RCA Laboratories
Princeton, New Jersey  08540

FEBRUARY 1980

## FINAL REPORT

For the Period 11 September 1978 to 10 September 1979

C, L,

THIS PAGE

WAS INTENTIONALLY

LEFT BLANK

## PREFACE

This Final Report covers the work performed by the Display and Energy Systems Research Laboratory of RCA Laboratories, Princeton, New Jersey, for the period 11 September 1978 to 10 September 1979 under Contract No. AC03-78-ET-21074. The Laboratory Director is B. F Williams; D. E. Carlson is the Group Head and Project Scientist. The staff members and associate staff personnel who have contributed to the report and their areas of specialization are listed below.

| | |
|---|---|
| D. E. Carlson<br>R. W. Smith | ac and dc Deposition of a-Si:H;<br>Pd-Schottky-Barrier Cells |
| *I. Balberg | Tunneling Studies |
| *R. S. Crandall<br>B. E. Tompkins | Photoconductive Gain, Electron Trapping, Field-Dependent Quantum Efficiency |
| *J. Dresner | Hall Effect, dc Deposition of a-Si:H |
| *B. Goldstein<br>D. J. Szostak | Surface Studies |
| †J. J. Hanak<br>J. P. Pellicane<br>V. Korsun | rf Deposition of a-Si:H; Solar Cell Structures |
| *A. R. Moore | Photoelectromagnetic Effect |
| †J. I. Pankove<br>J. E. Berkeyheiser | Photoluminescence, Ion Implantation, Photoconductivity |
| *D. L. Staebler<br>G. R. Latham | Hole Diffusion Length |
| *H. A. Weakliem<br>A. V. Cafiero | rf Magnetron Deposition of a-Si:H, Mass Spectroscopy |
| †R. Williams | Device Modeling |

The RCA report number is PRRL-79-CR-47.

THIS PAGE

WAS INTENTIONALLY

LEFT BLANK

# ABSTRACT

This Final Report describes work performed at RCA Laboratories, Princeton, NJ, on the five research tasks of the present contract. In Section II, Theoretical Modeling, we present theories for the capture of electrons by deep centers in hydrogenated amorphous silicon (a-Si:H) and for field-dependent quantum efficiency in a-Si:H.

In Section III, Deposition and Doping Studies, we describe the optimization of phosphorus-doped a-Si:H carried out in four different discharge systems. Some details of the dc proximity and rf magnetron discharge systems are also provided. Preliminary mass spectroscopy studies of the rf magnetron discharge in both $SiH_4$ and $SiF_4$ are presented.

In Section IV, Experimental Methods for Characterizing a-Si:H, we present recent work involving photoluminescence of fluorine-doped a-Si:H, photoconductivity spectra, the photoelectromagnetic effect, the photo-Hall effect and tunneling into a-Si:H. We also describe studies of the growth mechanism of Pt adsorbed on both crystalline Si and a-Si:H. Measurements of the surface photovoltage have been used to estimate the distribution of surface states on phosphorus-doped and undoped a-Si:H.

Section V, Formation of Solar-Cell Structures, contains information on stacked or multiple-junction a-Si:H solar cells. We also describe a series of material studies for the optimization of a p-i-n solar-cell structure.

In Section VI, Theoretical and Experimental Evaluation of Solar-Cell Parameters, an upper limit of $\sim 400$ Å is established for the hole diffusion length in undoped a-Si:H. We also present a detailed description of carrier generation, recombination and transport in a-Si:H solar cells. Finally, we describe some characteristics of Pd-Schottky-barrier cells for different processing histories.

TABLE OF CONTENTS

# LIST OF ILLUSTRATIONS

LIST OF ILLUSTRATIONS (Continued)

LIST OF ILLUSTRATIONS (Continued)

LIST OF TABLES

# SECTION I

## INTRODUCTION

This report reviews the research performed on amorphous-silicon solar cells at RCA Laboratories Princeton, NJ, over the period September 11, 1978 to September 10, 1979.

Hydrogenated amorphous silicon (a-Si:H) was first studied by Chittick et al. in 1969 [1]. The material was made in an rf electrodeless discharge in silane ($SiH_4$) at pressures of ~1 Torr. The authors had observed a strong dependence of resistivity on substrate temperature and also a photoconductivity much larger than that observed in evaporated amorphous silicon. They also reported some preliminary data indicating that their material could be substitutionally doped with phosphorus by adding small amounts of phosphine ($PH_3$) to the discharge atmosphere.

Subsequently, many of the properties of discharge-produced amorphous silicon were measured by researchers at the University of Dundee in Scotland. These investigators measured the drift mobility of electrons [2], the density of gap states [3], the Hall effect [4], and the thermoelectric power [5]. They also performed a detailed study of the substitutional doping of a-Si:H by adding $B_2H_6$ and $PH_3$ to the discharge atmosphere [6]. Recently, several investigators [7-9] have shown that discharge-produced amorphous silicon contains between 10 and 50 at. % of hydrogen. The hydrogen apparently compensates dangling bonds that would otherwise give rise to localized states in the gap.

1.  R. C. Chittick, J. H. Alexander, and H. F. Sterling, J. Electrochem. Soc. 116, 77 (1969).
2.  P. G. LeComber and W. E. Spear, Phys. Rev. Lett. 25, 509 (1970).
3.  W. E. Spear and P. G. LeComber, J. Non-Cryst. Solids 8-10, 727 (1972).
4.  P. G. LeComber, D. I. Jones, and W. E. Spear, Philos, Mag. 35, 1173 (1977).
5.  D. I. Jones, P. G. LeComber, and W. E. Spear, Philos, Mag. 36, 541 (1977).
6.  W. E. Spear and P. G. LeComber, Solid State Commun. 17, 1193 (1975).
7.  A. Triska, D. Dennison, and H. Fritzsche, Bull. Am. Phys. Soc. 20, 392 (1975).
8.  M. H. Brodsky, M. A. Frisch, J. F. Ziegler, and W. A. Lanford, Appl. Phys. Lett. 30, 561 (1977).
9.  J. I. Pankove and D. E. Carlson, Appl. Phys. Lett. 31, 450 (1977).

The first a-Si:H electronic devices were made at RCA Laboratories in 1974 [10,11].  Rectification and photovoltaic energy conversion were observed in several types of devices such as p-n, p-i-n, and Schottky-barrier junctions as well as heterojunctions.  This work showed that substitutional doping could be used to make junctions in a-Si:H as well as ohmic contacts to various metals.  Investigators at RCA Laboratories [12] have also observed electroluminescence in p-i-n and Schottky-barrier cells.  The best conversion efficiencies obtained to date in a-Si:H solar cells are ~5.5% for small area devices (~1.5 mm$^2$) [13] and 3.2% for large-area devices (>1 cm$^2$).

The present program for studying a-Si:H for solar-cell applications involves five tasks:  theoretical modeling, deposition and doping studies, experimental methods for the characterization of a-Si:H, formation of solar-cell structures, and theoretical and experimental evaluation of solar-cell parameters.

10.  D. E. Carlson, U.S. Pat. 4,064,521 (1977).
11.  D. E. Carlson and C. R. Wronski, Appl. Phys. Lett. 28, 671 (1976).
12.  J. I. Pankove and D. E. Carlson, Appl. Phys. Lett. 39, 620 (1976).
13.  D. E. Carlson, IEEE Trans. Electron Devices ED-24, 449 (1977).

## SECTION II

## THEORETICAL MODELING

### A. ELECTRON CAPTURE BY DEEP CENTERS IN a-Si:H

Measurements of deep-trap parameters in single-crystal silicon p-n junctions or barrier devices have been made by a variety of techniques. The most notable is the transient capacitance technique, in which the response of the depletion width to charge injection or extraction is monitored by a fast capacitance bridge [14]. Using this technique one can determine trap parameters such as capture cross section, density, and energy level. However, this technique requires that the depletion width is determined by the occupancy of the deep traps rather than the shallow traps. In amorphous silicon the opposite situation prevails. The shallow traps determine the depletion width. This occurs because the shallow states are in much greater number than the deep states [15]. Thus, a measurement of the depletion width does not readily give information on the deep traps. Furthermore, the characteristic time for the depletion width changes are on the order of the drift transit time which is too short for existing capacitive measurement techniques [16].

Nevertheless, one can obtain useful deep-trap parameters using transient current techniques. This approach has been successfully used to measure deep-interface traps in single-crystal silicon devices [17]. In this technique an injecting pulse fills the traps and then the current is monitored during an extraction current plus. In the extraction phase the cathode is a blocking contact. Therefore, the only current is due to the release of charge from deep traps.

The measurement sequence to be described here for an n-type a-Si:H Schottky-barrier device can be equally well applied to p-i-n or other device

14. D. V. Lang, J. Appl. Phys. 45, 3023 (1974).
15. W. E. Spear and P. G. LeComber, Philos. Mag. 33, 935 (1976).
16. R. S. Crandall, submitted for publication.
17. J. S. Uranwala, T. G. Simmons and H. A. Mar, Solid-State Electron. 19, 375 (1976).

structures. The only restriction is that the contacts must be blocking in one polarity. Figures 1(a) to 1(c) show the changes in the electron potential energy as the device goes through a measurement cycle. Initially, the barrier metal ($M_1$) is biased negative with respect to the contact metal ($M_2$). This reverse bias of magnitude $V_A$ establishes a depletion width ($\ell$) uncovering positive space charge of density $N_S$. These quantities are related by the usual expression [18].

$$\ell^2 = \frac{2\varepsilon_s}{eN_S} \left( V_B - \frac{kT}{e} \right) \tag{1}$$

where $\varepsilon_s$ is the static dielectric constant, T the temperature, k Boltzmann's constant, e the magnitude of the electron charge and $V_B$ the potential difference between the top of Schottky barrier and the metal $M_2$. It is given by

$$V_B = V_B^o + V_A \tag{2}$$

where $V_B^o$ is the built-in potential. In Fig. 1 (b) a forward-bias pulse $\Delta V$ is applied for a time ($t_p$) such that $V_B = V_B^o + V_A - \Delta V$ decreasing $\ell$ by an amount $\Delta\ell$; $\ell' = \ell - \Delta\ell$. Electrons have entered the silicon from the contact $M_2$ and neutralized the positive space charge in the region between $\ell$ and $\ell - \Delta\ell$. In Fig. 1(c) the voltage $\Delta V$ has been removed and electrons in shallow traps have left the material in a time the order of the transit time. Because their number is on the order of the positive space charge, the depletion width widens to its original value, $\ell$. However, the deep traps still contain electrons depicted by circles drawn about the + charges. Because their number is small compared with $N_S$ they do not significantly affect the magnitude of the positive space charge nor the potential distribution. In time, deeper and deeper traps empty, contributing to the current.

Figure 2 shows the current and voltage for the sequence depicted in Fig. 1. During the time interval $t_p$ the Schottky barrier decreases to $\ell'$ and negative charge is available for capture by deep as well as shallow traps. The injected current decays as these traps fill. When the pulse is

---

18. S. M. Sze, <u>Physics of Semiconductor Devices</u> (Wiley Interscience, New York, 1969).
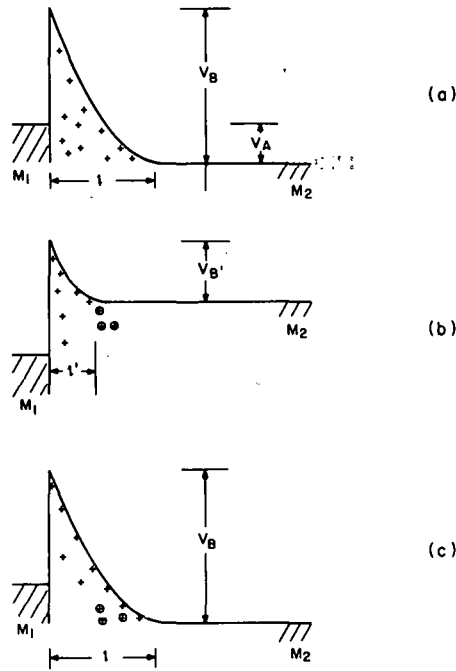
Figure 1. Electron potential energy as a function of thickness in an a-Si:H Schottky-barrier cell. $V_B$ is the potential difference between the top of the barrier and the back metal contact; $M_1$ and $M_2$ are metal contacts. +++ positive space charge; ⊕ ⊕ neutralized space charge. $V_A$ is the applied voltage. $\ell$ is the depletion width.

terminated, the shallow traps empty and the injected charge leaves in a time, $t_1$, the order of the transit time. The charge leaving in $t_1$ is about 99% of the injected charge. The dynamics of this process will be described in a forthcoming article [16]. At later times t charge still flows due to the emptying of deep traps. This current is measured in order to study parameters of these deep traps. The characteristics time $(\tau(\varepsilon))$ for a trap of a given energy $(\varepsilon)$ below the conduction band to empty is given by

$$\frac{1}{\tau(\varepsilon)} = \upsilon \, \exp \, (-\varepsilon/kT) \tag{3}$$

where $\upsilon$ is an attempt to escape frequency. This expression shows that deeper traps empty much slower than shallow ones and that their contribution to the current comes at progressively later times after the injecting pulse terminates.
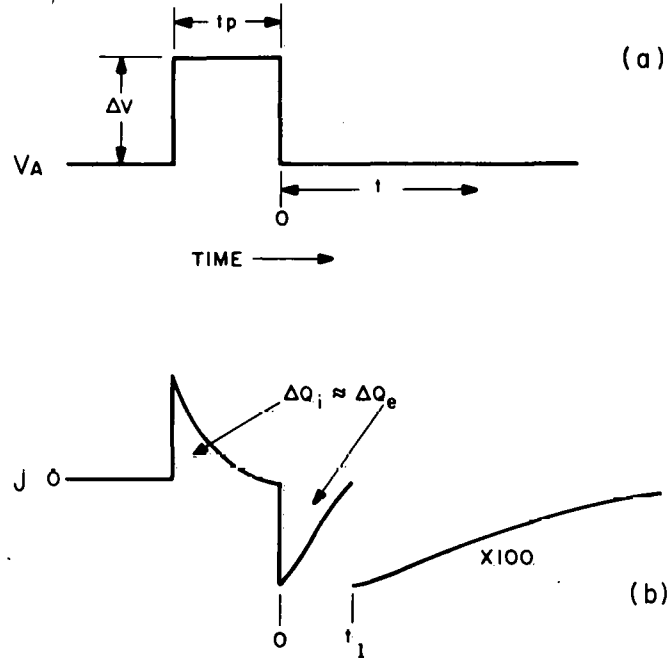
Figure 2. (a) Time sequence of the voltage applied to the device in Fig. 1.
$V_A$ is a dc reverse-bias voltage. $\Delta V$ is a voltage pulse applied in
the forward direction reducing the magnitude of the reverse bias for
a time $t_p$. (b) The current flow in the external circuit in conjunc-
tion with the voltage sequence in (a). During $t_p$ electrons are in-
jected into the region $\ell-\Delta\ell$ to neutralize the positive space charge.
During $t_p$ most of these are removed. The area under the curve during
$t_p$ is about equal to the area under the curve $0{\to}t_1$. The difference
represents charge in deep traps that comes out at later times.


The current density (J(t)) due to trap emptying is given by

$$J(t) = \frac{1}{2} \sum \frac{dQ(\varepsilon)}{dt} \qquad (4)$$

where t is the time after the termination of the injection pulse, and $dQ(\varepsilon)/dt$
is the time rate of charge of the number of electron charges per $cm^2$ trapped
at an energy $\varepsilon$. The summation is overall energy levels. It is asssumed that
once a trapped charge is thermally excited to the conduction band it is col-
lected in the external circuit; i.e., no recombination. This is reasonable
because the trapping time is much longer than the transit time so that a
carrier leaves the junction before it is recaptured. The factor of 1/2
arises because the charge is released uniformly in the bulk.

6

Under these conditions the rate equation for the fractional occupancy ($f(\varepsilon)$) of electrons trapped at an energy $\varepsilon$ is

$$\frac{df(\varepsilon)}{dt} = - f(\varepsilon)/\tau(\varepsilon) \tag{5}$$

With the initial condition that $f(\varepsilon) = f^\circ(\varepsilon)$ at $t = 0$, the solution of this equation is

$$f(\varepsilon) = f^\circ(\varepsilon) \exp [-t/\tau(\varepsilon)] \tag{6}$$

The charge $Q(\varepsilon)$ is related to $f(\varepsilon)$ by the density of states per unit energy ($N(\varepsilon)$). Therefore,

$$Q(\varepsilon) = e\, f(\varepsilon)\, N(\varepsilon)\, \Delta\ell \tag{7a}$$

and

$$\frac{dQ(\varepsilon)}{dt} = \Delta\ell e\, N(\varepsilon)\, f^\circ(\varepsilon)\, \frac{\exp [-t/\tau(\varepsilon)]}{t(\varepsilon)} \tag{7b}$$

Substituting Eq. (7b) into Eq. (4) and converting the summation into an integration over energy gives

$$J(t) = \frac{e\,\Delta\ell}{2} \int \frac{f^\circ(\varepsilon)\, N(\varepsilon)}{\tau(\varepsilon)} \exp [-t/\tau(\varepsilon)]\, d\varepsilon \tag{8}$$

Because $\exp [(-t/\tau(\varepsilon)]/\tau(\varepsilon)$ is a strongly peaked function of energy, the integral in Eq. (8) can be approximate by treating this function as a delta function [6]. Then, Eq. (8) becomes

$$J(t) = \frac{e\Delta\ell}{2} f^\circ(\varepsilon_o) \frac{N(\varepsilon_o)\, kT}{t} = \frac{1}{2} \frac{n(\varepsilon_o)}{t} e\Delta\ell\, kT \tag{9}$$

where $n(\varepsilon_o)$ is the number per unit volume per unit energy of electrons trapped at an energy $\varepsilon_o$. The energy $\varepsilon_o$ is given by

$$\varepsilon_o = kT \ell n\, (\upsilon t). \tag{10}$$

Using Eqs. (9) and (10), the current at different times can be used as a probe of the density of electrons trapped over the energy range given by Eq. (10). Furthermore, if the state at energy $\varepsilon_o$ is completely filled with electrons at $t = 0$, then $n(\varepsilon_o)$ is equal to the density of states and this technique can be used to map out the density of states. Unfortunately, $\upsilon$ must be determined from additional measurements or the energy scale is uncertain by an amount $kT \ell n(\upsilon)$.

To obtain a value for $\upsilon$ it is necessary to measure the rate of capture of electrons into the state $\varepsilon_o$. Then $\upsilon$ can be related to this rate through detailed balance. This can be done by measuring $n(\varepsilon_o)$ as a function of $t_p$, the length of the injecting pulse. This becomes apparent by considering the

7

following situation where the bias is changed by $\Delta V$ so that charge flows into the film and electrons enter the region $\Delta \ell$. Neglecting thermal excitation, the time rate of change of the density of trapped electrons is

$$\frac{dn(\varepsilon)}{dt_p} = n_c \, \beta(\varepsilon) \, N(\varepsilon) \, [(1 - f(\varepsilon)] \qquad (11)$$

where $n_c$ is the density of conduction band electrons and $\beta(\varepsilon) \, N(\varepsilon) = W(\varepsilon)$ is the probability of transition from the conduction band into the state at energy $\varepsilon$. The function $[1-f(\varepsilon)]$ assures that transitions are made only into empty states. The solution of Eq. (11) is

$$n(\varepsilon) = N(\varepsilon)[1 - \exp\,(-t_p/\tau_a)] \qquad (12)$$

where

$$\frac{1}{\tau_a} = n_c \beta(\varepsilon) \qquad (13)$$

In principle, then, a measurement of $n(\varepsilon)$, using Eq. (9), for different $t_p$ allows a determination of $\tau_a$ and $N(\varepsilon)$. Since $n_c$ is known, $\beta(\varepsilon)$ can be determined from $\tau_a$. Detailed balance then connects $\upsilon$ to $\beta(E)$ through the conduction band density of states $n_c$; i.e.,

$$\upsilon = n_n \, \beta(\varepsilon) \qquad (14)$$

so that the energy scale, using Eq. (10), can be determined.

The current $J(t)$ at different times is most easily measured using a gated amplifier. Then, repetitive pulses can be used and signal-averaging techniques can be applied. The time gate width is kept small for good time resolution.

In Fig. 3, $n(\varepsilon_o)$ using Eq. (9) is plotted versus $(\Delta Q)$, the charge injected during the forward-voltage pulse $\Delta V$. For this $\Delta Q = \int J(t_p)dt_p$. These data are for an a-Si:H film doped with $PH_3/SiH_4 = 2\text{x}10^{-3}$ in the gas phase. The Schottky barrier is platinum and the film is 1.6 $\mu$m thick. For a long injecting pulse $(t_p - 5 \,\mu s)$, the current increases until saturation at about $4\text{x}10^{-8}$C injected charge. The charge is changed by varying the voltage $\Delta V$. The voltage at which $n(\varepsilon_o)$ saturates corresponds to the voltage at which the Schottky barrier collapses ($\Delta \ell = \ell$). With further increase in voltage the additional charge flows through the film and is not trapped. If $t_p$ is short, not enough charge is injected to fill the state and $n(\varepsilon_o)$ increases with increasing $\Delta Q$, even though the voltage is high enough to collapse the depletion width. This is shown by the data for $t_p = 0.5 \,\mu s$.

In Fig. 4, $n(\varepsilon_o)$ is plotted vs the length of the injecting pulse $t_p$. The data are for the same sample as in Fig. 3. For these data $\Delta V$ is such
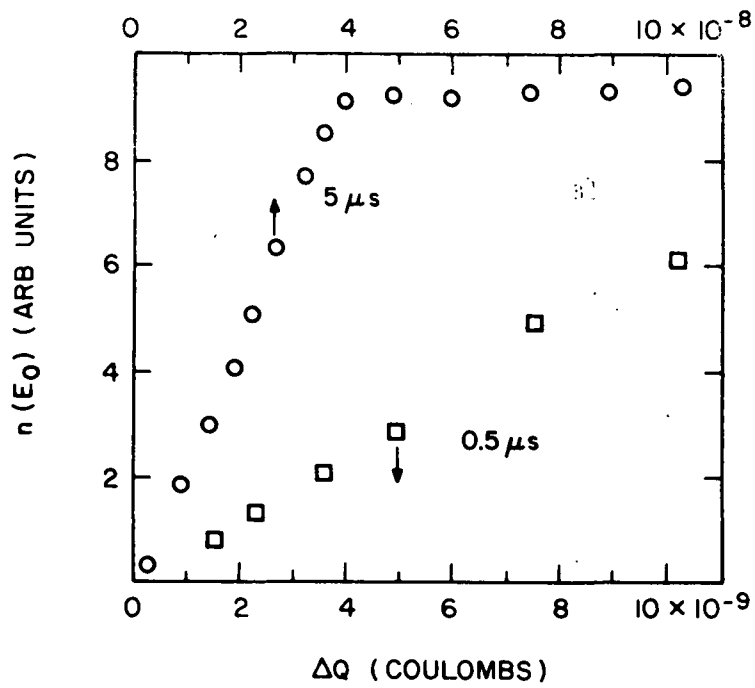
Figure 3. The density of trapped charge $n(\varepsilon_o)$ vs the injected charge $\Delta Q$ for a phosphorus-doped sample. $\Delta Q$ is varied by changing the voltage $\Delta V$. The times in the figure are the length of the injecting pulse.
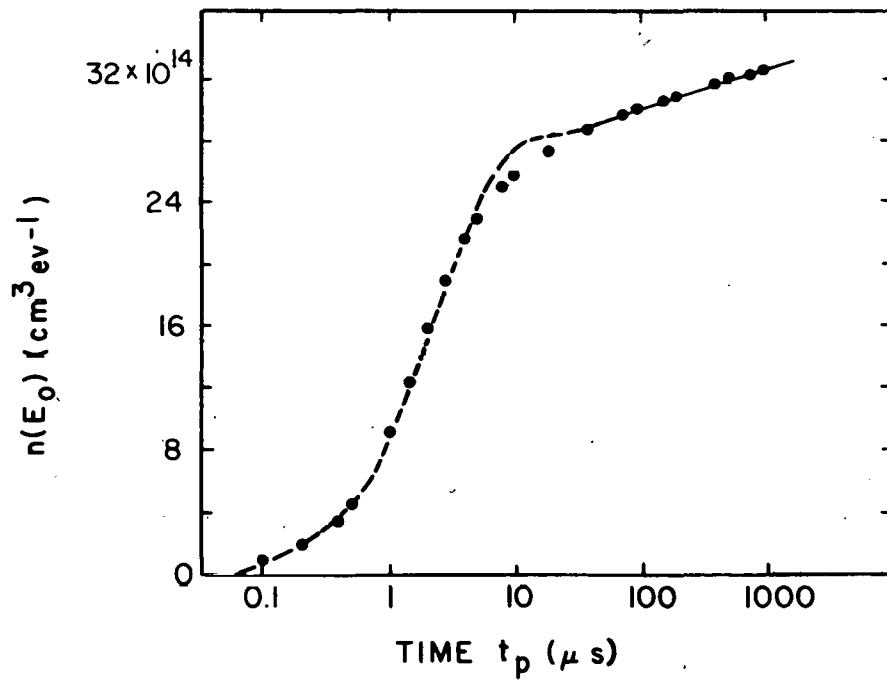


Figure 4. Trapped charge $n(\varepsilon_o)$ vs injecting pulse length $t_p$. The voltage $\Delta V$ is chosen so that $\Delta \ell = \ell$. $V_A = 1$ V. $\ell = 0.2$ $\mu$. The time $t = 40$ $\mu$s. The dashed curve is Eq. (12). Same sample as Fig. 2.

9

that $\Delta \ell = \ell$; i.e., the depletion region is just collapsed. The $n(\varepsilon_0)$ were determined from the current at 80 $\mu s$ after the end of the injecting pulse. The dashed curve is Eq. (12) which fits the data well for short $t_p$, but poorly at long $t_p$. In fact, the data are best explained at long times by a logarithmic dependence on $t_p$. This logarithmic dependence of $n(\varepsilon_0)$ on $t_p$ is not an isolated case. The majority of the a-Si:H (doped and undoped) that has been studied exhibits this behavior. Namely, a linear increase of of $n(\varepsilon_0)$ with $t_p$ followed by a $\ell n(t_p)$ dependence. In no case was an unambiguous saturation in $n(\varepsilon_0)$ with $t_p$ observed which would be characteristic of filling of the level $\varepsilon_0$. Thus, the measurements yield only a lower limit to the density of states.

Additional data for an undoped a-Si:H film with a platinum Schottky barrier are presented in Fig. 5. For this sample the logarithmic dependence of $n(\varepsilon_0)$ on $t_p$ dependence extends over a wider time interval.
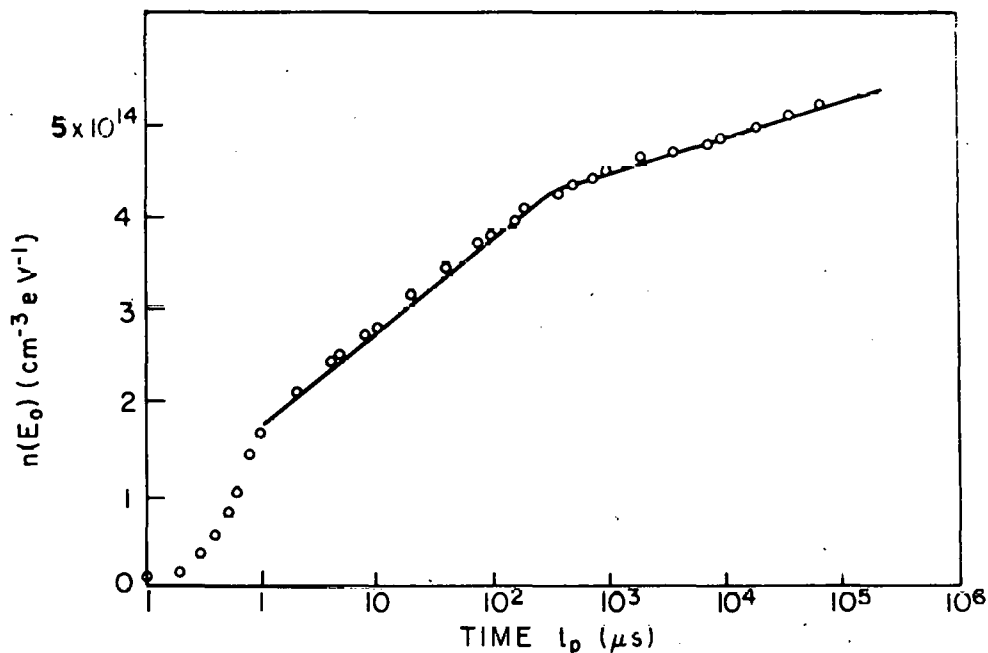


Figure 5. Same type of data as Fig. 4, but for an undoped film.

There is a simple model to explain the failure to observe saturation of the density of trapped electrons with increasing $t_p$. A mechanism that explains the logarithmic time dependence of $n(\varepsilon)$ is that the films are inhomogeneous with electron trapping occurring preferentially in specific regions of

10

the sample. These regions then become negatively charged, thus making further trapping less probable.

We imagine the a-Si:H to be composed of a random distribution of regions containing the majority of the electron traps. These regions are imbedded in the bulk a-Si:H. There is recent evidence that a-Si:H is inhomogeneous. Cylinders perpendicular to the plane of the film have been observed [19]. However, a layered structure in the plane of the film cannot explain all the experimental results. This structure would require that the current during the injecting pulse would decay as $1/t_p$ [20]. However, once the voltage $\Delta V$ is high enough to collapse the depletion width, a further increase in voltage results in injection currents that decrease very slowly with time.

To calculate the actual conduction electron density throughout this inhomogeneous structure is beyond the scope of this report. Therefore, it is assumed that what matters for the capture process is the change in electron density between the surface of the trapping region and the bulk a-Si:H. Then, the electron density at the surface of the trapping region can be expressed in terms of the charging energy $\Delta U$ as

$$n_c = n_o \exp(-\Delta U/kT) \tag{15}$$

where $n_o$ is the electron density in the bulk. The charging energy is the energy required to bring an electron from the bulk and place it on the surface of the trapping region. For most situations, $\Delta U$ will be proportional to the density of charge already trapped. As a simple example, we assume the trapping regions are spheres of radius R and that screening can be ignored. Then, if these regions are uniformly filled with electron space charge of density $N_s$ per unit volume, the charging energy is

$$\Delta U = e^2 R^2 N_s/3\varepsilon_s = a N_s \tag{16}$$

With this model for $n_c$ we can rewrite Eq. (11) as

$$\frac{dn(\varepsilon)}{dt_p} = n_o \beta(\varepsilon) \exp(-a N_s/kT) \tag{17}$$

19. J. C. Knights, G. Lucovsky and R. J. Nemanich, J. Non-Cryst. Solids 32, 393 (1979).
20. H. J. Wintle, IEEE. Trans. Elect. Insul. EI-12, 424 (1977).

with the condition that $f(\varepsilon) \ll 1$. Along with Eq. (17) there is the subsidiary condition that

$$N_s = \Sigma\ f(\varepsilon) = \int f(\varepsilon)\ N(\varepsilon)\ d\varepsilon = \int n(\varepsilon)\ d\varepsilon \qquad (18)$$

Thus, Eq. (17) is just one of a set of equations coupled through $N_s$. Nevertheless, one can take advantage of this coupling to simulaneously solve the entire set. By integrating both sides of Eq. (17) over energy and using Eq. (18) for $N_s$ one arrives at an equation for $N_s$. Namely,

$$\frac{dN_s}{dt_p} = n_o\ \exp\ (-aN_s/kT)\ \int \beta(\varepsilon)N(\varepsilon)\ d\varepsilon = n_o\ W\ \exp\ (-aN_s/kT) \qquad (19)$$

This equation, with the initial condition that $N_s = 0$ at $t_p = 0$, has the solution

$$N_s = \frac{1}{a}\ \ell n\ (1 + t_p/t_o) \qquad (20)$$

where

$$\frac{1}{t_o} = a\ n_o\ W \qquad (21)$$

Substituting Eq. (20) for $N_S$ into Eq. (17) yields

$$\frac{dn(\varepsilon)}{dt_p} = \frac{n_o\beta(\varepsilon)N(\varepsilon)}{1 + t_p/t_o} = \frac{n_o\ W(\varepsilon)}{1 + t_p/t_o} \qquad (22)$$

which, with the initial condition $n(\varepsilon) = 0$ at $t_p = 0$, has the same form of solution as Eq. (19). Namely,

$$n(\varepsilon) = n_o\ W(\varepsilon)\ t_o\ \ell n\ (1 + t_p/t_o) \qquad (23)$$

This equation has the logarithmic dependence on $t_p$ shown in Figs. 4 and 5.

In Fig. 6, $n(\varepsilon_o)$ is plotted vs t the time after the injecting pulse is turned off. These data are for values of $t_p$ corresponding to the beginning of the logarithmic dependence of $n(\varepsilon_o)$ on $t_p$. As might be expected, for a given time t, the doped sample has the larger density of trapped charge. This could be due to either a large density of states, a larger electron capture probability, or a combination of both. At long times (states farther away from the conduction band), both samples exhibit little variation of $n(\varepsilon_o)$ with time (energy). At short times, however, there is a rapid increase in $n(\varepsilon_o)$ with decreasing t for the doped sample. This same behavior has been
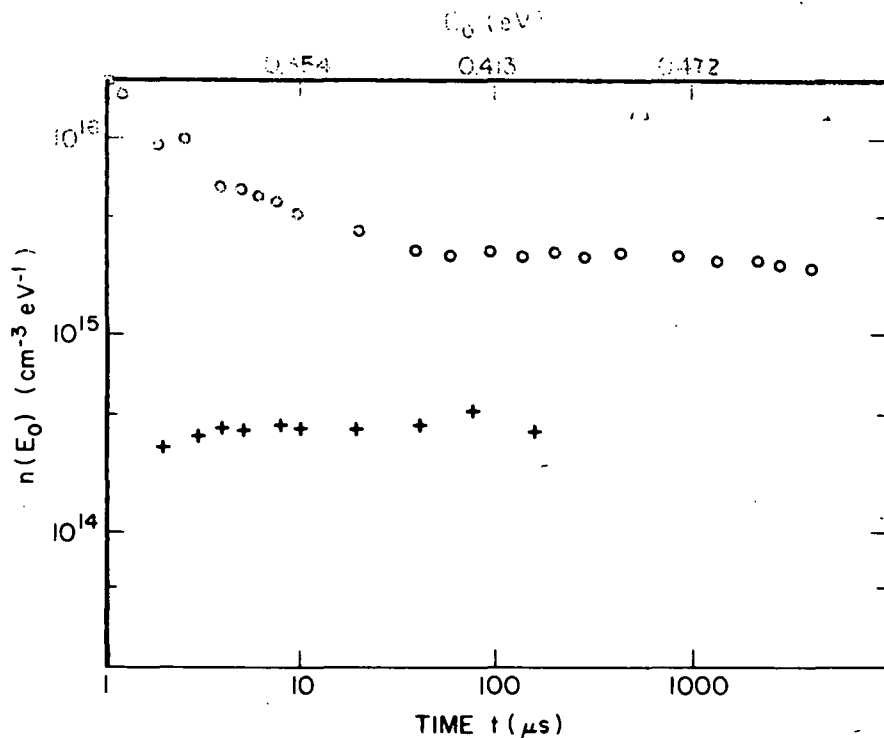
Figure 6. Measured values of trapped charge $n(\varepsilon_o)$ vs time after injecting pulse is terminated. o-doped sample, + undoped sample. The energy scale was determined by assuming $\upsilon = 10^{11}$ s$^{-1}$.

observed by field effect [15] and other means [21] on doped samples. As noted above, $n(\varepsilon_o)$ is less than the density of states $N(\varepsilon_o)$.

To extract more from the data than that it represents the lower limit to the density of states is not warranted. This is because of the problem of the inhomogeneous capture, which introduces too much uncertainty into the interpretation of the data. Even though Eq. (23) shows the logarithmic time dependence of $n(\varepsilon)$, not enough is known about the trapping regions such as their size and distribution to apply the equation in a realistic way to the data.

## B. FIELD-DEPENDENT QUANTUM EFFICIENCY IN a-Si:H

Recent collection efficiency measurements on a-Si:H solar cells were interpreted as giving evidence of geminate-recombination of the exited

21. G. H. Döhler and M. Hirose, Proc. 7th Int. Conf. Amorphous and Liquid Semiconductors, edited by W. E. Spear (CICL, University of Edinburgh, Scotland, 1977), p. 372.

electron-hole pairs [22]. This idea has received further support from measurements of the quantum efficiency for electron-hole-pair ionization using electrophotographic techniques [23]. Because geminate-recombination can be a serious limit to achieving the ultimate efficiency [11] of a-Si:H solar cells, this report will explore the matter further by presenting a model calculation to explain the collection efficiency results [22].

The original proposal [23] of geminate-recombination of electron-hole pairs (exitons) was based on the variation of the solar-cell collection efficiency ($\eta_c$) with depletion width (W) in a Schottky-barrier a-Si:H solar cell. The pertinent data is reproduced in Fig. 7. This data is for illumination with uniformly absorbed light. The important point is that the data can be represented by a linear variation of $\eta_c$ with W. Namely,

$$\eta_c = B \ (W-W_o) \qquad\qquad (24)$$

where B and $W_o$ are constants.
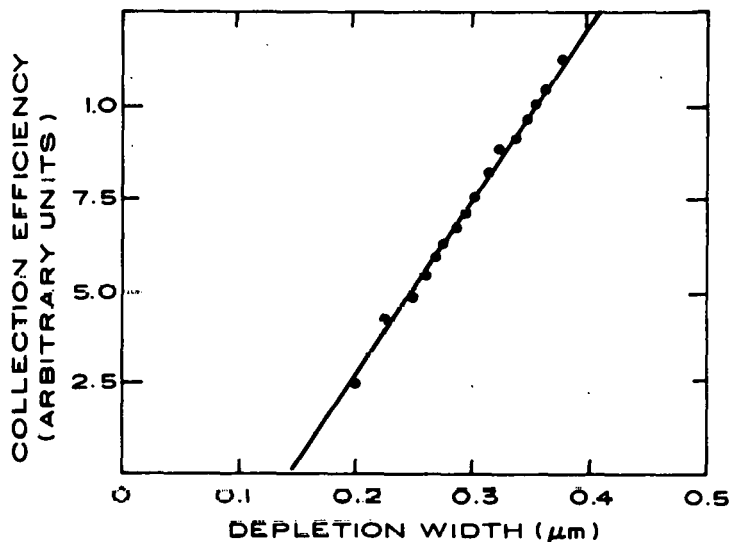


Figure 7. Photocurrent quantum yield, $\eta_c$, as a function of the barrier thickness, W, for a Pt - a-Si:H solar cell.

22. R. S. Crandall, R. Williams and B. E. Tompkins, J. Appl. Phys. 50, 5506 (1979).
23. I. Shimizu, T. Komatsu, K. Saito, and E. Inoue, 8th International Conference on Amorphous and Liquid Semiconductors, Cambridge MA. Aug. 27-31 (1979).

It is easy to show that $\eta_c$ will have this simple dependence on $W$ using a a model of field-dependent exiton dissociation. The collection efficiency is defined by

$$\eta_c = \alpha \int_0^{\ell} P_D(x) \exp(-\alpha x)\, dx \qquad (25)$$

where $\ell$ is the sample thickness and $P_D(x)$ is the probability that a photon produced at a point $x$ in the film produces an electron and hole that are eventually collected at the contacts of the film. Furthermore, it is assumed that each dissociated exiton leads to a collected electron and hole. In other words, recombination is neglected. This assumption is well justified except for pathological situations. Measurements of the minority-carrier diffusion length in a-Si:H indicate it to be short, less than 400 Å [24]. Thus, minority-carrier diffusion from the field-free region into the depletion region can be neglected in this treatment. Even with longer diffusion lengths, the contribution from the field-free region will be small [25].

A general form of the dissociation probability is

$$P_D(x) = P_i(E,T)/[P_R + P_i(E,T)] \qquad (26)$$

where $P_i(E,T)$ is the probability per unit time that the exiton is ionized, and $P_R$ is the corresponding probability for exiton destruction by either radiative or nonradiative recombination of the electron-hole pair. $P_i(E,T)$ will depend on both the electric field $(E)$ and temperature $(T)$. An electric field-dependent quantum efficiency in amorphous selenium [26] has been thoroughly studied and the general features explained in terms of the Frenkel-Poole [27] model of field-assisted thermal ionization of an electron bound to a coulomb potential which is a reasonable approximation to exiton binding. Furthermore, the

24. D. Staebler, ibid.
25. D. E. Carlson, I. Balberg, R. S. Crandall, J. J. Hanak, J. I. Pankove, D. L. Staebler and H. A. Weakliem, Quarterly Report No. 2, prepared for DOE under Contract No. ET-78-C-03-2219, April 1979.
26. D. M. Pai and S. W. Ing, Phys. Rev. 173, 899 (1968); M. D. Tabak and P J. Warter, Phys. Rev. 173, 729 (1968).
27. E. A. Davis, J. Non-Cryst. Solids 4, 107 (1970).

Frenkel-Poole model has been used to explain the field dependence of the dark conductivity in a-Si [28]. Using this model, then $P_i(E,T)$ has the form

$$P_i(E,T) = \upsilon \exp(-\varepsilon_i/kT) \exp(\sqrt{E/E_f}) \tag{27}$$

where $\upsilon$ is the attempt frequency, $\varepsilon_i$ the exiton binding energy. The field $E_f$ is defined by [27]

$$E_f = (kT)^2 \Pi e^3 k_o \tag{28}$$

Here $k_o$ is the high-frequency dielectric constant. For a-Si:H, $E_f \overset{\sim}{\sim} 1.2 \times 10^4$ V/cm at room temperature.

Combining Eqs. (2) - (4) gives for the collection efficiency

$$\eta_c = \alpha \int_o^W \frac{\exp(-\alpha x)\, dx}{1 + b\, \exp(-\sqrt{E/E_f})} \tag{29}$$

where b is the ratio of the recombination probability to the zero field ionization probability, i.e.,

$$b = P_R/[\upsilon \exp(-\varepsilon_i/kT)] \tag{30}$$

If E is independent of x then the integration of Eq. (29) is trivial. However, this is not the usual situation or the one considered in ref. 22. Usually the field decreases linearly from its maximum value at the Schottky-barrier contact to zero at the end of the depletion width. This is the ideal Schottky-barrier situation [18]. It is a good approximation to the situation in a-Si:H under illumination [29]. In this case, however, the integral in Eq. (29) must be evaluated numerically.

Since the data in Fig. 7 are for weakly absorbed light ($\alpha x \ll 1$), the integral in Eq. (29) can be express in an asymptotic form that is of the same form as Eq. (1). After some manipulation, Eq. (29) becomes

$$\eta_c = \alpha (W - W_o) \tag{31}$$

28.  T. Suzuki, M. Hirose, S. Ogase, and Y. Osaka, Phys. Status Solidi 42, 337 (1977); C. R. Wronski, unpublished data.
29.  R. Williams and R. S. Crandall, to be published.

where the term $W_o$ is defined by

$$W_o = \frac{2\,E_f\,\varepsilon_s}{N_s\,e} \int_{z_o}^{b} \frac{\ln(1+z)\,dz}{z} - \ln(z_o)\,\ln(1+z_o) \tag{32}$$

and

$$z_o = b\,\exp(-\sqrt{E_m/E_f}) \tag{33}$$

In the above, the electric field was expressed by the usual equation for a Schottky barrier [18];

$$E = E_m\,(1 - x/W); \quad E_m = W\,e\,N_s/\varepsilon_s \tag{34}$$

Here, $N_s$ is the space-charge density and $\varepsilon_s$ the static dielectric constant. To make the correspondence with the data in Fig. 7, $W_o$ must be shown to be independent of $W$. For this, it is sufficient to show that the terms containing $z_o$ in Eq. (32) can be neglected. Since the collection efficiency is not too small in a-Si:H, $z_o < 1$. For this approximation $W_o$ becomes

$$W_o = \frac{\pi^2\,E_f\,\varepsilon_s}{6\,e\,N_s} \left[ 1 + \frac{12}{\pi^2} \int_{1}^{b} \frac{\ln(1+z)\,dz}{z} + \sigma(z_o) \right] \tag{35}$$

which is to a good approximation independent of $W$. Thus, Eq. (31) is a good representation of the data in Fig. 7. Furthermore, the quantity $W_o\,N_s$ depends only on fundamental parameters of $\alpha$-Si:H.

Since the space-charge density $N_s$ can be changed in a-Si:H by varying the illumination intensity, the constancy of $W_o N_s$ and, hence, the validity of Eq. (35) can be verified. This is shown by the data in Table 1. To obtain this data the illumination intensity was varied to change the space charge density on the sample in Fig. 7. For a given sample the short-circuit current ($J_{sc}$) varies linearly with light intensity. Within experimental error, $N_s W_o$ remains constant. Also in the table are data for a sample that had received intense illumination to change its properties [30]. The main effect is to increase the space charge density. However, $N_s W_o$ is virtually the same as for the other sample. These results give good support to this model calculation.

30.  D. L. Staebler and C. R. Wronski, Appl. Phys. Lett. 31, 292 (1977).

TABLE 1. SHORT-CIRCUIT CURRENT $J_{sc}$, INTERCEPT $W_o$ AND SPACE CHARGE DENSITY $N_s$ FOR DIFFERENT AMOUNTS OF 6328-Å WAVELENGTH ILLUMINATION. THE DATA WITH * IS FOR A SAMPLE DIFFERENT FROM THAT SHOWN IN FIG. 7

| $J_{sc}$ (mA/cm$^2$) | $W_o$ (μm) | $N_s$ (cm$^{-3}$) | $N_s W_o$ (cm$^{-2}$) |
|---|---|---|---|
| 0.52 | 0.14 | $1.3 \times 10^{16}$ | $1.8 \times 10^{11}$ |
| 0.047 | 0.30 | $5.2 \times 10^{15}$ | $1.6 \times 10^{11}$ |
| 0.006 | 0.44 | $3.4 \times 10^{15}$ | $1.5 \times 10^{11}$ |
| * 0.002 | 0.045 | $4 \times 10^{16}$ | $1.8 \times 10^{11}$ |

Substituting the average value of $N_s W_o$ from Table 1 into Eq. (35) permits a determination of b. The result is b = 1.27. This low value of b indicates why a-Si:H solar cells have achieved an efficiency as high as 5.5%. This value of b gives a zero field exiton dissociation probability of 0.44. How much higher the dissociation probability will be in the high-field region of a solar cell can be estimated as follows. The built-in potential is typically about 0.7 eV and if we assume the best situation where the depletion width extends throughout the film thickness of 1 μm, then the collection efficiency per absorbed photon would be about 63%. If the film were 1/2 μm thick, then $\eta_c$ would only increase to 70%. Thus, there is much more to be gained by increasing the film thickness as long as there is a corresponding increase in the depletion width. Furthermore, as is the usual case with geminate-recombination, the higher the exitation energy, the higher the exiton dissociation probability [23]. This is because the electron and hole have a better chance of diffusing apart during thermalization if their respective kinetic energies are higher. Thus, one expects higher collection efficiencies for blue, relative to red light.

## DEPOSITION AND DOPING STUDIES

### A. COORDINATED FABRICATION AND CHARACTERIZATION PROGRAM

Four glow-discharge deposition systems are involved in this program (a large dc proximity system, a small dc/ac proximity system, an rf capacitive system, and an rf magnetron system [25,31]). Films of undoped and doped a-Si:H were deposited on $SiO_2$ substrates in all four discharge systems with temperature gradients running from ~150 to ~350°C. Generally, the photoconductivities of undoped films were $<10^{-5}$ $\Omega^{-1}cm^{-1}$ at all substrate temperatures; however, values as high as $3 \times 10^{-4}$ $\Omega^{-1}cm^{-1}$ were observed for films made in a dc system with an air leak.

One series of films was made (in all four systems) with varying amounts of phosphorus doping. Figure 8 shows the variation in dark conductivity with substrate temperature for varying amounts of $PH_3$ in the discharge atmosphere of a dc system. Figure 9 shows similar data for films made in an rf capacitive system. In general, the most conductive films occur at a doping level of $\gamma = PH_3/SiH_4 \sim 2 \times 10^{-2}$ at the highest substrate temperatures investigated.

Another series of films was made in discharges containing varying amounts of $SiF_4$ in an $SiH_4$ atmosphere (with $\gamma = PH_3/SiH_4 \sim 10^{-2}$). Some data for films made in an rf capacitive discharge are shown in Fig. 10. Small additions of $SiF_4$ $(r = \frac{SiF_4}{SiH_4} + SiF_4 \sim 10^{-2})$ cause a slight decrease in conductivity, while an increase is observed for large concentrations of $SiF_4$ $(r = 0.9)$. Similar trends were observed in the rf magnetron system, but the dependence of conductivity on substrate temperature was stronger.

While these results show that $SiF_4$ additions can improve the conductivity somewhat, the conductivities are still small compared to results obtained with discharges in $SiF_4$ and $H_2$ [32]. This latter work was done at a pressure of

31. D. E. Carlson, R. S. Crandall, B. Goldstein, J. J. Hanak, A. R. Moore, J. I. Pankove, and D. L. Staebler, Final Report, prepared for DOE under Contract No. EY-76-C-03-1286, October 1978.
32. Stanford R. Ovshinsky and Arun Madan, NATURE 276, 482 (1978).
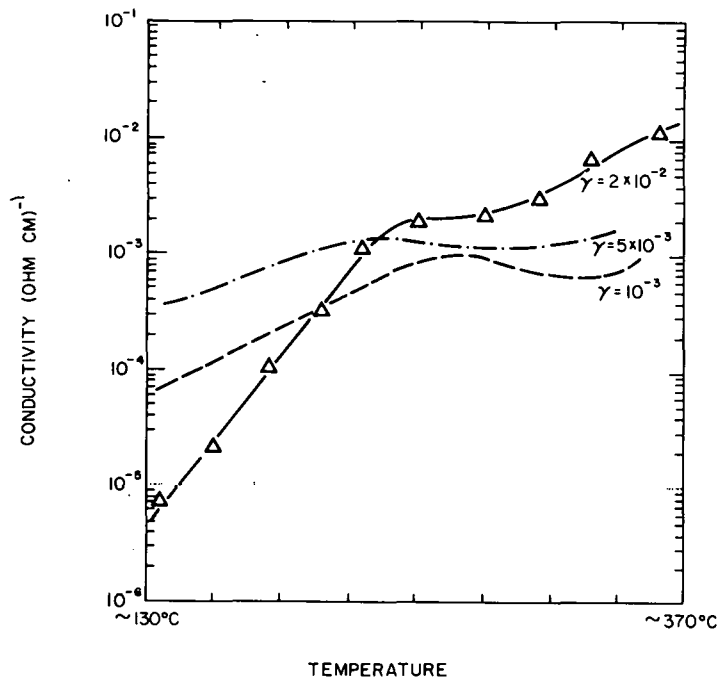
Figure 8. Dark conductivity as a function of substrate temperature for a-Si:H films made with varying amounts of $PH_3$ in a dc glow discharge ($\gamma = PH_3/SiH_4$).
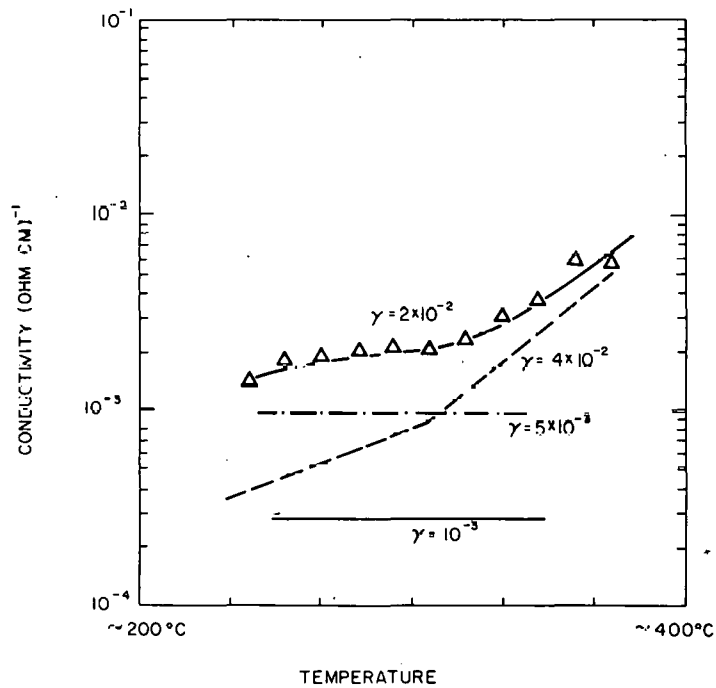


Figure 9. Dark conductivity as a function of substrate temperature for a-Si:H films made with varying amounts of $PH_3$ in án rf glow discharge. ($\gamma = PH_3/SiH_4$).
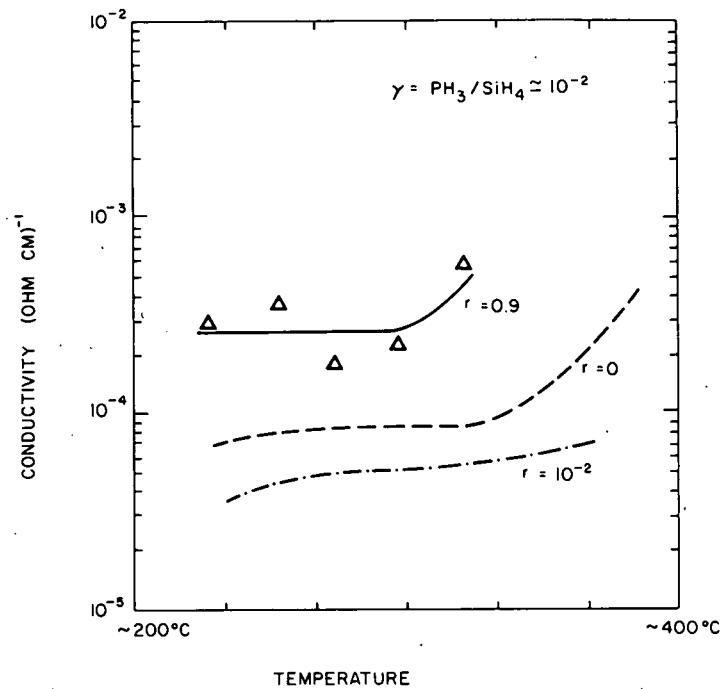
Figure 10. Dark conductivity as a function of substrate temperature for a-Si:H films made with varying amounts of $SiF_4$ in an rf glow discharge. [$r = SiF_4/(SiH_4 + SiF_4)$].

~1 Torr and at relatively high rf power, while our investigations to date have been performed at low pressures (~5-20 mTorr).

We have also made a series of Pt-Schottky-barrier devices in the four discharge systems and find that the large dc system and the rf capacitive system are both making good quality, undoped a-Si:H; collection regions are typically ~0.5 μm thick under AM1 illumination for films made in both systems. Films made in the rf magnetron system exhibit narrower collection regions, apparently due to more $SiH_2$ and $(SiH_2)_n$ groups in these films (as determined from IR absorption). Also, narrow collection regions were observed in films made in a dc system with a small air leak. Thus, while oxygen and nitrogen contaminants can increase the photoconductivity [33], they add to the net space charge in the collection region. The presence of a small amount of phosphorus in the bulk film has a similar effect.

33. R. W. Griffith, F. J. Kampas, P. E. Vanier, and M. D. Hirsch, 8th International Conference on Amorphous and Liquid Semiconductors, Cambridge, MA. (Aug. 27-31, 1979).

## B. INVESTIGATION OF THE dc(P) GLOW DISCHARGE

The dc-proximity method produces a-Si:H layers of relatively high quality; the intrinsic layer in solar cells shows depletion widths ranging from 3000 to 5000 Å, and values of $J_{sc}$ are relatively large (>10 mA/cm$^2$). For this reason considerable time is being given to understanding this method and to determine which parameters may be profitably altered.

The relatively high structural quality of the dc(P) layers is confirmed by IR absorption measurements. Several samples made on a floating substrate showed no detectable absorption at 840 cm$^{-1}$ and 890 cm$^{-1}$. The ratio $\alpha(890\ cm^{-1})/\alpha(2000\ cm^{-1})$ is a measure of the relative amounts $SiH_2 + (SiH_2)_n$ compared to SiH and indicates the degree to which the dangling bonds terminating the $(SiH_2)$ chains remain uncompensated [19]. In our samples this ratio is below 0.05, the lowest value reported in the literature. In comparison, samples made by other methods at RCA Laboratories have shown values for this ratio from 0.18 to 0.60. Some samples made by the dc(P) method with the substrates at positive bias nominally >100 V have shown a barely detectable amount of dihydride. However, because the single-crystal Si substrates were highly resistive, the true surface potential is unknown. This experiment is being repeated with more conducting Si substrates.

While the normal cathode fall in the $SiH_4$ discharge is about 850 V, the floating substrate is normally at about 550 V positive with respect to the cathode. It is probably correct to treat the substrate as a Langmuir probe which touches the plasma that penetrates through the cathode grid. Surprisingly, it was found that as $T_s$ is raised from room temperature to 340°C, the cathode potential for constant current decreases by 300 V, whereas the substrate to cathode potential remains constant. The effect is probably due to local changes in the gas pressure near the cathode.

Applying a bias to the substrate, with respect to the normal floating potential has a strong effect on the deposition rate as shown in the table below:

| Bias (Volts) | Deposition Rate (A/min $T_s$ = 330° |
|---|---|
| 0 | 374 |
| +100 | 80 |
| +130 | 27-62 |
| -254 | 489 |

All samples with positive bias had a grainy appearance, were under 2500-$\overset{\circ}{A}$ thick, and yielded only shorted cells. The samples at negative bias had a normal appearance. It is apparent that these voltages are too large compared to the electron temperature of the plasma; the experiment is being repeated with biases in the range 0 to 50 V.

C. rf MAGNETRON DEPOSITION STUDIES

1. Introduction

A deposition system for rf excitation of a plasma which can be used either with a magnetron electrode or in a planar diode configuration was designed and constructed. The cylindrical vacuum chamber measuring 24 in. long by 19 in. in diameter is constructed entirely of stainless steel and is equipped with several large-access ports and viewing windows. The powered electrode shown in Fig. 11 is rectangular, 7.5 in. x 11.0 in. constructed of a channeled sandwich of monel which allows for water cooling. An array of permanent Alvico V bar magnets contained in a holder (also shown in Fig. 11) may be mounted on the back (air side) of the electrode to provide the magnetron confinement. The magnet array may be readily removed, thus converting the system to an asymmetric capacitor. The rf power source is a 2-kW, 13.56-MHz supply with an automatic tuning matching network*.

Various sample holders have been built and each may be mounted on the circular cover lid of the vacuum chamber. The holders are electrically isolated from the cathode and anode (the entire grounded metal container) of the discharge chamber and may be biased with respect to them. One holder is designed for uniform heating of two 3-in. x 3 in. substrates up to 400°C. Another holder has a heater mounted along one edge and is used to provide a temperature gradient of 100-150°C and a maximum temperature of about 350°C. The heaters are quartz heat lamps embedded in graphite which are fired in dry $H_2$ at 1000°C to removed binders and impurities. Gases are introduced to the discharge chamber via an all-stainless-steel manifold and their flow rates are controlled by electronic mass flow controllers**.

---

*Plasmatherm, Inc. Kresson, NJ.
**Tylan Corp., Torrance, CA.
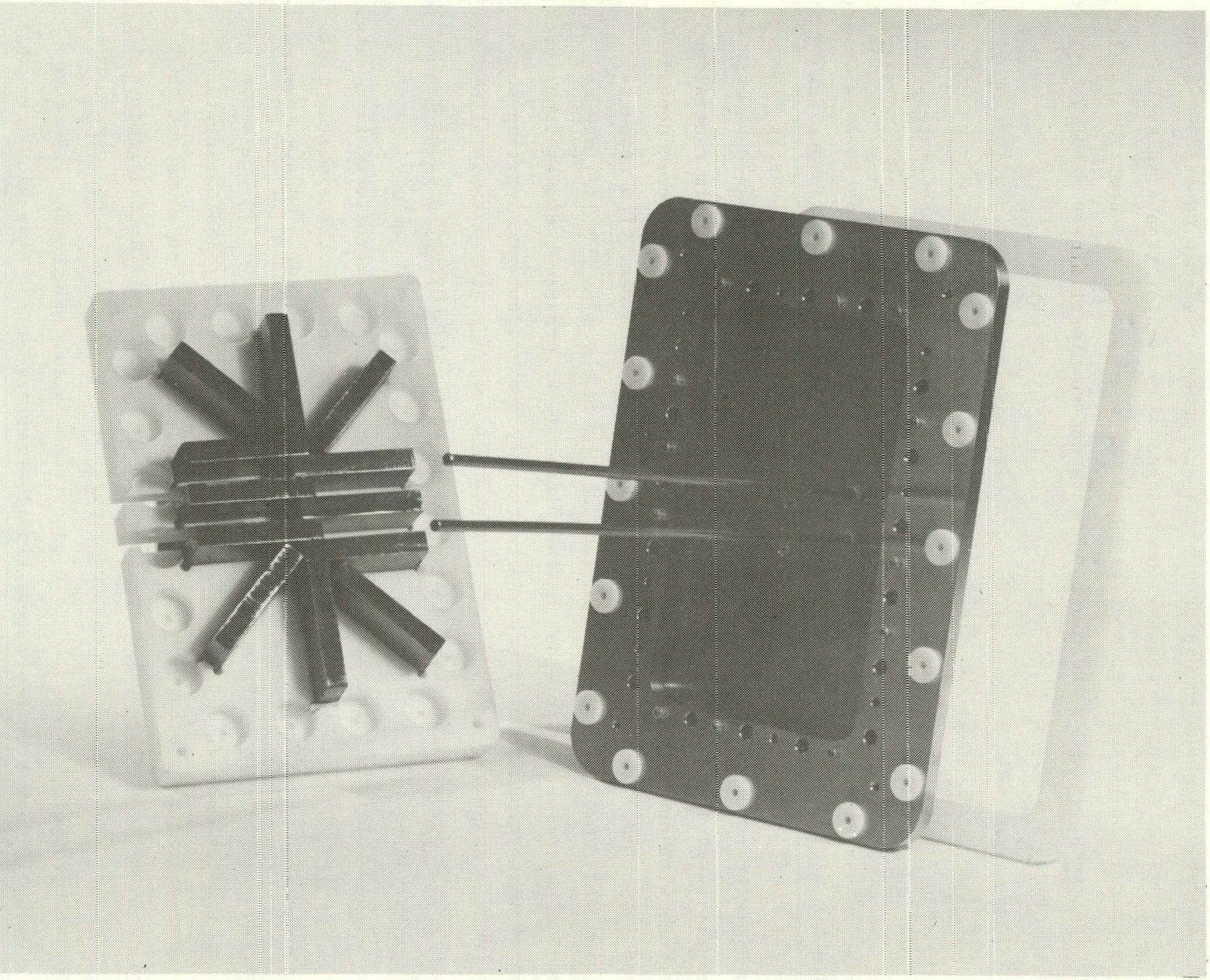
Figure 11. Photograph of rt-powered electrode showing the insulated spacer, water inlet lines, and the magnet array which is inserted into the rectangular opening of the mounting plate.

24

A dual, differentially pumped mass-spectrometer system with line-of-sight viewing of the discharge chamber was designed in collaboration with Extra-nuclear Laboratories (Pittsburg, PA), and was constructed by them. The system has been attached to the discharge chamber and some preliminary results have been obtained, which will be described in the next section.

All of the a-Si:H films produced so far have been prepared using the magnetron mode. The films were deposited on various substrates which were placed parallel to the plane of the cathode. The effects of substrate-to-cathode separation on various properties were studied. At a given separation, there is a spatial variation in the deposition rate, being about 10-20% slower near the center of the cathode than in regions directly opposite from the bright luminous rectangular ring displayed by the magnetron discharge. We have not found conclusive evidence for any differences between physical properties of films deposited opposite the bright ring or the dim central region, with one exception: for pressures greater than 10-15 mTorr, deposits near the center are soft and powderlike, whereas films deposited opposite the bright ring are hard and adherent.

The first samples prepared were contaminated with C, O, and Cr impurities, as determined by SIMS analyses in these laboratories, but this problem was eliminated after finding and sealing some minor vacuum system leaks and coating the chamber walls with Si (this effectively eliminates Cr which comes from the stainless steel).

The deposition rate for pure silane as a function of pressure, flow rate, and rf power was measured. The deposition rate increases approximately linearly with an increase of each parameter, but levels off above the following approximate values; p = 10 mTorr, flow rate = 50 sccm, rf power = 300 W. It was found that good films (judged by the photoluminescence, optical absorption, IR absorption) are produced with p = 9 mTorr, flow rate = 60 sccm, and rf power = 100 W, in which case, the measured deposition rate is 0.1 $\mu$/min.

2. IR and Visible Spectra Analysis

a-Si:H films were deposited on single-crystal Si for several different pressures, flow rates and substrate bias. These films contain no detectable C or O impurities, as determined by the IR absorption in the range 400-4000 $cm^{-1}$. We find that the H content ranges from 7 to 18 at. % using the IR

analysis suggested by E. Freeman and W. Paul [34].  Bands near 800-900 $cm^{-1}$ (usually referred to as dihydride peaks) are seen in all cases.  We find that the ratio of Si-H (the 2000-$cm^{-1}$ band) to Si-H$_2$ + (SiH$_2$)$_n$ (the 2090-$cm^{-1}$ band) increases as the flow rate increases, and also increases when the substrate is electrically connected to the anode (grounded) compared with allowing it to float.  Electrical potential measurements show that the potential of the grounded substrate is less positive than that of the floating substrate by 20-30 V.  Also, the width of the IR bands in a film prepared at a low flow rate (20 sccm) is significantly narrower than at higher flow rates, and for films grown by others using either rf or dc discharges.  Considerable detail is seen, as shown in Fig. 12, and an analysis of the spectra of this and similar samples may provide useful structural information.
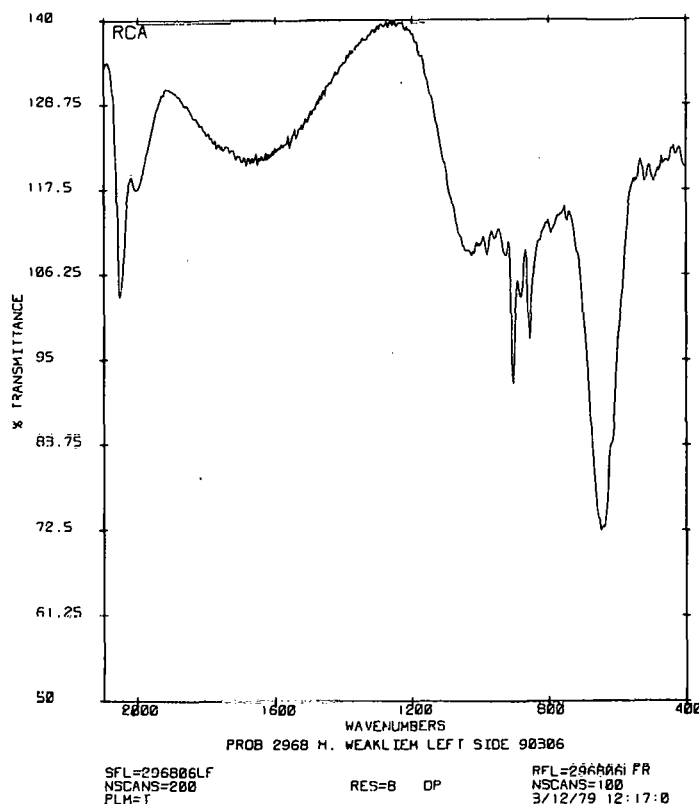


Figure 12.  Infrared absorption of a thick film of a-Si:H deposited on crystalline Si at 50°C.

34.  E. C. Freeman and W. Paul, Phys. Rev. B, 18, 4288 (1978).

The effect of rf power in the discharge on the nature of the infrared modes in the resulting films was studied. We prepared two thick a-Si films deposited on crystalline Si which was held in a temperature gradient of ~50°C over 2 in. (hot and at 300°C), using 2-h deposition time, and 100 W rf in one case, and 50 W rf in the second case. The resulting films were 10.3 μm thick for the former, and 7.5 μm thick for the latter. The IR spectra show no sign of oxygen in either case; however, we see that the dihydride to monohydride ratio depends on both temperature and rf power. Using the ratio $\alpha(840)/\alpha(2000)$ as a measure of the dihydride/monohydride concentration we find:

|  | $\alpha(840)/\alpha(2000)$ | |
|---|---|---|
|  | 300°C | 250°C |
| 100-W sample | 0.194 | 0.150 |
| 50-W sample | 0.172 | 0.127 |

These results, together with recent evidence that solar-cell performance improves as the rf power used during deposition decreases, suggests that dihydride complexes in the a-Si:H film are associated with a trapping state. The question of why lower rf power produces fewer dihydride complexes in the films remains unanswered. However, the presence of dihydride complexes in the a-Si:H films is not simply related to the concentration of clusters of polysilicon-hydrides in the plasma. We find that lower rf power favors the formation of larger clusters of polysilicon hydride ions in the plasma. (See Section III D.)

The optical absorption spectrum for a number of films of various thicknesses deposited on glass substrates held at 300°C and at 350°C were measured. These films were prepared together with films deposited on crystalline Si so that comparison could be made between the optical spectra and the infrared vibrational spectra. A plot of $(\alpha E_p)^{1/2}$ vs $E_p$ for these two temperatures is shown on Fig. 13. ($\alpha$ is the absorption coefficient and $E_p$ is the photon energy.) The energy threshold (commonly referred to as the optical gap), which is obtained by extrapolation of the linear part of the curve to $(\alpha E_p)^{1/2} = 0$, shifts from 1.63 eV for the 350°C film to 1.76 eV for the 300°C film. These results are in reasonable good agreement with earlier
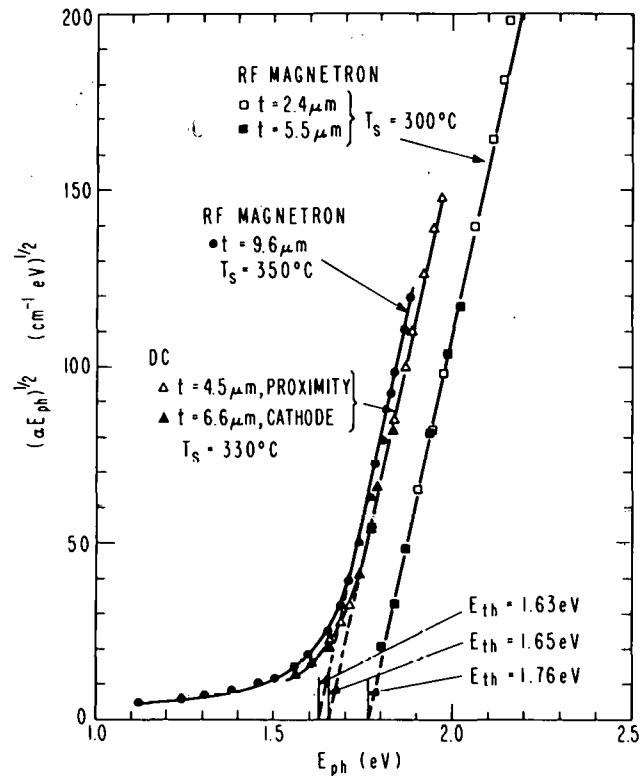
Figure 13. $(\alpha E_p)^{1/2}$ as a function of $E_p$ (photon energy) for a-Si:H deposited on glass at different temperatures.

work in these laboratories [35] and elsewhere [36]; the value for the 300°C film being somewhat high, 1.76 eV vs the earlier value of 1.70 eV. Data for a film prepared in these laboratories recently, using the dc proximity mode and a substrate temperature of 330°C are also shown in Fig. 13. It has the same slope as the rf magnetron results and has an energy threshold value in agreement with the temperature dependence shown by the rf magnetron samples. With respect to this physical property, at least, we may say that films prepared by the rf magnetron are the same as those prepared by the dc proximity techniques.

The temperature dependence of $E_{th}$ has been related to the hydrogen concentration in the films - the greater the hydrogen concentration, the larger the value of $E_{th}$. On the other hand, there is no simple relationship between

35. P. J. Zanzucchi, C. R. Wronski, and D. E. Carlson, J. Appl. Phys. 48, 5227 (1977).

36. G. D. Cody, B. Abeles, C. R. Wronski, and B. Brooks, 8th International Conference on Amorphous and Liquid Semiconductors, Cambridge, MA, (Aug. 27-31, 1979).

$E_{th}$, and, thus, the deposition temperature, and the relative values of the dihydride to monohydride ratio, which we have earlier assumed to be given by the infrared absorbance ratio $\alpha(840\ cm^{-1})/\alpha(2000\ cm^{-1})$. Films prepared by the dc proximity technique have ratios considerably lower than those found so far for the rf magnetron samples. If future experiments continue to support the correlation that the lower the infrared ratio (the fewer the dihydride complexes), the better the solar-cell performance, we shall have to find means to reduce the concentration of the dihydrides in films produced by the rf magnetron, either during or after growth of the film.

## 3. Doping Studies and Schottky-Barrier Cells

The effects of fluorine on a-Si:H properties were studied on a series of films deposited from a plasma having various ratios of the gases $SiH_4$, $PH_3$, and $SiF_4$, and with an rf power of 100 W. The films were grown on substrates having a temperature gradient of 100-150°C across a 4-in.-long sample and the hot end was approximately 300°C. Infrared spectra, dark conductivity, photoconductivity, and tunneling measurements were made.

We find that the dark conductivity increases as the fluorine concentration increases, and at each fluorine concentration it increases with deposition temperature. Since no maximum has been observed, we shall prepare additional films at a higher temperature. The deposition rate strongly depends on the $(SiF_4)/SiH_4)$ concentration ratio, decreasing as the $(SiF_4)$ concentration increases. The deposition rate varies from 0.080 μm/min for 1% $SiF_4$ to 0.020 μm/min for 90% $SiF_4$. The deposition rate does not depend on temperature, however, over the limited temperature range used.

A few Schottky-barrier cells, Pt/undoped a-Si:H/n+ a-Si:H/Mo or stainless steel, were fabricated. The earlier cells generally had low $J_{sc}$ (~2 mA/cm$^2$), fill factors (~0.5), and high-effective series resistance, 70-90 ohm-cm. Recently, however, 1-cm$^2$ cells having $V_{oc}$ ~ 0.45, $J_{sc}$ ~ 4 mA/cm$^2$, FF = 0.55, and efficiencies of ~1% have been prepared.

## D. MASS-SPECTROSCOPIC ANALYSIS OF THE rf MAGNETRON DISCHARGE

### 1. Introduction

Mass spectroscopic analysis of the gas composition of the plasma of a glow discharge is, in principle, capable of providing detailed information about the chemical reactions occurring in the discharge. The technique has been shown to be quite valuable in studies applied to sputtering applications [37-38]. In a glow-discharge system used to deposit a-Si:H, one is interested in analyzing and characterizing the plasma at the place where deposition occurs, and this need causes one of the principal difficulties in doing mass spectroscopy of the discharge. The mass analyzer should be attached to the discharge so that: (1) the plasma conditions are not perturbed by the presence of the analyzer; (2) the geometry should permit collisionless-extraction of the ions and molecules into the analyzer. The analyzer should be capable of detecting ions produced in the discharge, as well as neutrals. Other requirements are a mass range of 1-500, (since clusters may be produced in the discharge), high sensitivity to detect small quantities of short-lived species, and the ability to analyze discharges over a wide pressure range; 1-10 mTorr. It is also quite desirable to energy-analyze the ion beams and to be able to position the entrance aperture at various places in the spatially inhomogeneous discharge. We can do both of these things with the present system; however, with some restrictions and difficulties which will be elaborated on later.

### 2. Instrumentation

A mass-spectrometer system was designed in collaboration with Extranuclear Laboratories, Pittsburgh, PA, and was constructed by them. The necessary vacuum connections between the mass spectrometer and the discharge chamber were designed and built in these laboratories. The system is shown attached to the discharge chamber in Fig. 14.

In order to accommodate a wide range of possible operating pressures in the discharge chamber, a dual-differentially pumped spectrometer system was

37. J. W. Coburn and E. Kay, J. Appl. Phys. $\underline{43}$, 4965 (1972), and references contained therein.
38. A. J. Purdes, B.F.T. Bokler, J. D. Bucci, and T. C. Tisone, J. Vac. Sci. Technol. $\underline{14}$, 98 (1977).
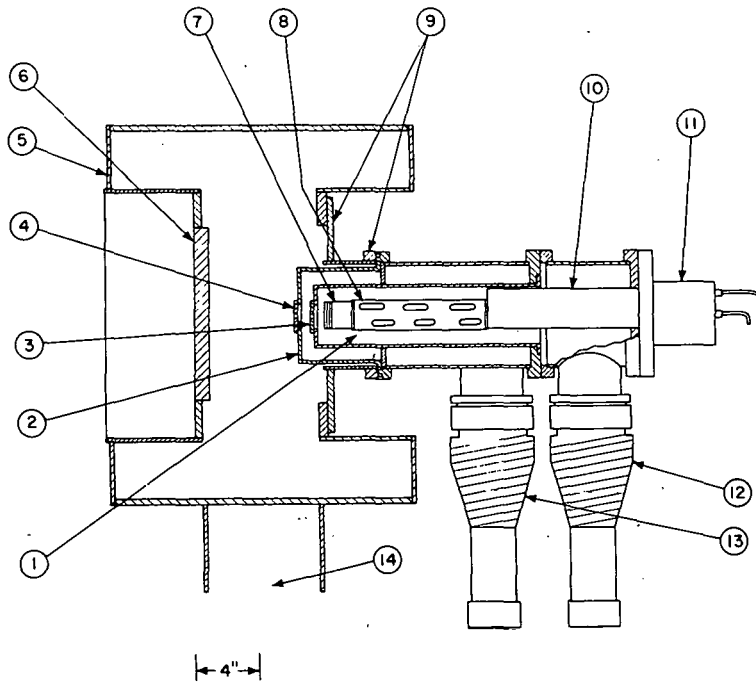
Figure 14.  Schematic cross section of discharge chamber and mass
spectrometer.  The principal items are:
1.  Analyzer chamber
2.  First chamber
3.  Removable aperture disc, analyzer chamber
4.  Removable aperture disc, first chamber
5.  rf Discharge chamber, grounded metal container
6.  rf-Powered cathode
7.  Ionizer and extraction lenses
8.  Quadrupole mass filter
9.  Flanges connecting vacuum chambers
10.  Electron multiplier
11.  High-voltage and signal-lead connections
12.  Vacuum pumps for analyzer chamber
13.  Vacuum pumps for first chamber
14.  To vacuum pumps for discharge chamber

designed.  It is necessary to keep the pressure, $p_A$, in the quadrupole mass
filter - electron multiplier chamber below about $1 \times 10^{-5}$ Torr.  If the dis-
charge chamber is operated at a pressure $p_s$, and the chambers are separated
by a pinhole aperture of area a, the required pumping speed of the analyzer
chamber is given by

$$S = \frac{av}{4} \frac{p_s}{p_A}$$

(36)

where v is the mean velocity of the gas molecules [39]. Using $v = 4 \times 10^4$ cm/s, the value for air at 100°C, and the smallest practical value of 0.01-cm diameter for the pinhole, and taking $p_s = 1$ Torr, $p_A = 1 \times 10^{-5}$ Torr, we find a required pumping speed of 80 $\ell$/s. A small pump could readily achieve this speed; however, considerations of the conductance of the vacuum chamber whose size is dictated by space limitations imposed by the analyzer parts and by the discharge chamber show that the effective pumping speed which could be obtained is only about 10 $\ell$/s.

A dual-differential pumping system allows the pressure reduction to be done in two steps, thus allowing operation of the discharge chamber over a wide range and allowing the use of somewhat larger pinhole diameters than are possible with a single-differential pumping system. The latter feature is desirable since it minimizes the possibility of covering the pinhole aperture with the deposits which occur in the a-Si:H deposition chamber.

The principal features of the system are discussed with reference to Fig. 14. The first chamber serves to reduce the pressure according to Eq. 36 to a value given by the effective pumping speed and the area of the aperture, (4). The pressure is further reduced in the analyzer by the second aperture, (3). The calculated conductance of each chamber is 40 $\ell$/s, and using a pumping speed of 135 $\ell$/s - that of the 63 Series Diffstack, we obtain an effective pumping speed of 30 $\ell$/s. There is a separate pump for each of the two chambers (12) and (13).

The apertures are removable and several sizes ranging from 100 µm to 1000 µm are available. The pressure ratios given by Eq. (36) for various sizes of apertures, and the effective pumping speed of 30 $\ell$/s are shown in Table 2.

TABLE 2.   PRESSURE RATIO FOR SEVERAL VALUES OF APERTURE DIAMETER USING AN EFFECTIVE PUMPING SPEED OF 30 $\ell$/s

| Aperture Diameter (µm) | $p_s/p_A$ |
| --- | --- |
| 200 | 9,500 |
| 300 | 4,200 |
| 1000 | 380 |

39.   S. Dushman, Vacuum Techniques, (J. Wiley & Sons, New York, 1966).

Tests using 300-μm-diam apertures are in good agreement with the value given in Table 2 for both mass-spectrometer chambers.

The distance between apertures (3) and (4) is 2 cm, and between the inner aperture (3) and the entrance port of the electron lens array (7) is also 2 cm. These distances were kept small in order to minimize the loss of short-lived ions or molecules in the beam _via_ molecular collision. The molecular mean free path is given by

$$L = \frac{1}{\sqrt{2}\, \Pi\, \sigma\, n} \tag{37}$$

where $\sigma$ is the collision cross section, and $n$ is the molecular volume density. Although the values of $\sigma$ for silane fragments are not known, useful estimates may be made by taking the value for nitrogen, where $L = 5 \times 10^{-3}/p$ at room temperature, and the units are $L$ in cm and $p$ in Torr. If the first chamber is operated at a pressure below $10^{-4}$ Torr, the conditions for collisionless-extraction are safely met. On the other hand, depending on the pressure in the discharge chamber, one must be very concerned with molecular collision and reactions, which is exactly the problem being addressed.

The quadrupole mass filter (8) is slotted to increase the pumping speed. The quadrupole is model 4-162-8, consisting of 9.55-mm-diam rods 20 cm long. Two high Q Heads are used; one allows coverage at the mass range 1-50 with high resolution (measured $\frac{m}{\Delta m} \geq 1200$) and the other covers the mass range 2-500. A Channeltron electron multiplier (10) is used for ion detection and different signal preamps are available for the detection of either positive or negative ions. The necessary signal and high-voltage vacuum feedthrough connections are contained in the TRIAX head (11).

The mass spectrograph may be used to analyze neutral gases using the electron bombardment ionizer which is part of the ionizer, lens assembly, (7). The ionizer consists of a filament arranged in a square configuration arround the center line of the quadrupole axis. When ions produced in a discharge are to be analyzed, the ionizer is turned off, and since there is no obstruction to a beam defined by the pinhole apertures, the lens aperture and the axis of the quadrupole, ions from the discharge may be transmitted and mass analyzed before being neutralized by collision. For maximum ion-beam signal, it is required that the three apertures and the quadrupole axis be accurately aligned. This was accomplished by using a 633-nm He-Ne

laser beam, a beam splitter, and a long focal-length telescope to align the pinhole apertures before attaching the quadrupole system to the discharge chamber.

## 3. Experimental Results

### a. Neutral Gas Analysis

We have used the spectrometer to analyze the silane gas. In this case, there is no discharge, and the neutral molecules are ionized using the electron bombardment ionizer which is an integral part of the lens array, (7) in Fig. 14.

There are six main mass peaks having the relative intensities shown in Table 3.

TABLE 3. SILANE CRACKING PATTERN

| $m/e$ | $I_{rel}$ | Ion Contributions |
|---|---|---|
| 28 | 33 | $(Si^{28})^+$ |
| 29 | 33 | $Si^{28}H^+$ |
| 30 | 100 | $Si^{28}H_2^+$ |
| 31 | 75 | $Si^{28}H_3^+$ |
| 32 | 7 | $Si^{29}H_3^+ + Si^{30}H_2^+$ |
| 33 | 24 | $Si^{30}H_3^+$ |

These principal mass peaks are in good agreement with previously published values [40]. The peak at mass numbers 32 and 33 can be accounted for almost entirely by contributions from the higher mass isotope of silicon, which occur with the natural abundance $Si^{28} = 92.2\%$, $Si^{29} = 4.7\%$, $Si^{30} = 3.1\%$. We also observe the doubly ionized Si mass peaks, water and carbon at intensities $\sim 0.001$ that of $SiH_4$; however, these latter two could arise from the background in the analyzer chamber, whose base pressure is $5 \pm 2 \times 10^{-7}$ Torr (the pumps are untrapped, oil-diffusion pumps and the chamber walls are not heated to desorb water, CO, $N_2$, the persistent adsorbed gases). We have detected a trace of Cl at 30 ppm, which may be detected at this level because of the absence of interference with normal residual gases of the analyzer.

40. F. E. Saalfeld and H. J. Svec, Inorg. Chem. 2, 46 (1963).

The detection limits of the system with respect to detection in the ppm range for all masses is partly a result of restrictions on the operating pressure imposed by the pinhole apertures and the operating pressure restrictions in the analyzer chamber, as well as the use of untrapped diffusion pumps. Since the system was not designed for neutral gas analysis in the ppm range, however, we are quite pleased that it operates as well as it does for this purpose and believe that we shall improve its performance in the interfering mass range 12-20 with additional operating experience.

b. Analysis of Ions in the $SiH_4$ Discharge

Preliminary results of the ion composition of rf discharges in $SiH_4$, $SiF_4$, and a 50% $SiH_4$:50% $SiF_4$ mixture have been obtained. The magnetron mode was used throughout, and the effects of rf power and discharge pressure were examined.

In order to detect ions produced in the discharge, the ionizer of the mass spectrometer is turned off and the focusing lenses [(7) in Fig. 14] are used to extract the ions from the discharge chamber and focus them onto the axis of the quadrupole mass filter.

In a pure silane discharge, the most intense peak occurs at m = 31, corresponding to $SiH_3^+$. There are two peaks at m/e = 32, and m/e = 33 which are in the proper intensity ratio to that of m/e = 31 to be accounted for by the $Si^{29}$, and $Si^{30}$ isotopes. This triplet is a very useful diagnostic tool for more complex spectra. The relative intensities of the m/e = 28 to m/e = 33 mass peaks are shown in Table 4.

TABLE 4.  RELATIVE INTENSITIES OF THE MASS 28 THROUGH MASS 33
PEAKS FOR SILANE IN A 100-W rf DISCHARGE

| m/e | Relative Intensity | Ion |
|---|---|---|
| 28 | 1.9 | $Si^+$ |
| 29 | 6.3 | $SiH^+$ |
| 30 | 2 | $SiH_2^+$ |
| 31 | 100 | $SiH_3^+$ |
| 32 | 5.5 | $Si^{29}H_3^+ + Si^{28}H_4^+$ |
| 33 | 4 | $Si^{30}H_3^+$ |

There is no strong dependence of these relative intensities on either rf power (over the range 75 W to 300 W) or pressure (over the range 7 - 15 mTorr). It appears that the relative intensity of m/e = 29 increases slightly as rf power decreases.

We also observe higher clusters of $Si_xH_y^+$ ions. The spectrum consists of clusters, beginning with the unhydrated $Si_x^+$ ion for x up to 6, followed by 8 - 16 peaks corresponding to the sequence $Si_x^+$, $Si_xH^+$, $Si_xH_2^+$, etc. The approximate relative intensity of the clusters is indicated in Table 5 which lists the intensity of the strongest m/e peak in each group up to trimers for $p \sim 7.5$ mTorr, and two different rf power levels.

TABLE 5. INTENSITY OF THE STRONGEST m/e PEAK WITHIN EACH GROUP FOR IONS CONTAINING 1,2, AND 3 Si ATOMS, p = 7.5 Torr AND rf POWER OF 100 W AND 190 W

| m/e | ion | 100 W rf $I_{rel}$ | 190 W rf $I_{rel}$ |
|---|---|---|---|
| 31 | $SiH_3^+$ | 100 | 100 |
| 60 | $Si_2H_4^+$ | 13.8 | 8.3 |
| 61 | $Si_2H_5^+$ | 14 | 8.5 |
| 91 | $Si_3H_7^+$ | 1.4 | 0.5 |

Table 5 shows, and additional data are in agreement, that the higher the rf power the greater the relative intensity of the smaller clusters.

c. $SiF_4$ Discharge

The spectrum of ions in a $SiF_4$ is considerably simpler than that of silane, owing in part to the absence of hydrogen. The principal peak occurs at m/e = 47 corresponding to $SiF^+$. The other peaks observed in a 100-W rf discharge at 10 mTorr are shown in Table 6, where we consider only peaks corresponding to the $Si^{28}$ isotope.

d. 50% $SiH_4$ - 50% $SiF_4$ Discharge

The spectrum is quite complicated, but the m/e peaks at 31 and 47 dominate. Thus, the principal ion seen in the corresponding pure $SiH_4$ or $SiF_4$ discharges also dominate the mixture. The dimer spectrum of $Si_2H_y^+$ is also seen.

TABLE 6.   RELATIVE INTENSITIES OF IONS IN A $SiF_4$
100-W rf DISCHARGE AT p = 10 mTorr

| m/e | Ion | $I_{rel}$ |
|-----|-----|-----------|
| 47 | $SiF^+$ | 100 |
| 56 | $Si_2^+$ | 0.03 |
| 66 | $SiF_2^+$ | 0.5 |
| 85 | $SiF_3^+$ | 0.2 |
| 94 | $Si_2F_2^+$ | 0.03 |
| 104 | $SiF_4$ | 0.001 |

## 4.  Discussion and Conclusions

The existence of secondary, tertiary, and higher ions in a silane dis-
charge shows that ion-molecule reactions are very important.  At the pressures
and power levels used - typical for the growth of a-Si:H films - the discharge
corresponds to a weakly ionized plasma.  Most of the gas molecules are neutrals
and their concentration is much greater than that of the ions.  Reactions in-
volving a primary ion produced by the discharge with a neutral molecule may
produce a secondary ion containing two silicon atoms; this ion, in turn, may
react with another neutral molecule to produce a tertiary ion containing
three Si atoms, and so on.

The ion-molecule chemistry of silane has been studied previously by
several groups [41-43].  They find the principal primary ions as $SiH_2^+$ and
$SiH_3^+$.  In fact, $SiH_3^+$ is also produced as a secondary ion by the reaction

$$SiH_2^+ + SiH_4 \rightarrow SiH_3 + SiH_3^+ \tag{38}$$

These studies find the secondary ion $Si_2H_4^+$ is the predominant product of
reactions of $SiH_4$ with $SiH_2^+$ and $SiH_3^+$.  They also find that there is a
strong pressure dependence in the relative intensities of the secondary

41.  T. Y. Yu, T.M.H. Cheng, V. Kempter, and F. W. Lampe, J. Phys. Chem. 76
     3321 (1972) and earlier work cited therein.
42.  J.M.S. Henis, G. W. Stewart, M. K. Tripodi, and P. P. Gaspar, J. Chem.
     Phys. 57, 389 (1972).
43.  G. Nolet, J. Electrochem. Soc. 122, 1030 (1975).

ions; however, the strong pressure dependence occurs for pressures above about 50 mTorr, which is higher than that used in our studies.

We note that we observe the ion $Si_3H_7^+$ in these studies, and, although this ion is the largest percentage of the tertiary ions observed, the tertiary ion only becomes significant above a pressure of 100 mTorr [41]. The apparently high concentration of the higher $Si_xH_y^+$ clusters which we find is rather surprising, considering the low pressure of the discharge.

The studies we report here must be regarded as preliminary ones. Future work will attempt to obtain more details about the reaction kinetics of the discharge. We are planning experiments involving both dc and rf diode and magnetron discharges aimed at identifying the principal reactions involved in a-Si:H film growth. We anticipate the need to energy-analyze the ion beam. Although our present equipment does not include a separate velocity analyzer, we can bias the axis of the quadrupole mass filter with respect to ground, which is the reference potential to which the energy of an ion beam in the analyzer is referenced.

We shall also study the effect of varying the dc potential of a substrate with respect to the plasma potential. We intend to place the substrate immediately in front of the first pinhole aperture of the mass spectrometer and the substrate will have a suitable hole in it to allow the passage of ions through it to the mass spectrometer.

# SECTION IV

## EXPERIMENTAL METHODS FOR CHARACTERIZING a-Si:H

### A.  PHOTOLUMINESCENCE OF FLUORINE-DOPED a-Si:H

A mixture of $SiF_4$ and $H_2$ was fed into an rf-capacitive discharge system. A series of runs was made at a total pressure of about 1 Torr while the ratio of $H_2$ to $SiF_4$ pressure was varied from 0 to 4.3.  The substrate temperature was kept at 350°C.  No deposit is obtained when the $H_2/SiF_4$ pressure ratio is less than 0.1.  When the pressure ratio exceeds 0.3, a dark film is obtained which luminesces over a broad spectral range with a contribution above 1.6 eV.  As the pressure ratio is increased (less $SiF_4$), the higher energy contribution decreases rapidly (Fig. 15).  The dominant peak always occurred at ∿1.15 eV.  The IR vibrational spectrum revealed a strong $SiO_2$ band, but none due to SiF.  Hence, we hypothesize that the plasma forms HF, which attacks the glass walls and release oxygen from the walls.
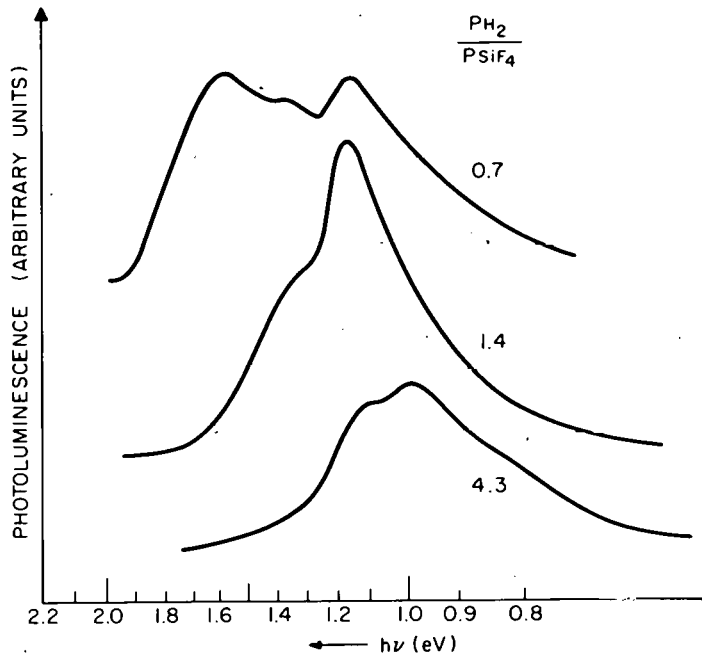


Figure 15.  Photoluminescence intensity as a function of photon energy for various pressure ratios for $H_2$ to $SiF_4$.

Another series of glow-discharge depositions was made from a mixture of $SiF_4$ and $SiH_4$.  When the ratio of $SiF_4/(SiF_4 + SiH_4)$ is varied from 0 to 0.9,

39

the luminescence intensity decreases slowly to a ratio of 0.8, then drops precipitously (see Fig. 16). The emission spectrum does not vary significantly. The film is clearer (perhaps, thinner) for the larger values of the $SiF_4$.
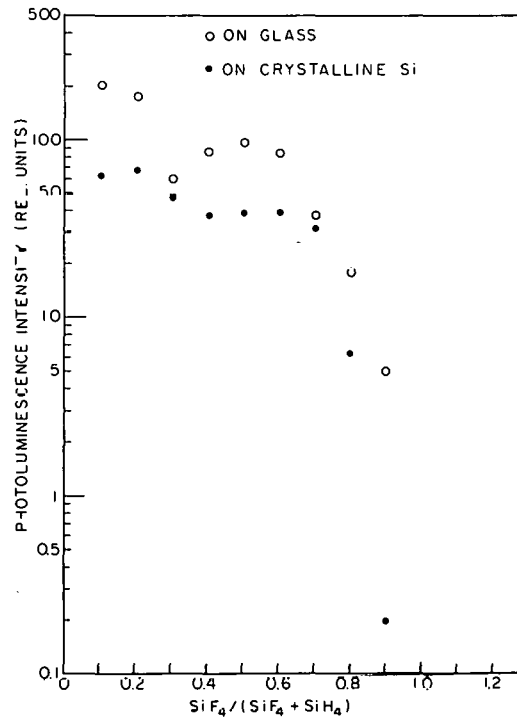


Figure 16. Photoluminescence intensity as a function of the ratio $SiF_4/(SiF_4 + SiH_4)$.

Layers deposited from a mixture of $SiH_4$ and HF tend to be less efficient than the HF-free product. The efficiency of the 1% HF film decreases with decreasing substrate temperature, as shown in Fig. 17, whereas, the efficiency of the 50% HF film decreases with increasing substrate temperature. The films were deposited on substrates in a temperature gradient running from ∿140 to ∿330°C.

Six samples deposited from an ac glow discharge using a mixture of $SiF_4$ and $SiH_4$ (+500 ppm $B_2H_6$) were tested. As shown in Figs. 18 and 19, the base sample with 0% $SiF_4$ was the most efficient, emitting at ∿1.3 eV over the whole substrate temperature range. The 0.1% $SiF_4$ was slightly less efficient and also emitted at 1.3 eV. The 1% $SiF_4$ sample exhibited at $T_s > 250°C$ two peaks (1.1 and 1.3 eV) and a decreasing efficiency. With 10% SiF the luminescence efficiency dropped by about one order of magnitude (compared to base),

40
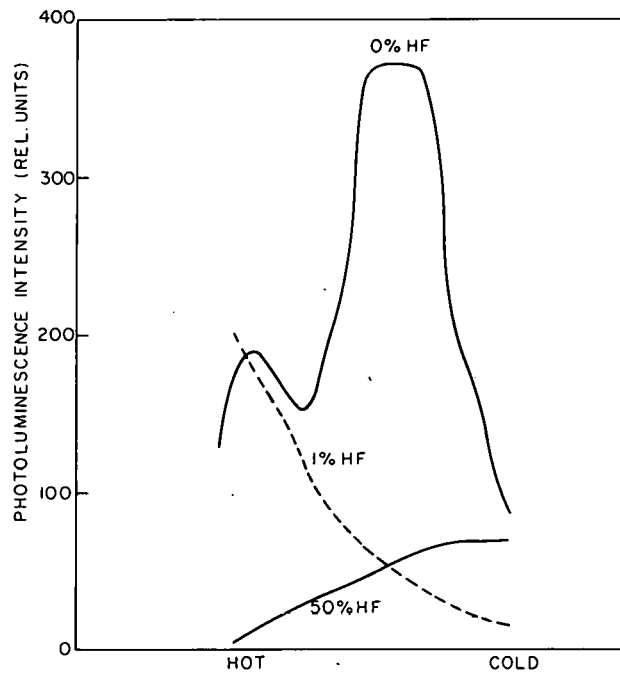
Figure 17.  Photoluminescence intensity as a function of substrate
temperature for various discharge atmospheres.
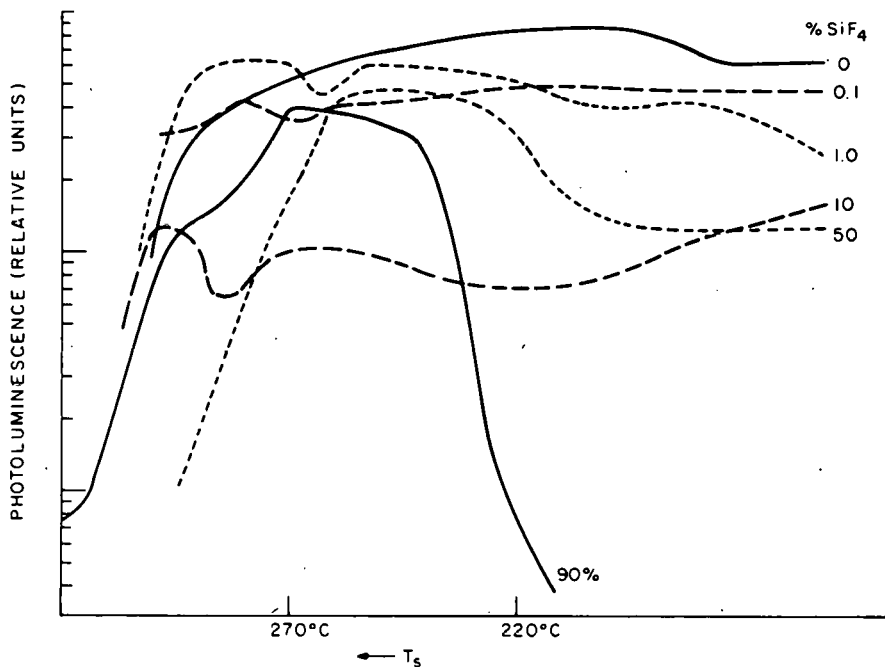


Figure 18.  Photoluminescence intensity as a function of substrate
temperature for various percentages of $SiF_4$ in an ac
discharge containing $SiH_4$ (+500 ppm $B_2H_6$).

% SiF$_4$

50

90

1.5

h$\nu$(eV)

10

0

0.1

1.0

1.0

1.0

0.1

10

HOT

T$_s$

COLD
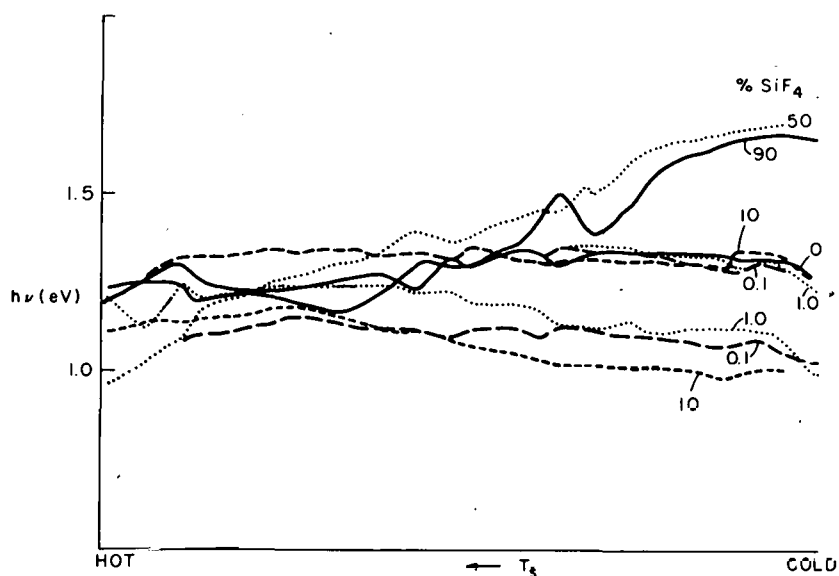
Figure 19. Peak emission energy as a function of substrate temperature for various percentages of SiF$_4$ in an ac discharge containing SiH$_4$ (+500 ppm B$_2$H$_6$).

and above T$_s$ = 240°C exhibited two peaks (1.0 and 1.3 eV). The efficiency of the 50% SiF$_4$ samples maximizes sharply at T$_s$ = 220°C, while the emission peak shifts from 1.7 eV to 1.0 eV as T$_s$ increases from 145 to 315°C. The efficiency of the 90% SiF$_4$ sample maximizes at T$_s$ ∼ 240°C, while the emission peak climbs from 1.2 to 1.7 eV above T$_s$ = 230°C. In all figures the hot end is at ∼330°C, and the cold end at ∼140°C.

Another sample, deposited from 10% SiF$_4$ and 90% SiH$_4$, was n-type at the hot end, and p-type at the cold end. In this sample, the luminescence peak shifted from 1.34 to 1.10 eV from hot to cold substrate temperature and a second peak appeared at 1.4 eV near the cold end (Fig. 20). The luminescence efficiency exhibits a broad maximum with T$_s$ at about 230°C (Fig. 21). Another sample made from 100% SiH$_4$ exhibited the same spectral dependence on T$_s$ (Fig. 22), but a somewhat lower luminescence efficiency (Fig. 23). The emergence of a higher energy luminescence peak in low T$_s$ material is consistent with a widening of the energy gap, as evidenced by the absorption data of Fig. 24 which shows a 0.1-eV increase in the energy gap of the fluorinated sample.
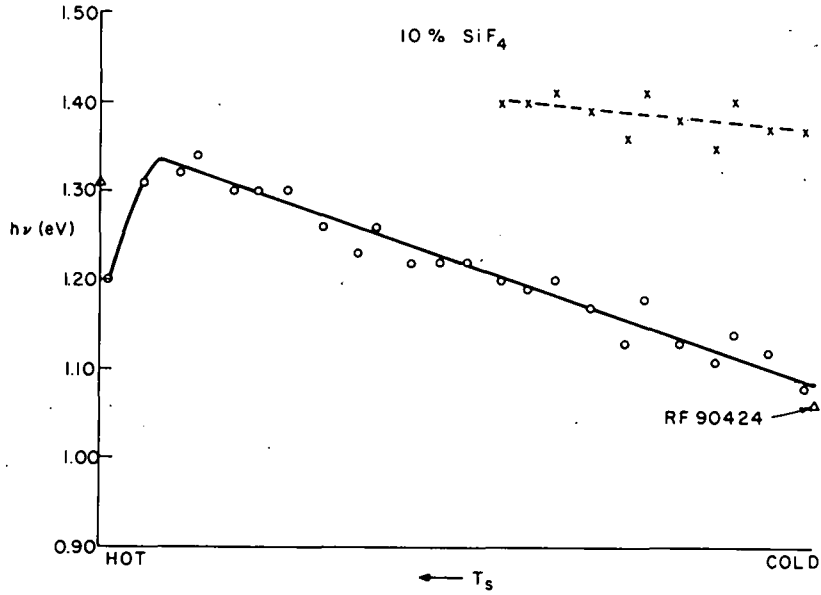
Figure 20.  Peak emission energy as a function of substrate temperature
for an ac discharge containing 10% $SiF_4$ and 90% $SiH_4$.
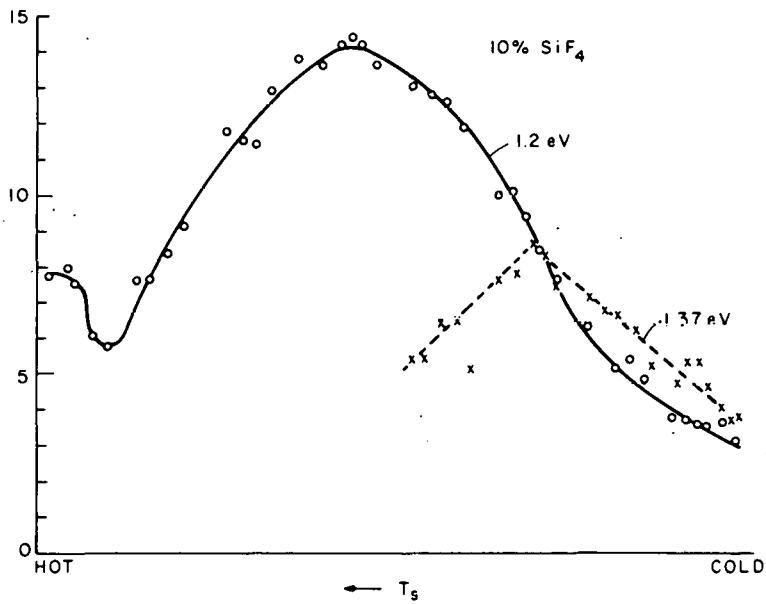


Figure 21.  Photoluminescence intensity as a function of substrate tempera-
ture for an ac discharge containing 10% $SiF_4$ and 90% $SiH_4$.

0 % SiF$_4$
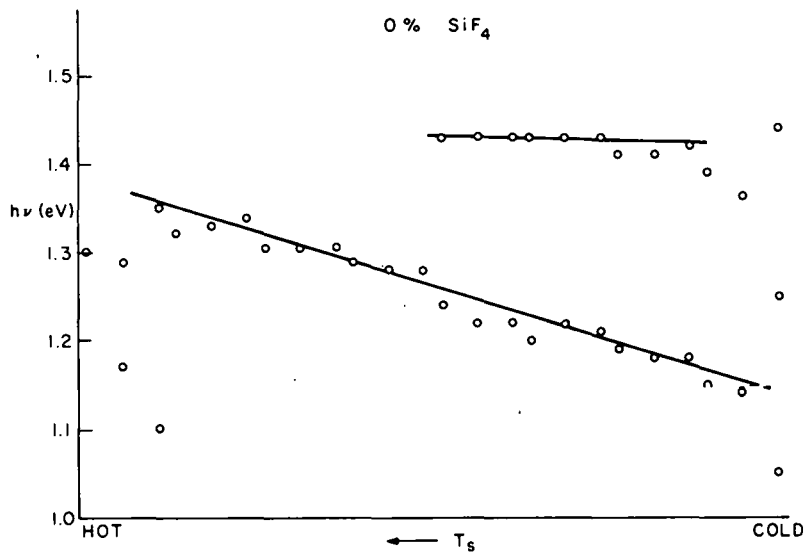
Figure 22.  Peak emission energy as a function of substrate temperature
for an ac discharge in SiH$_4$.



0% SiF$_4$
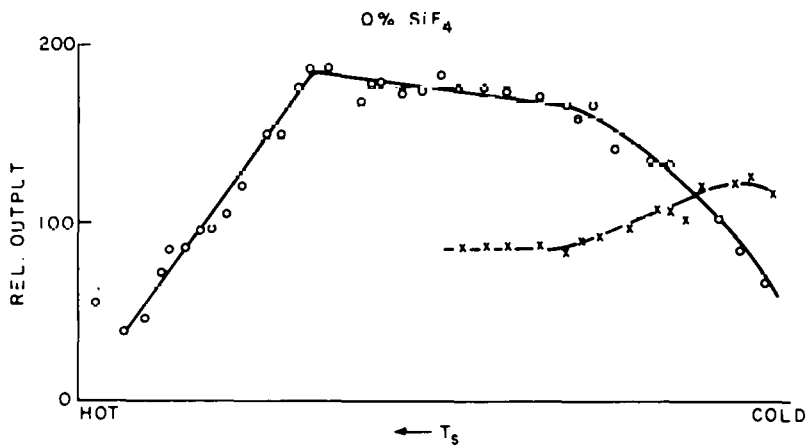
Figure 23.  Photoluminescence intensity as a function of substrate
temperature for an ac discharge in SiH$_4$.
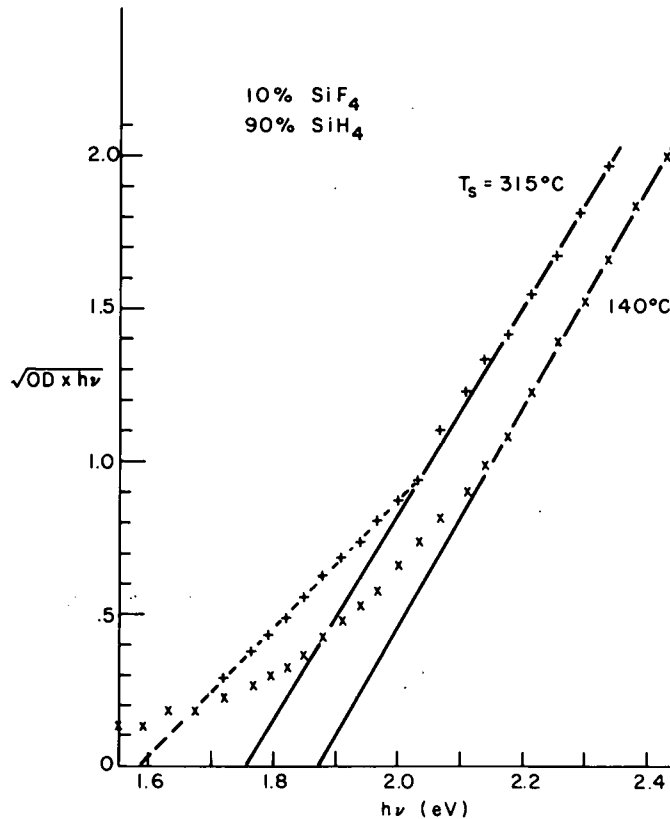
Figure 24.  The square root of the optical density-photo-energy
product as a function of the photon energy for films
deposited at 140°C and 315°C in an ac discharge con-
taining 10% $SiF_4$ and 90% $SiH_4$.

## B.  PHOTOCONDUCTIVITY SPECTRA OF a-Si:H

The room-temperature photoconductivity (PC) spectra of many samples were
expressed as photocurrent per incident photon before plotting.  All the samples
show a response extending far below the bandgap, and still detectable below
0.6 eV.  In most samples, the response increases monotonically with photon
energy and the increase becomes very rapid above about 1.4 eV (see Fig. 25).
The main PC peak occurs at ∿1.9 eV; it is due to the transport of carriers
excited across the energy gap.  In some samples a shoulder is obtained at
∿1.2 eV (see Fig. 26), and in a few samples a peak at ∿1.2 eV is found (see
Fig. 27).  The ∿1.2-eV peak is tentatively attributed to the excitation of
electrons out of deep acceptors to donors.  This is believed to be the inverse
of the luminescent transition.  A similar peak was found in the photovoltaic
spectrum of one sample (see Fig. 28).
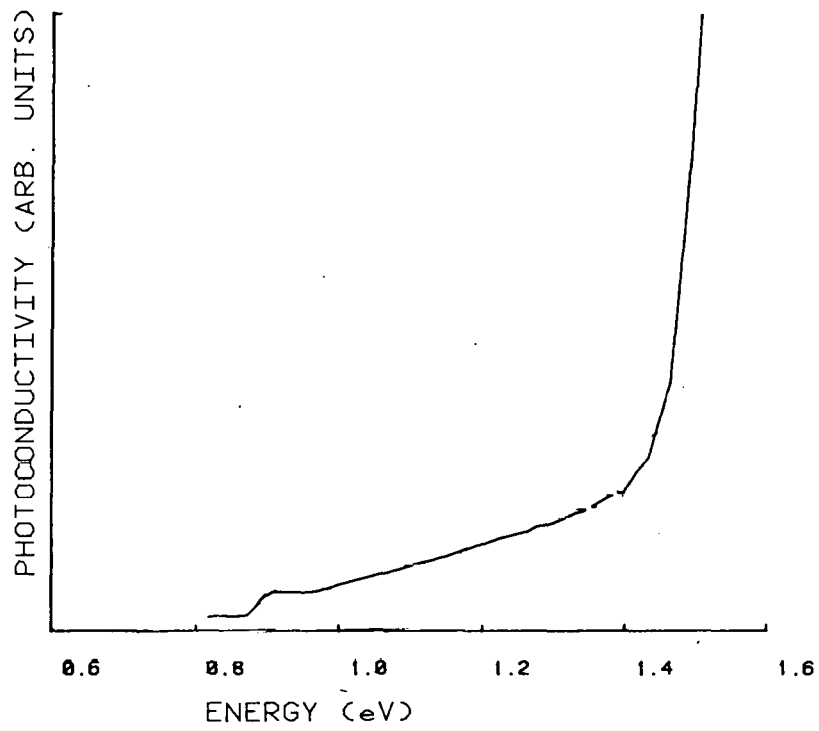
Figure 25.  Photoconductivity spectrum of undoped a-Si:H.
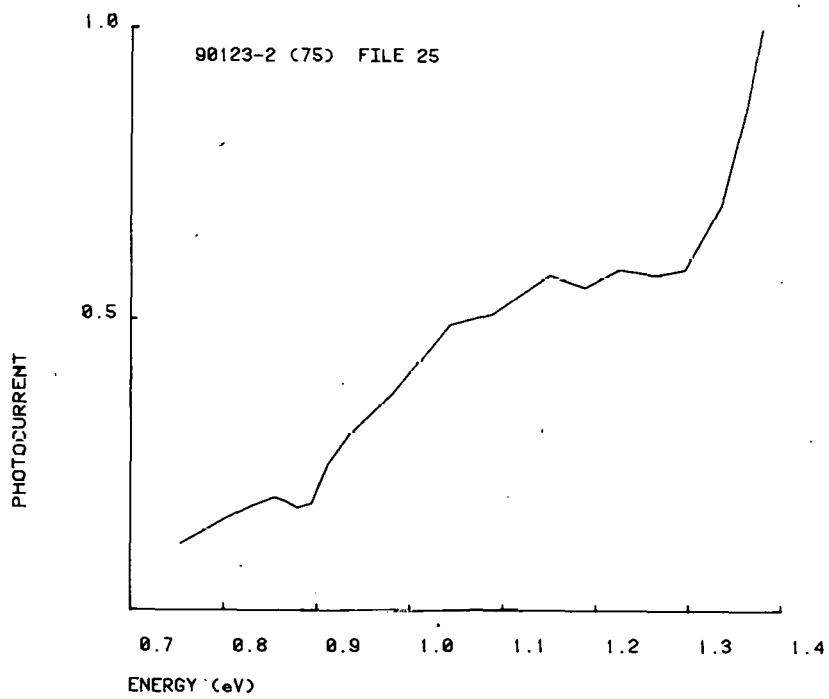


Figure 26.  Photoconductivity spectrum showing a shoulder at ~1.2 eV.
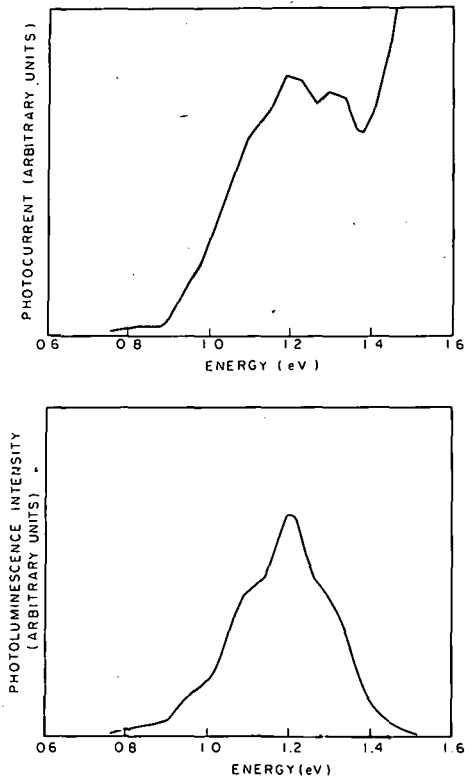
Figure 27.  Photoconductivity spectrum of a film of a-Si:H at room
temperature and its photoluminescence spectrum at 78K.
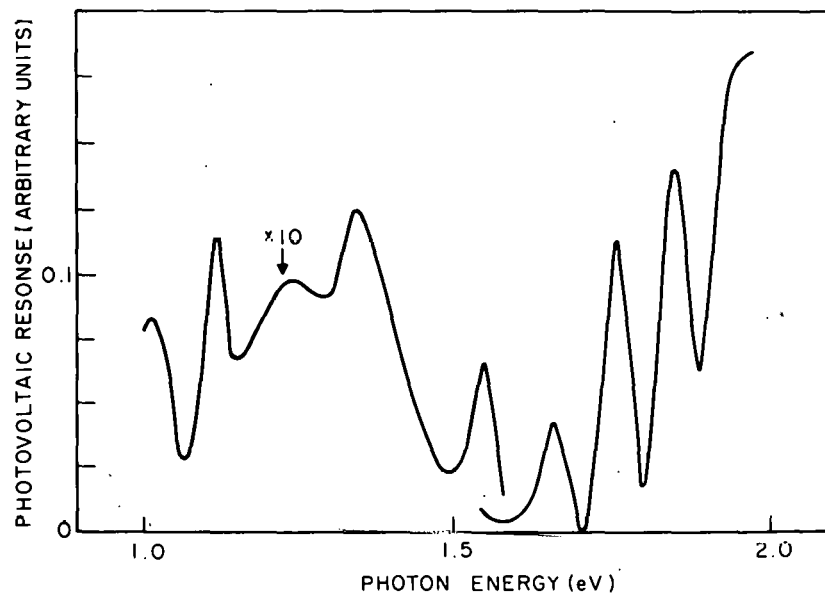


Figure 28.  Photovoltaic response of KCl Schottky barrier to a-Si:H at
room temperature.  The photovoltage is normalized with
respect to incident power.  The oscillations are due to
interference effects in the thin film.

Conduction is due either to hopping transport from donor to donor or to motion in the conduction band after thermal excitation from the donors. The photocurrent at 1.2 eV increases linearly with light intensity. The main argument for assuming an acceptor-to-donor optical transition is the observation of a dropping high-energy edge of the 1.2-eV peak, instead of a plateau. A transition from an acceptor band to a conduction tail would produce a threshold followed by a plateau, then a second threshold at the onset of the across-the-gap transition (see Fig. 29(a)). In contrast, a transition from acceptors to donors would produce one threshold, a peak, and then a drop in response as fewer states can be linked by the higher-energy photons, until across-the-gap transitions could generate a second (steeper) threshold (see Fig. 29(b)).

The most striking correspondence between absorption and emission (suggesting that the same optical transition is seen in both directions) is shown in Fig. 27. Both the luminescence and photoconductivity spectra exhibit identical rippled modulation due to interference effects in the thick layer.

In order to avoid the interferometric oscillations which modulate the PC spectra, the measurements are made at the Brewster angle with polarized light. Although this precaution greatly reduces the amount of light incident on the specimen, the interference is almost completely eliminated.

## C. HYDROGENATED-AMORPHIZED SINGLE-CRYSTAL SILICON

Crystalline Si (c-Si) ion-implanted with Si+ becomes amorphous within the implantation range at a dose greater than $10^{14}$/cm$^2$. After hydrogenation, the photoluminescence forms a broad band at ~1.15 eV. Its temperature dependence shows an activation energy of 0.15 eV for the competing nonradiative recombination, as shown in Fig. 30(a) (compared to 0.13 eV for glow-discharge deposited a-Si:H). In contrast, c-Si implanted at a dose of 1 x $10^{13}$/cm$^2$ after hydrogenation exhibits narrower emission band at 0.98 eV, the temperature dependence of which has an activation energy to 0.09 eV, shown in Fig. 30(b).

The emission at 0.98 eV is due to an implantation-induced defect which does not depend on the chemical nature of the implanted ion. However, hydrogenation is required to make this peak efficient.

The emission peak of the sample amorphized at 7 x $10^{14}$/cm$^2$ shifts to lower energy with increasing temperature at a rate of 1.1 x $10^{-3}$ eV/K, whereas

48
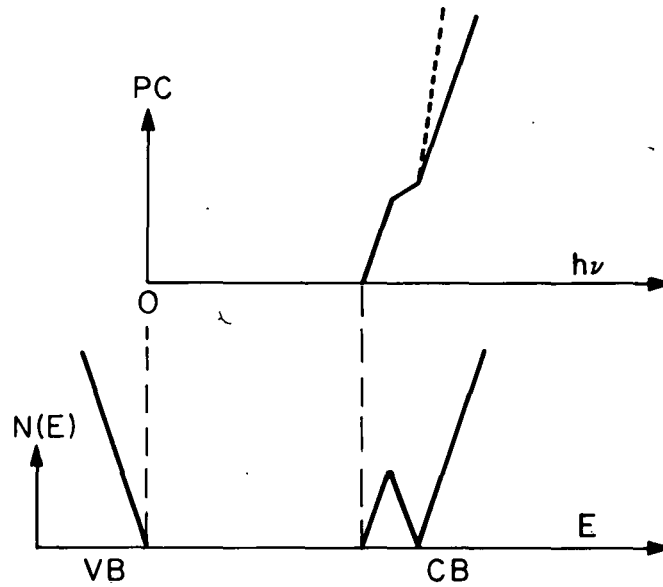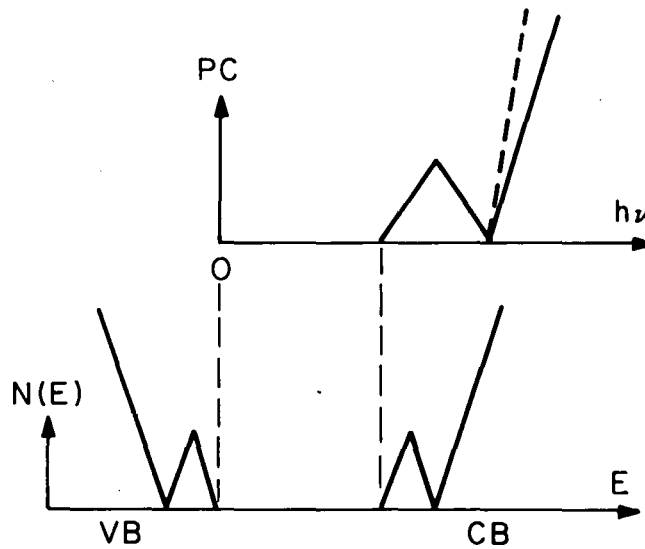
Figure 29. Idealized band structure and photoconductivity spectra
for: (a) a single-donor state below the conduction band
and, (b) both a donor state and an acceptor state.

the emission of the sample treated with $1 \times 10^{13}/cm^2$ stays at the same position
at 0.98 eV up to 120 K, and then shifts to 0.92 eV (which may be another peak)
(see Fig. 31).
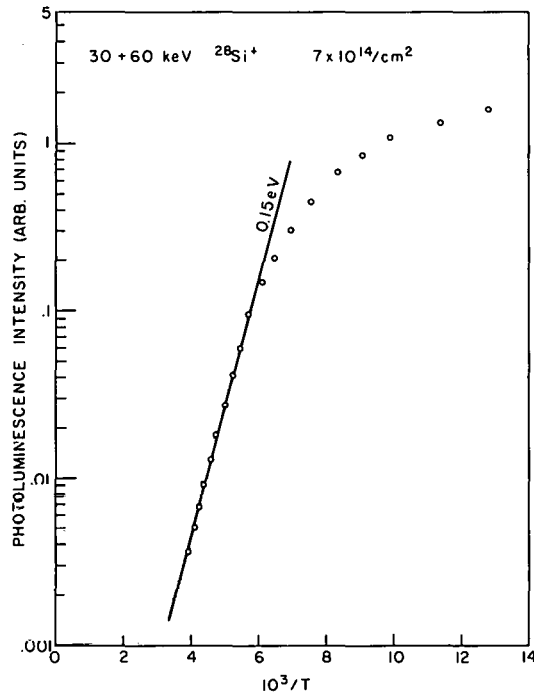
(a)
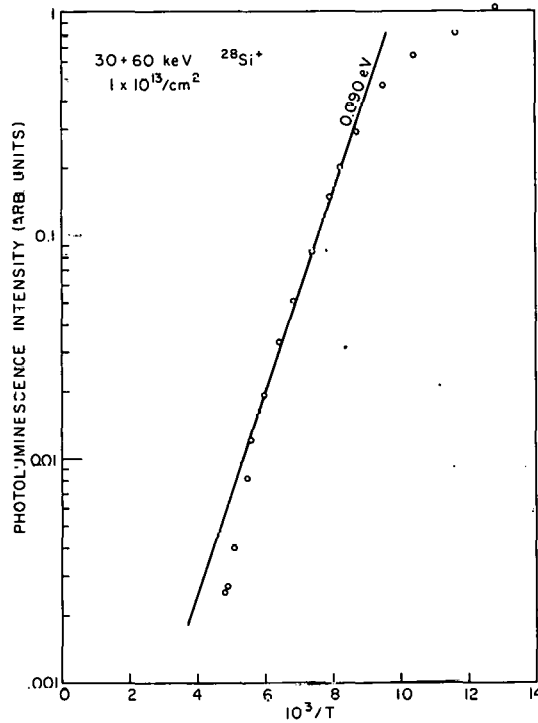


(b)

Figure 30.  Photoluminescence intensity as a function of $10^3/T$ for
ion-implantcd, hydrogenaled silicon after doses of
(a) 7 x $10^{14}/cm^2$ and (b) 1 x $10^{13}/cm^2$.
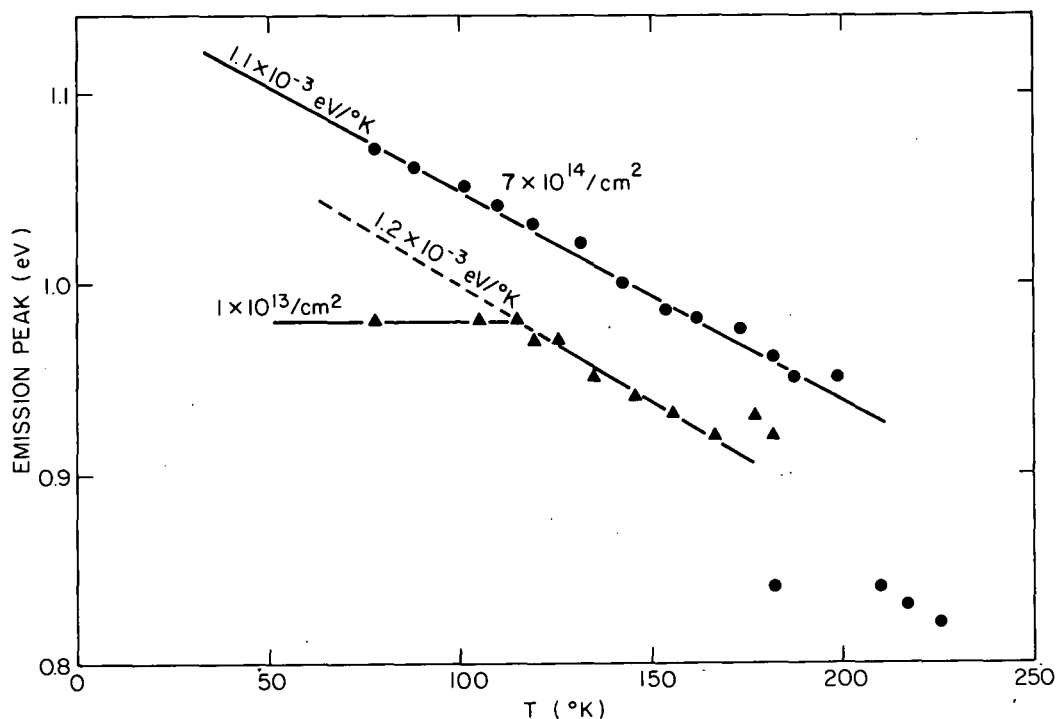
Figure 31. Peak emission energy as a function of temperature for ion-implanted, hydrogenated silicon for doses of $1 \times 10^{13}/cm^2$ and $7 \times 10^{14}/cm^2$.

## D. PHOTOELECTROMAGNETIC EFFECT

If a current of hole-electron pairs in a semiconductor or insulator flows by diffusion perpendicular to an applied magnetic field, an electric field appears mutually perpendicular to the pair flow and the applied field. This is called the photoelectromagnetic effect (PEM). If the PEM field is short-circuited outside the semiconductor, a PEM short-circuit current flows which is directly proportional to the diffusion length of the minority carrier. The PEM effect was used many years ago to estimate the diffusion length (and also the surface recombination velocity) in well-behaved semiconductors like Ge and Si, as well as insulating semiconductors like CdS. For insulating semiconductors with unequal hole and electron lifetimes the PEM effect is unique in measuring only the minority carrier lifetime ($L = \sqrt{D\tau}$), even in the presence of a much longer majority carrier lifetime. Since one of the major uncertainties in the use of a-Si:H in solar cells is the value of the minority-carrier diffusion length, the PEM method may be a useful diagnostic tool.

An attempt was made to detect the PEM effect in several samples of undoped or slightly n-type doped a-Si:H. Only "ohmic" contacts were used; there was no junction involved. The diffusion current was set up by illuminating with

51

strongly absorbed light from a xenon arc. A small electromagnet provided two to three thousand gauss magnetic field. Using an estimated diffusion length of 0.1 μm (Staebler and Wronski's original estimate) the calculated short-circuit PEM current would be about $10^{-12}$ A with a light intensity equivalent to one sun. Although the detecting system could have detected currents of this magnitude, no unambiguous signal was observed. If the diffusion length corresponds to Staebler's recent estimate of 400 Å, it probably could not have been observed.

One of the principal difficulties proved to be the "ohmic" contacts. When the light illuminates the contact area, even without a magnetic field, an open-circuit photovoltage is observed, which under some conditions is many times as large as the signal sought. This photovoltage is not a fixed quantity, but depends on the history of the contact. There appears to be a hysteresis effect which depends on the past history of applied field and its direction, together with the illumination. The apparatus is now being reconstructed to provide for a much higher magnetic field, an improved light source and a better sample shielding.

## E. THE PHOTO-HALL EFFECT IN UNDOPED a-Si:H

It has been stated by several investigators that photoconduction in undoped a-Si:H is due to electrons in the extended states lying immediately above the mobility edge, and there are theoretical arguments predicting that the mobility in these extended states might lie in the range 1 to 10 $cm^2V^{-1}s^{-1}$ [44,45]. Others conclude that the evidence for the existence of a mobility edge in a-Si:H is somewhat tentative [46]. The drift mobility for electrons has been measured to be about $10^{-2}cm^2V^{-1}s^{-1}$ at room temperature [47]. If one combines these results with photoconductivity measurements (lifetime and response time), then according to the usual phenomenological model [48], one indeed calculates an extended states mobility on the order of 10 $cm^2V^{-1}s^{-1}$.

44. P. G. LeComber, A. Madan and W. E. Spear, J. Non-Cryst. Solids 11, 219 (1972).
45. P. G. LeComber, W. E. Spear and D. Allan, J. Non-Cryst. Solids 32, 1 (1979).
46. K. Weiser, Comments Solid-State Phys. 6, 81 (1975).
47. A. R. Moore, Appl. Phys. Lett. 31, 762 (1977).
48. A. Rose, Concepts in Photoconductivity and Allied Problems (Wiley Interscience, New York, 1963.)

However, there is a strong possiblity that in a-Si:H, the neat distinction between traps (interchanging carriers only with the conduction band) and recombination centers may not be valid. We are now investigating whether such high-mobility carriers are present at all, and whether they can be detected by the Hall effect.

If $\mu$ ranges from 1 to 10, one would observe the correct sign for the electrons and the usual picture of an electron moving with thermal velocity can be applied even though its mean free path would only be a few interatomic distances. For $\mu \ll 1$, the measured sign of the carriers would be reversed if conduction takes place by hopping or tunneling in the band-tails, and this has been observed for highly doped n- and p-type a-Si:H [49,50]. In our experiments, one would want to measure the Hall effect under the maximum possible light intensity and at elevated temperature to increase the population of the high energy states.

In our first series of measurements, the signals were identified as a Hall effect by showing the proper reversals upon reversal of the current and magnetic field as well as by the linear dependence upon magnetic field up to 0.25 Torr. (At higher fields the signals saturated.) This series yielded n-type values of $\mu$ equal to $\sim 5$ $cm^2V^{-1}S^{-1}$ (with some values in the range 10 to 20 $cm^2V^{-1}S^{-1}$) upon illumination with $h\upsilon \geq E_g$. For two samples the signals were originally p-type, changing to n-type after light soaking.

The accuracy of these large values of $\mu_n$ is now in doubt for the following reasons:

(a)  Stray magnetic fields less than 1 G have been found to affect our Hg arc, causing spurious results with the same characteristics as the Hall effect.

(b)  The a-Si:H samples exhibit a magnetoconductive effect [51]; the magnetic field can either increase or decrease the lifetime of the photogenerated carriers. It is reported that for fields in the range 1 to 10 KG the photoconductivity changes by $\Delta\sigma/\sigma \sim 1\%$. If this effect is nonuniform over the sample area, the resulting potential changes may be larger than the Hall signal.

49.  L. Friedman, Philos. Mag. __38__, 467 (1978). D. Emin, Philos. Mag. __35__, 1189 (1977).
50.  P. G. LeComber, D. I. Jones and W. E. Spear, Philos. Mag. __35__, 1173 (1977).
51.  A. Mell, B. Movagher and L. Schweitzer, Phys. Status Solidi __88__, 531 (1978).

At this time, the method of our experiment is being reevaluated to see if it is at all possible to measure conduction in the extended states by means of the Hall effect.

F.   TUNNELING INTO a-Si:H

Fifteen years ago Gray [52] had demonstrated that information concerning the electronic states of a semiconductor can be deduced from the conductance-voltage (G-V) and capacitance voltage (C-V) characteristics of a MOS (metal-oxide-semiconductor) tunnel junction.  His ideas were extended [53,54] and were made a tool for the determination of the density, the energetic location, and the recombination time of semiconductors surface states [18,55].  The intensive study of amorphous semiconductors in the last decade had prompted many researchers to try to apply this tool with the hope that the G-V characteristics could be analyzed to yield information about the density of localized states in these materials [56].  The results of all these studies were rather disappointing since these characteristics were found to exhibit a universal symmetry and to lack any structure, even for elemental amorphous semiconductors, where a structure in the density of states distribution might be expected [56,57].  Thus, it appeared "that tunneling studies do not yield an easy answer to the question of localized state distribution, but instead they pose new and interesting problems" [57].  This universality of the G-V tunneling characteristics must be attributed to the two typical qualities of amorphous semiconductors, i.e., the high density of states in the gap and the hopping conduction mechanism in the bulk.  These two qualities were removed to a large extent in the dopable amorphous silicon-hydrogen alloy, a-Si:H, first investigated by Chittick, Alexander, and Sterling [1].  More recently, Spear and LeComber [15] have shown that doping with phosphorus makes the dominant conduction take place in the conduction band, and that

52.  P. V. Gray, Phys. Rev. 140 A179 (1965).
53.  J. Shewchun, A. Waxman, and G. Warfield, Solid-State Electron. 10 1165, 1187 (1967).
54.  L. B. Freeman and W. E. Dahlke, Solid-State Electron. 13 1483 (1970).
55.  S. Kar and W. E. Kahlke, Solid-State Electron. 15, 221 (1972).
56.  For many references and detailed data see J. W. Osmun, Phys. Rev. B11 5008 (1975).
57.  For a critical review, see H. Fritzche in Electronic and Structural Properties of Amorphous Semiconductors, edited by P. G. Le Comber and J. Mort (Academic Press, London, 1973) p. 55.

the density of states, g(E), (determined by field-effect measurement) is relatively low. Since they found a distinct structure in the density of states, it seemed reasonable to expect some structure in the tunneling characteristics.

The junctions prepared for this study were made by first depositing ~1100 Å of a-Si:H on a stainless-steel substrate. The material was prepared by decomposition of $SiH_4$ with 0.1% $PH_3$ in a dc proximity glow-discharge system with a substrate temperature, $T_s$, of 350°C. Films made under these conditions were found to have a resistivity of about 500-$\Omega$cm, in agreement with the resistivities obtained by Spear and LeComber for the same gaseous impurity ratio [15]. The films were oxidized for a few days in air at temperatures up to 150°C. The thickness of the oxide of the tunnel junction, the results of which will be reported here, was 24 Å. The oxide thickness was obtained by ellipsometry, where we used the $SiO_2$ refractive index for the oxide (1.45) and the recently determined optical constants of a-Si:H (n = 4.5 and $\kappa$ = 0.34). While it is likely that the oxide contains a significant amount of hydroxyl groups, we have found that its physical and chemical properties are similar to those of $SiO_2$. In particular, if we assume a dielectric constant of 4.0 for this oxide the thickness obtained from capacitance and ellipsometry were always in agreement with each other to within 20%. The top electrodes of the junctions were made by evaporating Cr dots, with an area A of 1 $mm^2$ and a thickness of 1500 Å. In the measurements we have employed the standard techniques of measuring the dc current vs voltage (I-V) characteristics [52,56] and of measuring the differential conductance (G-V) and capacitance (C-V) characteristics [55]. The latter quantities were determined by the in-phase and out-of-phase components of the current induced by a small (1 mV) ac test signal, and detected by a PAR model 124 lock-in amplifier. The voltage across the junction was gradually increased using a ramp generator (5 mV/s).

The I-V characteristics of junctions for which the oxide thickness, d, was between 20 and 30 Å was found to be asymmetric and a structure could be recognized between -0.1 and -1.0 V. This structure becomes more apparent if one takes the derivative of the I-V characteristic by numerical or electronic differentiation. The latter, obtained from the low-frequency G-V characteristic of the junction, is shown by the dashed curve in Fig. 32. As the frequency of the test signal is increased, a clear peak in the G-V
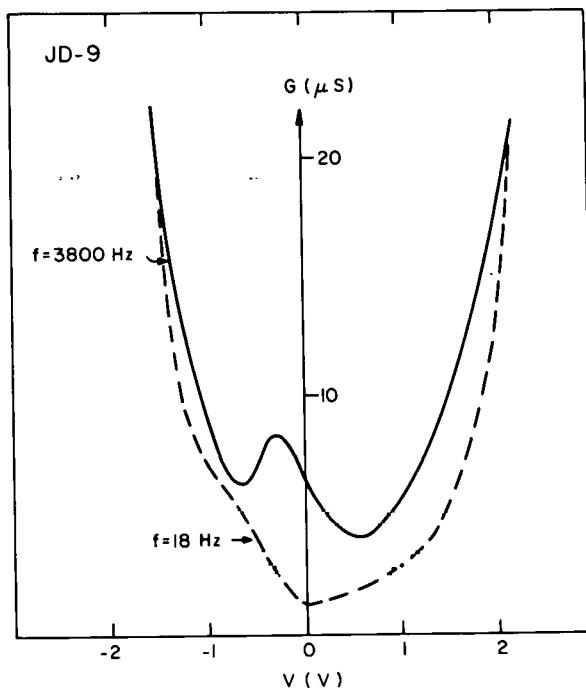
Figure 32. Conductance-voltage characteristics of a tunnel junction of phosphorus-doped hydrogenated amorphous silicon. The oxide thickness was 24 Å and the resistivity of the amorphous semi-conductor was 500 Ω-cm.

characteristic is revealed. This is shown by the solid curve in Fig. 32. Beyond the voltages $V_c$ = -1.50 V and $V_v$ = 2.25 V the characteristics become independent of frequency. As is apparent from Fig. 32, the resistance of the junction is $10^6$ Ω at V = 0. Comparing this with the corresponding MSM structure resistance, which is about 1 Ω, indicates clearly that the problem of the voltage drop across the bulk of the amorphous semiconductor [56] does not exist. The C-V characteristics, to be discussed elsewhere, have also shown a peak at -0.3 V. This peak was found regardless of the thickness of the oxide (as expected for the surface-state differential capacitance of an MOS structure) while the structure in the I-V and G-V characteristics disappeared for very thin oxides (<15 Å). The latter observation is due to the fact that in the thin-oxide case the tunneling into the conducting bands masks the tunneling into interface states [54]. All these observations are consistent with the tunneling-controlled mechanism [54] where the surface-state recombination time is much shorter than the tunneling time constant.

Since the features of the data shown in Fig. 32 are similar to those expected [53,54], and observed [52-55] in crystalline MOS structures, and since the density of surface states $N_s$, expected for the present material

(i.e., $g(E)^{2/3}$ using the data of Ref. 15), yields an $N_S$ distribution of similar magnitude and energy dependence as observed in crystalline MOS structures [18], we shall interpret our results according to the procedures [54,55] used for these structures.

To set the energy scale we must determine the applied voltages that correspond to tunneling into the conduction and valence bands. A good criterion is the frequency independence of such a tunneling process [53-55]. Using the theory of Ref. 53 with the dielectric constants of Si and $SiO_2$ for a-Si:H and the present oxide, respectively, we found that for positive voltages approximately 1/3 of the voltage drops across the accumulation layer, while for negative voltages approximately 5/6 of the voltage drops across the depletion layer (using d = 24 Å, $V_c$ = 1.5 V, $V_v$ = 2.25 V, and a carrier concentration, $n_b$, of $5.10^{15}$ $cm^{-3}$). We have assumed in this calculation (in accord with Ref. 15) a value of 5 $cm^2$/Vs for the extended states mobility (to deduce $n_b$), and a zero surface potential at V = 0. Away from the band edges, the theory [53] is not sensitive to variation of carrier concentrations in the range $10^{17} \geq n_b \geq 10^{15}$ $cm^{-3}$ to $N_S$ smaller than $10^{12}/cm^2$ eV, and to the assumption of zero surface potential. Since the ac conductance method, to be described below, is also not applicable close to the band edges [18], $E_c$ and $E_v$, our energy scale becomes less reliable as these edges are approached. However, using the theory of Ref. 53 we get $E_c$ - $E_F$ = 0.27 eV and $E_c$ - $E_v$ = 1.72 eV in good agreement with the values obtained in Ref. 15 for samples of comparable resistivity. Here, $E_F$ is the semiconductor's Fermi level.

The structure in the ac G-V characteristics is well known to represent the recombination-generation kinetics via surface states [52-55]. As the magnitude of the applied negative voltage increases, $E_F$ sweeps across the bandgap region $E_F \geq E \geq E_v$, while for positive voltages, $E_F$ sweeps across the region between $E_F \leq E \leq E_c$. Since it is easier and more common [53-55] to interpret these characteristics rather than the dc characteristics [54] we will use the former procedure to deduce $N_S(E)$. The relation between the surface density of states $N_S$ at a given energy E (or the corresponding applied voltage V) and the ac conductance associated with it, $\Delta G(V)$, is given by [18,54,55]:

$$N_S(V) = 2(\Delta G(V)/\omega)_m/qA \ , \tag{39}$$

where q is the electronic charge and $(\Delta G(V)/\omega)_m$ is the $\Delta G(V)$ to angular frequency ratio at the applied frequency (f = $\omega/2\pi$) for which this ratio has

its maximum. We could identify such maximas for voltages in the range $0.9 \geq V \geq -0.6$ V. Outside this range, but within the interval $V_v > V > V_c$ a rather univeral monotonic increase of G with $\omega$ was observed. Typical results for the two voltage regimes discussed are shown in Fig. 33(a) and Fig. 33(b). $\Delta G(V)$ was determined by subtracting the monotonic frequency-dependent background as shown in Fig. 33(a) from the measured conductance. As can be seen in Fig. 33(a) this was a small correction in the frequency range where maximas were found, $1000 \geq f \geq 40$ c/s. From results such as those shown in Fig. 33(b) we were able to map out $N_S$ as a function of the energy $E - E_F$ in the region $E_F + 0.1 \geq E \geq E_F - 0.5$ eV.

Although the results obtained by the procedure described above are strictly associated with the surface states, we present them in terms of $N_S^{3/2}$ vs $E - E_F$ in Fig. 34. This is done to make a comparison with the results reported in Ref. 15 (that were claimed to be associated with the bulk density of states $g(E)$). In addition, we show our $N_S^{3/2}$ vs $(E-E_F)$ results as obtained from the low frequency capacitance measurements using the well-known $N_S(V) = C_S(V)/qA$ relation [18]. In the latter measurements we were able to sweep a somewhat wider energy range. The agreement between our two sets of results is quite good and the difference between them is probably indicative of the error in estimating $N_S$.

While bulk density of states $N_S^{3/2}$ deduced from our $N_S$, and the bulk density of states, $g(E)$, deduced from field-effect measurements [15], might not be expected to yield the same states distribution, we see that the most distinct features of the two distributions above the midgap are quite similar.

From other field-effect measurements [58] and optical absorption measurements, it appears that increasing the amount of phosphorus or arsenic [58] doping enhances the peak in $g(E)$. Since it is known [59] that in crystalline silicon the vacancy-phosphorus complex yields an energy level at $E = E_c - 0.4$ eV this may not be surprising. We therefore believe that one may miss [3,21] the peak in $N_S(E-E_F)$ if the samples are undoped or very lightly doped.

58.   Z. S. Jan, R. H. Bube, and John C. Knights, to be published in J. of Elect. Mat.
59.   B. Henderson, Defects in Crystalline Solids Vol. I (Crane, Russak & Co., New York, 1972) p. 133.
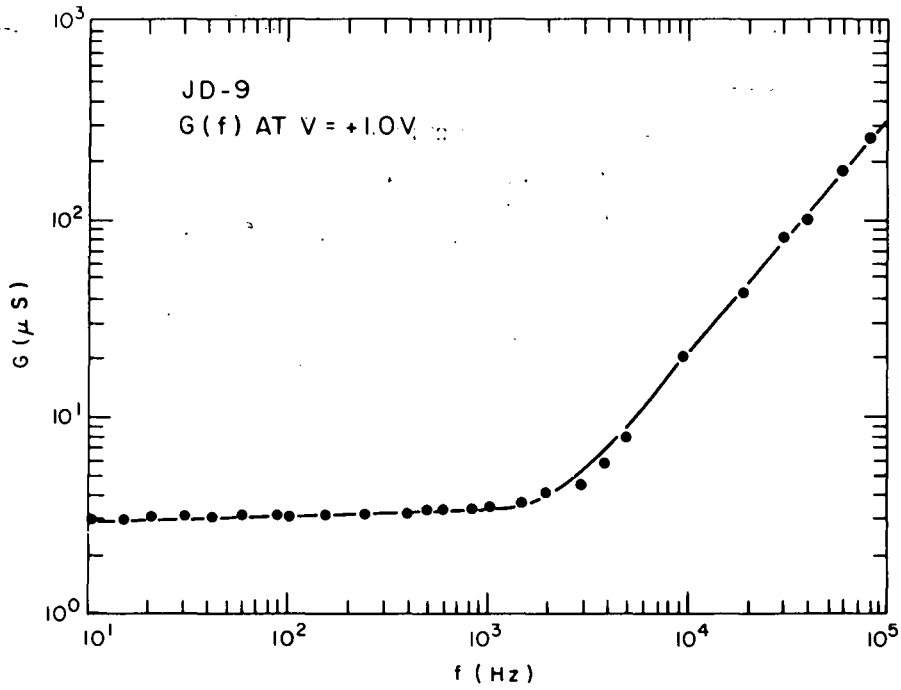
(a)
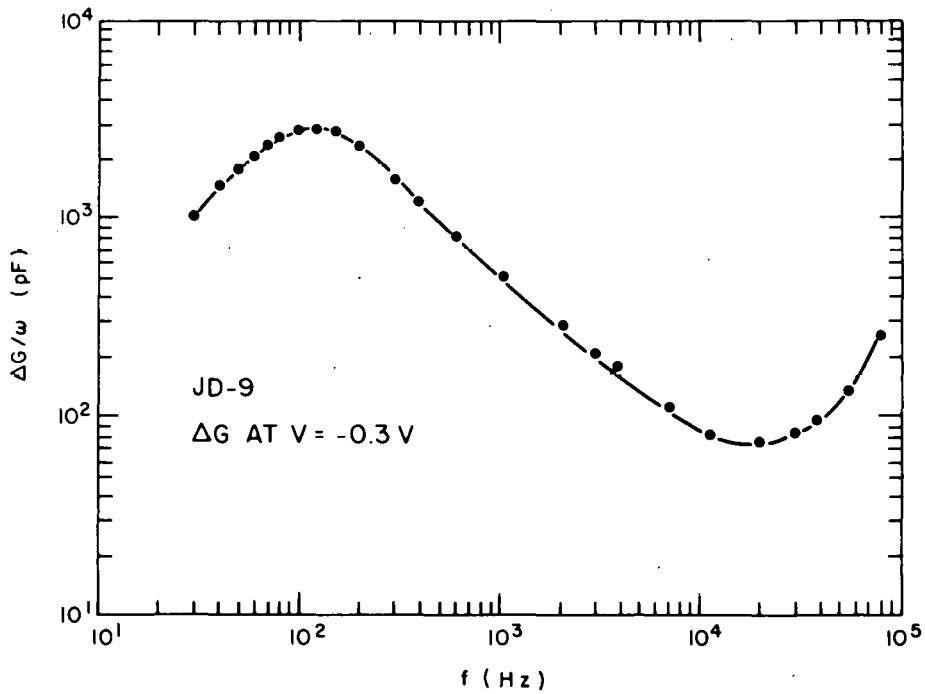


(b)

Figure 33.  (a) The frequency dependence of the tunnel junction conductance
at V = 1 V, and (b) the frequency dependence of the ratio of the
additional conductance (above the background) to the applied
frequency at V = 0.3 V.
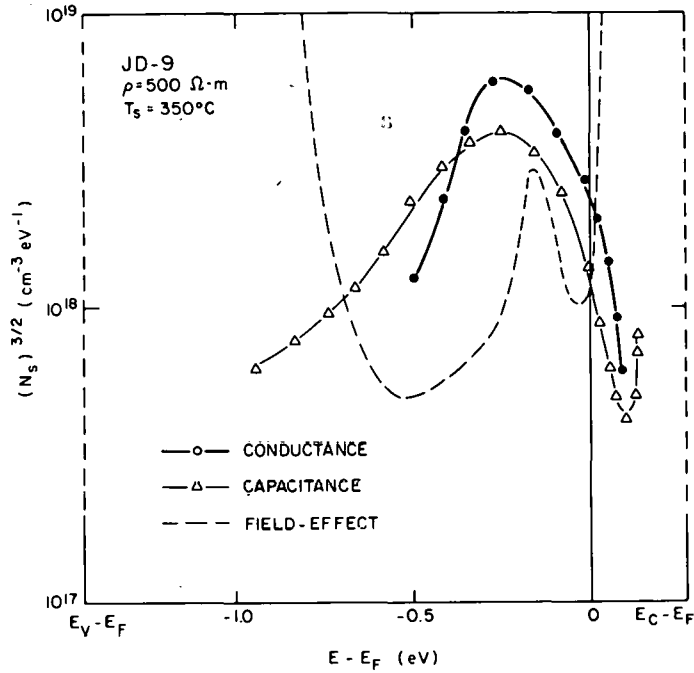
Figure 34. The energy dependence of $(N_S)^{3/2}$, where $N_S$ is the surface state density as determined from the G-V and the C-V characteristics of the tunnel junction. Also shown (dashed curve), the bulk density of states as deduced in Ref. 15 from field-effect measurements.

## G. SURFACE STUDIES - PLATINUM DEPOSITION

In this section we describe work which is directed toward an understanding on an atomic scale, of the clean, the oxidized, and the platinized surfaces of a-Si:H. The purpose is to characterize the processes by which the semiconductor-oxide-metal Schottky barrier is formed. For this purpose, an already existing bakeable, all-metal, ion-pumped, ultrahigh-vacuum chamber has been modified so that the following measurements can be made: Auger Electron Spectroscopy (AES), Low Energy Electron Diffraction (LEED), Electron Loss Spectroscopy (ELS), work function, adsorption and evaporation from the sample surfaces. In addition, the sample surface can be sputter-cleaned, illuminated by monochromatic light, cooled to liquid nitrogen temperature, and heated to about 600°C. Gas ambients of oxygen, carbon monoxide, and hydrogen are available. A platinum evaporator can deposit platinum at rates as slow as tenths of a monolayer per minute.

60

1.  The Deposition of Platinum on Single-Crystal Silicon

The problem of absolute quantitative measurements of adsorbed atoms by AES has been, and remains, a difficult and complicated one. Although some theoretical attempts have recently been discussed, the best and most fool-proof approach is empirical. We have, therefore, begun our work with the adsorption of Pt on single-crystal silicon to "calibrate" the process.

A (111) surface of silicon was sputter-cleaned and annealed at 950°C to produce a well-defined characteristic LEED pattern. Platinum was then eva-porated onto this surface by heating a helical filament of Pt to 1500°C for fixed times. The buildup of Pt is shown in Fig. 35 where we plot the peak-to-peak magnitude of the 64-V Pt Auger line and the 92-V Si Auger line vs Pt evaporation time. Initially, there is a simple linear increase and de-crease of Pt and Si, respectively. At a certain breakpoint, both these behaviors change, and subsequently show a leveling off. During these measurements the LEED behavior showed only a constant, overall dimming of the Si substrate LEED spots until the entire LEED pattern disappeared just at the point where the linear rates of change stopped, as shown in Fig. 35. There is no new LEED pattern introduced by the Pt overlayer. We infer that during the initial linear portion of these curves, Pt is building up to a coverage, $\theta$, of one monolayer, and that the point at which we depart from linearity and when the Si substrate LEED pattern disappears corresponds to one complete atomic over-layer of Pt. We will take this value of the Pt Auger line (suitably adjusted for the overall system gain) as that corre-sponding to one monolayer, $\theta = 1$, and $7 \times 10^{14}$ Pt/cm$^2$ (i.e., the (111) Si planar atomic density).

Note in Fig. 35 that while the saturation of the Pt line is only to be expected, the nonzero saturation of the Si line might be considered surprising. Actually, this furnishes a strong clue to the overgrowth mechanism of Pt on single-crystal Si, as follows: the fact that in Fig. 35 the Pt Auger line in-creases linearly and the Si Auger line decreases linearly until the LEED pat-tern disappears, indicates that one monolayer of Pt has formed. The fact that beyond this point the Si does not go to zero suggests that subsequent Pt growth does not cover the entire area of the Si substrate with successive layers of Pt, i.e., there are islands of Pt growing atop the first monolayer of Pt. This is the so-called Stranski-Krastanov mechanism, and is shown schematically in

GROWTH OF Pt ON (III) Si
o 64V Pt AUGER LINE
x 92V Si AUGER LINE
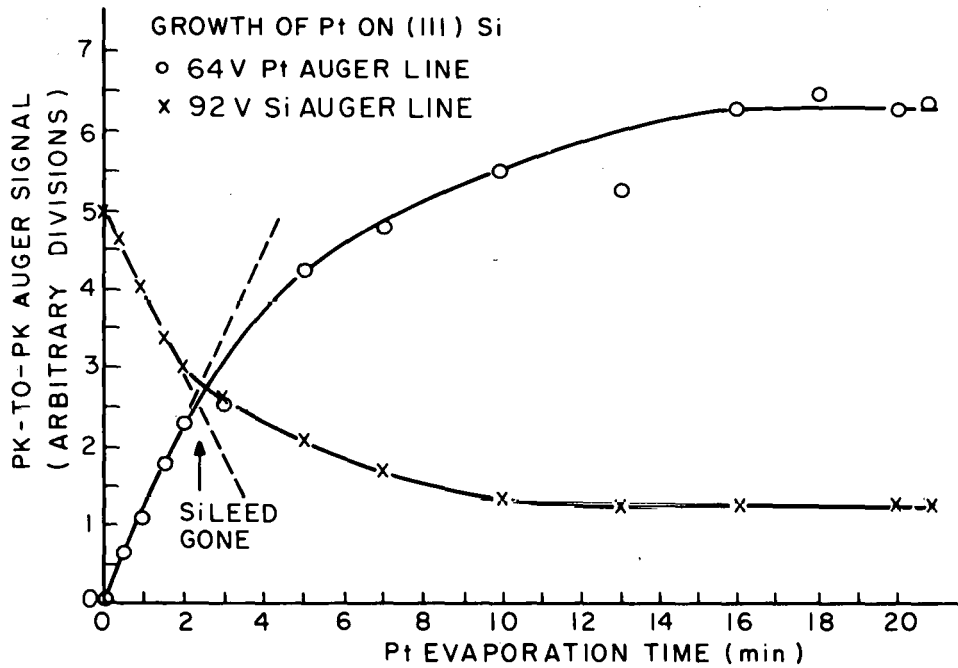
Figure 35.   Growth of 64-V Pt Auger line and decrease of 92-V Si Auger
line with Pt evaporation on single-crystal Si (111).

Fig. 36(a). Ultimately, if we were to wait long enough, the islands would in-
crease in size and "fill in" the spaces, but at the times and temperatures
used for Fig. 35, this has clearly not yet occurred.
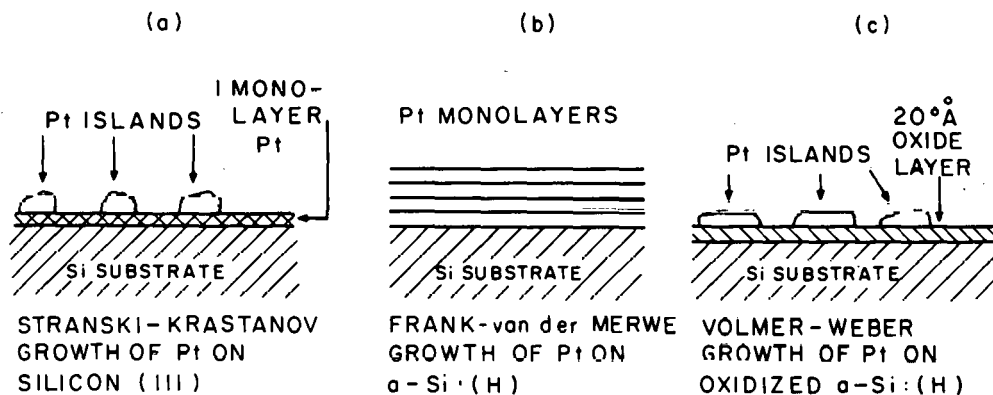


Figure 36.   (a) The Stranski-Krastanov thin film.   (b) The Frank-van
der Merwe growth of Pt-thin films on a-Si:H.   (c) The
Volmer-Weber growth mechanism.

We tested the model of Pt islands on a first Pt atom layer by heating the crystal to 450°C for a short time. (At this temperature Pt does not evaporate, nor is there any interdiffusion between the Si and Pt.) The results are shown in Fig. 37 where the marked decrease in the 92-V Si line is interpreted in terms of the Pt islands "spreading out" and filling in the spaces between them, thus covering up more of the Si. Note the small silicide line at 80 V just beginning to grow as a result of the heating.

PLATINUM ISLANDS "SPREADING OUT" WITH TEMPERATURE

AFTER Pt
DEPOSITION
AT RM. TEMP.

HEATED 30 Secs.
AT 450° C.

HEATED 60 Secs.
AT 450° C.

AUGER SIGNAL

VOLTS (V)
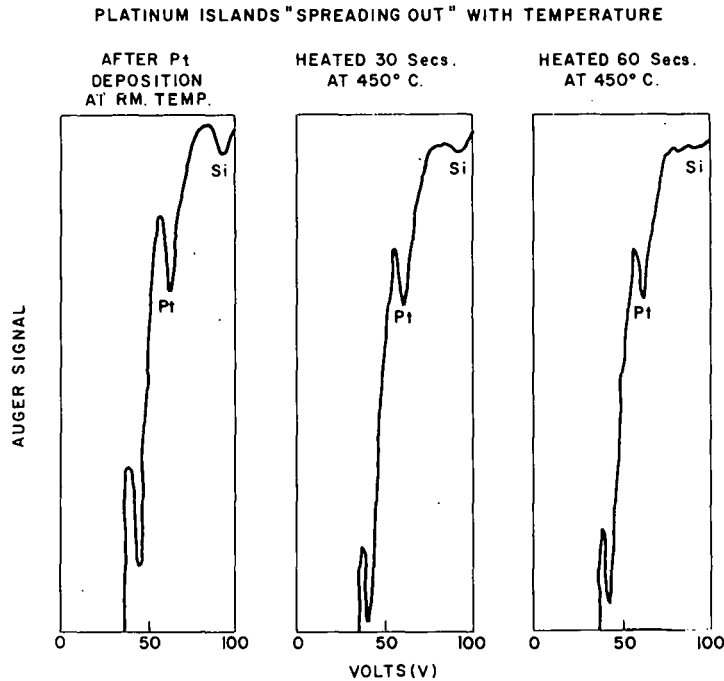
Figure 37. "Spreading out" of Pt islands with temperature. The Si de-
creases as the Pt migrates on the surface and fills in the
spaces between the islands. Note the onset of the small
80-V silicide Auger line.

2. The Deposition of Platinum on a-Si:H

Having quantitatively calibrated our Pt deposition, we then turned to studies of Pt on a-Si:H. The a-Si:H samples were deposited on a polished molybdenum substrate in a silane discharge system. They were 1.3 μm thick. The samples were chemically cleaned, mounted in the vacuum chamber, and, after baking out, sputter-etched until trace carbon was the sole contaminant seen on the surface by Auger analysis. After each sputter-cleaning the sample was heated to 300°C for 20 min. This was done not only to try to desorb volatile atoms (like argon) but also to try to establish as reproducible a surface as possible for each experiment.

A serious problem of sample charging by the Auger primary electron beam was initially encountered. This problem was overcome by thinning down the sample (by sputter-etching) to about 8000 Å, at which point even very small Pt depositions would remove all traces of sample-charging. A second serious problem of electron-beam-enhanced $O_2$ adsorption was eliminated by using low beam currents (5 μA) and a cryopanel which condensed out residual gases in our system.

In Fig. 38 we show the growth of Pt deposited on a clean a-Si:H substrate, again by heating the Pt evaporator for various times at a fixed temperature. When we compare Figs. 38 and 35, we find that while the initial behavior is qualitatively the same, i.e., a linear increase of Pt and a linear decrease of Si, beyond the one monolayer point there are significant differences. First, there is a sharp break in the Si decrease at one monolayer beyond which point, for a-Si:H, the Si continues to decrease (at a slower rate) until it disappears. Second, Pt continues to increase linearly past the one monolayer point until about five monolayers are deposited, and only then does it begin to round off and saturate.
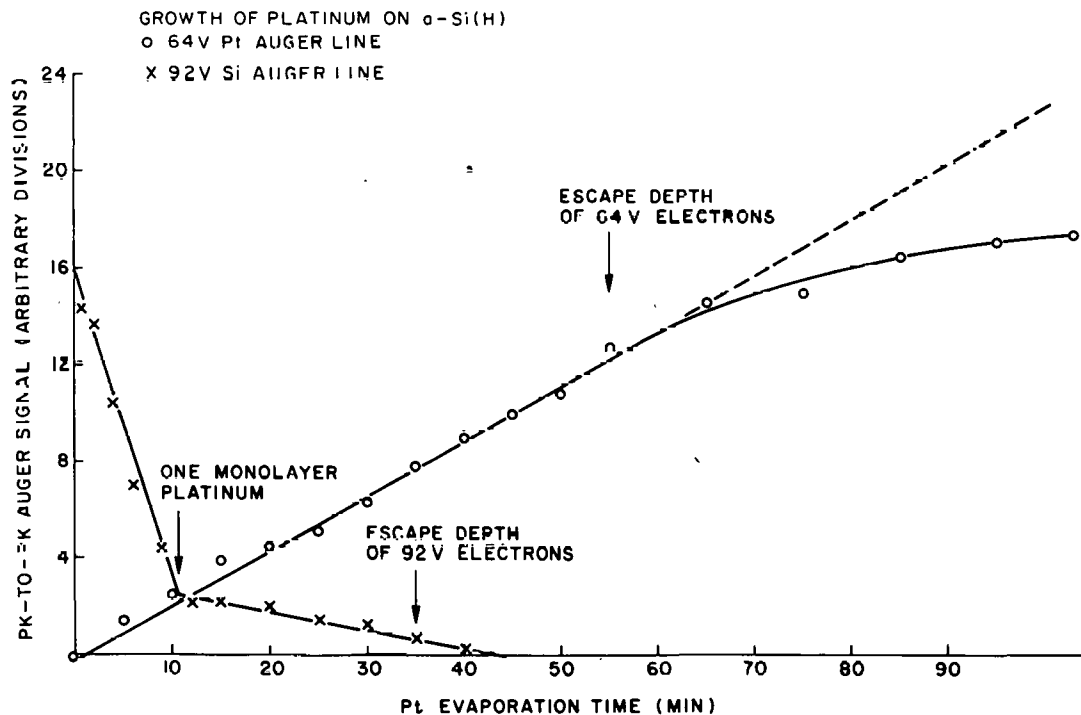


Figure 38.  Growth of 65-V Pt Auger line and decrease of 92-V Si Auger line with Pt evaporation on a-Si:H.

Both the Si and Pt behaviors described above and shown in Fig. 38 qualitatively suggest that Pt adsorbs on a-Si:H in complete monolayers - the so-called Frank-van der Merwe process which we show schematically in Fig. 36(b). Adsorption in the form of complete monolayers was strongly substantiated by correlating the thickness of the Pt deposit to the escape depths of the 64-V Pt Auger electron ($\sim$6 Å in Pt) and the 92-V Si Auger electron ($\sim$4 Å in Pt). These points are indicated in Fig. 38.

## 3. Plasmon Losses

One of the more valuable surface physics techniques that have been developed in recent years is Electron Loss Spectroscopy. In this technique a primary electron beam of relatively low energy ($\sim$100 V) is directed at a surface, and the back-scattered electrons are examined in the energy region just below the elastic peak. In this energy region are to be found the electron energy losses corresponding to electronic excitations characteristic of the surface, e.g., surface plasmons and surface-state transitions.

In Fig. 39 we show the characteristic losses of the a-Si:H surfaces corresponding to the experimental conditions of Fig. 38 using a primary electron-beam energy of 98 V. At first, in curve (a), we see only the characteristic bulk and surface plasmon losses of Si. No surface-state transitions are observed. In curve (b) we have deposited 0.25 monolayer of Pt. Even at this relatively low coverage, note that the Si surface plasmon has been washed out leaving only the bulk plasmon. The appearance of this loss spectrum then remains essentially unchanged throughout increasing Pt coverage, until several monolayers of Pt have completely suppressed the characteristic losses of Si, at which point the characteristic losses of pure Pt are seen as in curve (c).

The losses in curve (c) for 9 monolayers of Pt are in excellent agreement with the literature for bulk Pt. From them we can deduce an effective number of electrons per atom of Pt which participate in the collective oscillation which forms the plasmon, as follows: the formula for the energy of the bulk plasmon is

$$E = \hbar \left( \frac{4 \Pi n e^2}{m} \right)^{1/2} \tag{40}$$

where n is the number of electrons per $cm^3$ forming the plasma, and m is the electron's effective mass. This reduces to

$$E(eV) = 3.68 \times 10^{-11} \sqrt{n} \tag{41}$$
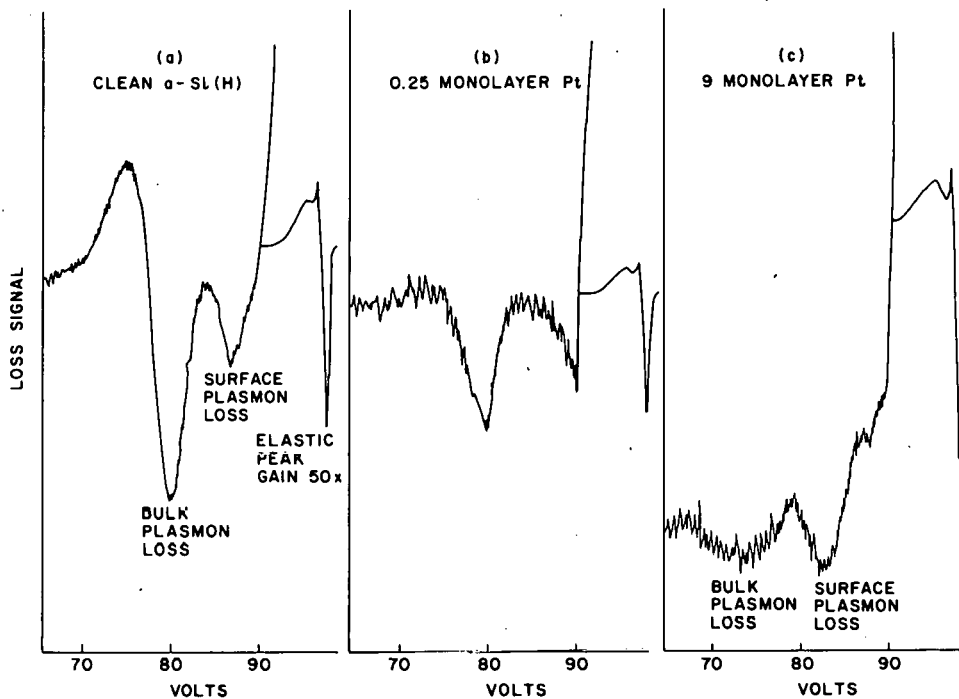
Figure 39.  Characteristic losses of clean and platinized a-Si:H.
The elastic peak in all three cases is taken at 1/30
times the gain of the plasmon loss peaks.

Taking $E = 24$ V (from curve (c), Fig. 39) we calculate n to be $43 \times 10^{22}$ el/cm$^3$.
Knowing Pt to be face-centered-cubic with a lattice constant of $3.92 \times 10^{-8}$ cm,
we calculate that there are $6.6 \times 10^{22}$ atoms/cm$^3$. Thus, there are 6.5 electrons/
atom forming the plasma whose oscillations have quanta of 25 eV. Note that
this number is consistent with the fact that the outer electronic structure
of Pt consists of one S electron and nine D electrons - the S and D shells
being relatively close in energy as witnessed by platinum's 78th electron
going not into the outermost S shell but the next inner D shell. Thus, one
might expect that the effective number of plasma electrons per atom to be
between 1 and 10, hence the plausibility of the 6.5 figure.

4.  Deposition of Platinum on Oxidized a-Si:H

Since the final form of the Schottky-barrier solar cell is a Pt film on
a thin oxidized layer of a-Si:H (i.e., an MIS structure), the measurements
described in Sections IV.H.1 and IV.H.2 above were repeated on a-Si:H which
had been oxidized in room ambient to thickness of about 20 Å as measured by
ellipsometry.

Figure 40 shows typical Pt growth behavior on oxidized a-Si:H. The in-
crease in the Pt Auger line with Pt deposition time appears to be the same

66

GROWTH OF Pt ON OXIDIZED a-Si:H
o 64V Pt AUGER LINE
x 80V OXIDE Si AUGER LINE
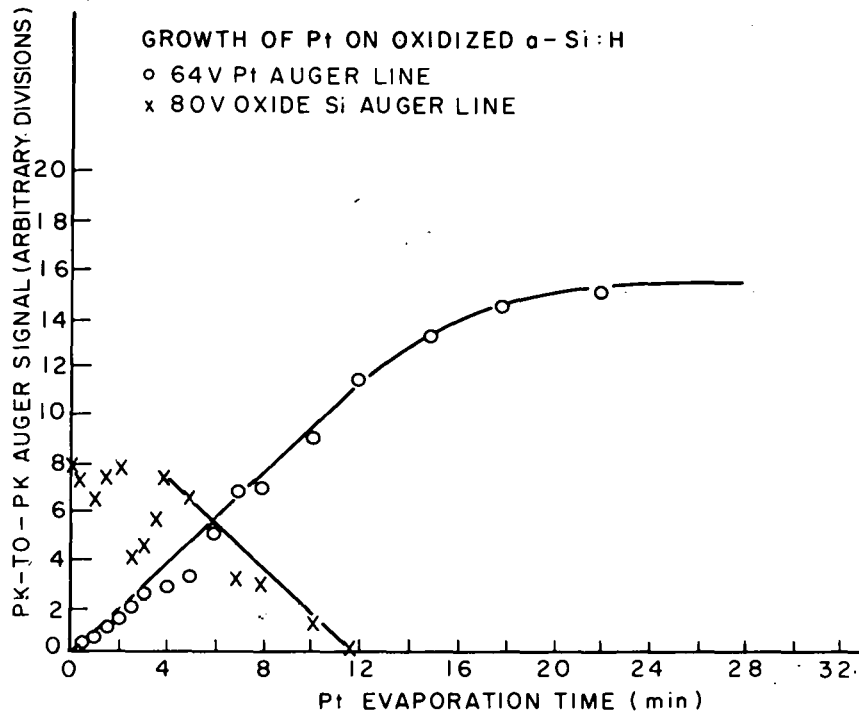
Figure 40. Growth of 64-V Pt Auger line and decrease of 92-V
Si Auger line with Pt evaporation on oxidized a-Si:H.

as in clean a-Si:H, i.e., a linear growth ultimately showing signs of satura-
tion. However, changes in the Si Auger line during the initial Pt growth
period displayed a consistently erratic behavior characterized by sudden in-
creases (as typified by the curve in Fig. 40) rather than by a steady decrease
with Pt deposition.

We suggest that this behavior is due to a modified Volmer-Weber type
growth mechanism, schematically illustrated in Fig. 36(c). At coverages of
less than a monolayer, Pt atoms initially adsorb uniformly. When their density
reaches certain critical values they agglomerate to form islands and, hence,
produce erratic shadowing of the substrate Si atoms*. After about a monolayer,
this effect would be expected to diminish markedly. We tried to test this
hypothesis by adsorbing Pt at liquid nitrogen temperature where the atomic
mobility of Pt should be considerably less than at room temperature. The
behavior at low temperature was exactly the same as that characterized by
adsorption in complete monolayers (as in Fig. 38) with no erratic behavior

---

*This effect would be much less noticeable for the 512-V oxygen Auger line.

67

in the decrease of the Si Auger line. Furthermore, if we adsorb Pt at low temperature to a point where the Si Auger line has almost disappeared, then heat the sample to room temperature, we find that the Si Auger line has increased by a factor of four, while the Pt Auger line has changed only negligibly. This would be consistent with Pt island formation when, as described above, there is sufficient thermal energy to allow surface migration. If our Pt agglomeration hypothesis is correct, it would mean that the interfacial energy between Pt and the oxide of a-Si:H is less than that between Pt and clean a-Si:H.

## H. SURFACE PHOTOVOLTAGE, BAND-BENDING AND SURFACE STATES ON a-Si:H

### 1. Introduction

In this section we describe studies which are directed toward determining the properties of the surface states on a-Si:H. These include location (in energy), number, optical activity, behavior with temperature, and effects of oxygen and platinum adsorption. Our principal experimental technique is surface photovoltage spectroscopy and consists of measuring the band-bending, more precisely, the change in band-bending by means of monitoring the difference in contact potential between the a-Si:H surface and a stable reference electrode.

The samples used for these studies were $0.5-1.0-\mu$ films made by deposition at 325°C from a glow discharge in silane. Two types of samples were studied. One was lightly phosphorus-doped by the addition of 0.1% $PH_3$ in the $SiH_4$ discharge. It was of relatively low resistivity and was characterized by a room-temperature activation energy of 0.4 eV. The second was intrinsic (i.e., not intentionally doped), of much higher resistivity, and was characterized by a room-temperature activation energy of 0.7 eV. The samples were chemically cleaned, mounted in an all-metal vacuum chamber sputter-cleaned and heated 200-250°C for 20 min before beginning any set of experiments. This last step was included to evaporate any volatile surface contaminants and also to have as reproducible a starting condition as possible before beginning any given sequence of measurements.

### 2. Band-Bending and the Surface Photovoltage

In Fig. 41, we illustrate schematically the relationship between band-bending and the surface photovoltage (SPV). In Fig. 41(a) is shown an n-type
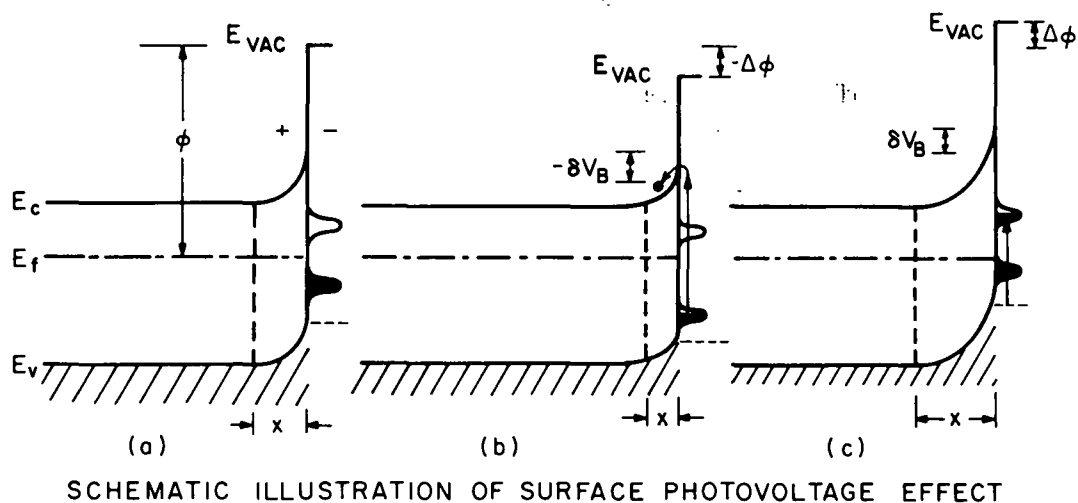
Figure 41.  Schematic illustration of the relationship between the
surface photovoltage and band-bending.

semiconductor with both filled and empty surface states in the bandgap.  The
states below the Fermi level have been filled by electrons from the region
of the semiconductor adjacent to the surface, thus producing a space-charge
region, $\chi$.  The net surface dipole produces, in turn, band-bending as shown
and a Schottky barrier with height, $V_B$.  If light of appropriate wavelength
now changes the equilibrium electron population of the surface states, then
the surface charge, space-charge region and barrier height will change ac-
cordingly.  This change in barrier height is called the surface photovoltage
(SPV).  Electronic transitions which empty surface states flatten the bands
[Fig. 41(b),], while those that fill surface states increase the band-bending
[Fig. 41(c)].

We measure changes in the band-bending (SPV) by using a Vibrating Kelvin
Probe which directly measures the change in contact potential $\Delta\phi$ between a-Si:H
and a vibrating gold electrode.  This has the advantage of not having to touch
the surface under study.  The frequency of the vibrating electrode is 630 Hz,
and a feedback circuit which measures the bucking voltage required to keep the
contact potential difference at zero enables us to continuously record the
change in band-bending and SPV*.

_____

*We are indebted to A. White of RCA Laboratories for the design and construction
of this circuit.

3. Phosphous Doped a-Si:H

a. Surface Photovoltage Measurements

One of the prerequisites for observing an SPV is that the surface states whose electron population is changing be sufficiently decoupled electronically from the valence and conduction bands. (A preliminary indication that an SPV might be observable at low temperature for a-Si:H was the finding that electron loss spectroscopy measurements on these surfaces were sensitive to light [60]). Such decoupling is, of course, more likely for wide bandgap materials. That this decoupling exists for a-Si:H is demonstrated in Fig. 42, where we show some of the basic SPV behavior.

When P-doped a-Si:H is cooled in the dark to -168°C, and then illuminated, a SPV, $-\Delta\phi$, is developed whose polarity indicates band-flattening, see Fig. 42(a). After equilibrium is reached, removing the illumination does not restore the surface to its dark condition. There is only about a 20% recovery and the bands remain flattened. We have changed the population of the surface states, and only at higher temperature does the population return to its dark value as in Fig. 42(b). Some thermal energy is evidently required for the "restoring" electronic transitions (i.e., "filling" transitions, Fig. 41(c)) to occur. Note, however, in Fig. 42 that heating in the dark and then cooling also restores the surface to its original state.

In Fig. 43 we show some wavelength dependence curves of the SPV ($\Delta\phi$) for isophotonic illumination at three temperatures. At -168°C, $\Delta\phi$ (after the initial illumination) is very small (see Fig. 42). At -90°C, $\Delta\phi$ is larger and at -55°C, $\Delta\phi$ is again small. The polarity change at -168°C is real and indicates that both filling transitions and emptying transitions are possible (although, as we shall see, when the surface states are filled the dominant optical transitions are emptying ones). The structure between 0.6 and 1.0 eV is reproducible and is not due to optical fringe effects since we have made these measurement above and below the Brewster's angle and have obtained the same results. We will discuss this structure shortly.

In Fig. 44 we show the temperature dependence of $\Delta\phi$ at different wavelengths above, at, and below the optical gap. Consistent with the behavior suggested in Fig. 43, there is first an increase in $\Delta\phi$, followed by a region in which $\Delta\phi$ decreases to zero. It is to be emphasized that curves a-d are

60. J. Derrien et al., Appl. Phys. Lett. 33, 881 (1978).

BASIC SURFACE PHOTO-VOLTAGE BEHAVIOR
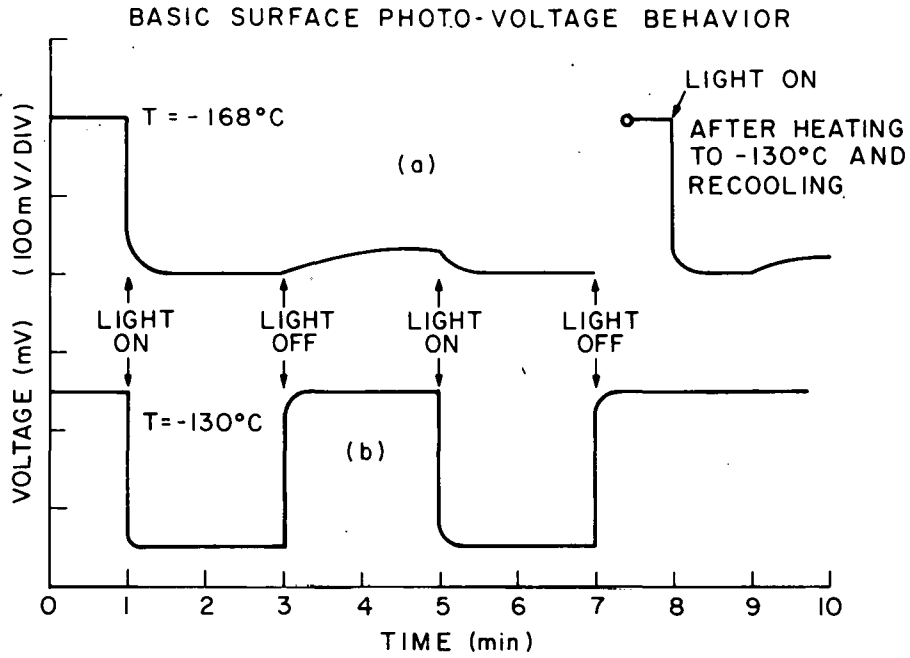
Figure 42. Typical surface photovoltage behavior of a-Si:H at -168°C
and -130°C. Note effect of temperature on "restoring"
the surface to its dark condition.
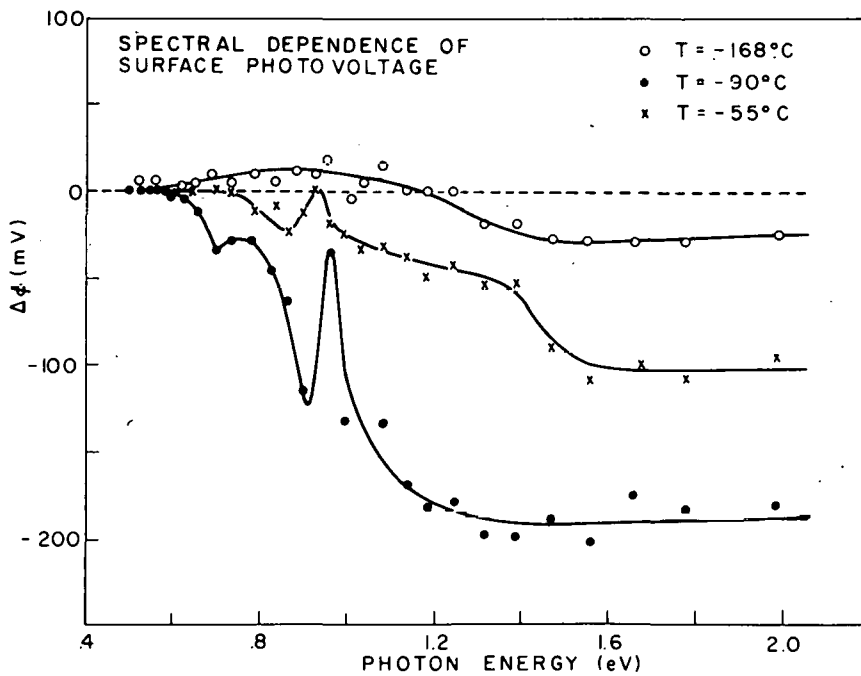


Figure 43. Spectral dependence of surface photovoltage of a-Si:H at
different temperatures. The structure between 0.5 and
1.0 eV is not due to optical fringe effects.

71
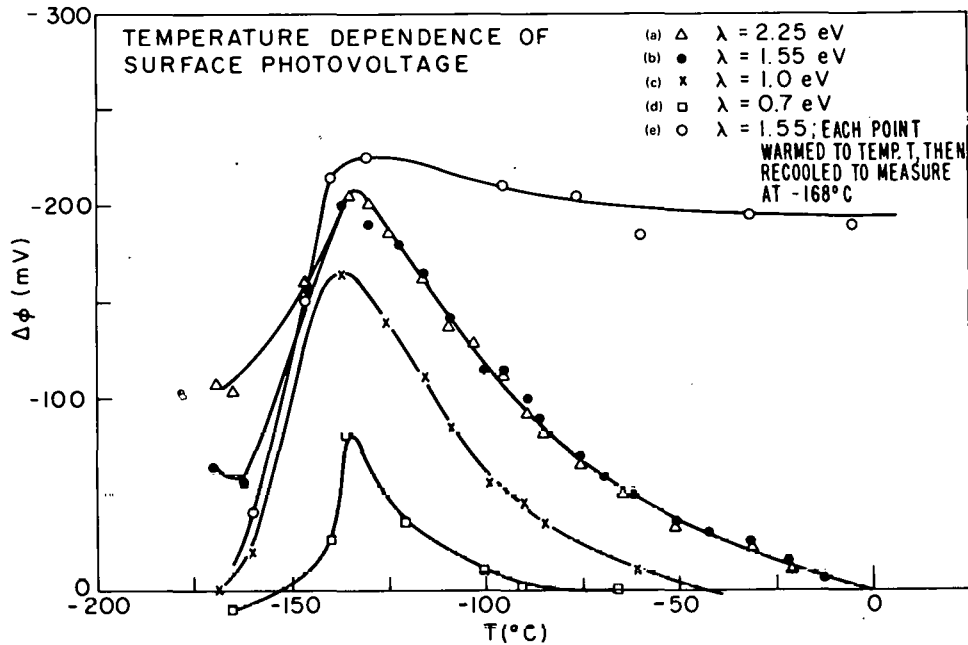
Figure 44.  Temperature dependence of surface photovoltage; curve (e)
illustrates the "freezing in" at -168°C of the situation
produced at the higher temperature T.

for Δφ whose values were obtained with successive "light on-light off" meas-
urements as the temperature is increased.  The first measurement at -168°C
would be considerably greater (see Fig. 42) than the Δφ at -168°C plotted
in Fig. 44.  Curve (e) in Fig. 44 was, on the other hand, obtained by heating
to temperature T, and then recooling in the dark to -168°C for the Δφ measure-
ment.  Now there is only little decrease in Δφ once the peak temperature of
curves (a-d) has been exceeded.  By measuring at -168°C instead of at the
higher temperatures, we have "frozen in" the surface-state conditions pro-
duced at the higher temperatures.  We take this curve, i.e., curve (e)
Fig. 44, to be a truer picture of the effect of temperature on the surface-
state electron population.

This being the case, we show in Fig. 45 the wavelength spectrum of Δφ
in which for each point the sample was heated to -130°C, i.e., past the peak
in Fig. 44, and then cooled to -168°C prior to measurement.  Note that this
curve has the character of the higher temperature curves of Fig. 43.  This is
only to be expected since we have "frozen in" at -168°C the conditions obtained
at -130°C.  Ordinarily, one might take the structure seen between 0.5 and 1.0
eV as directly reflecting some electron or energy level distribution since the
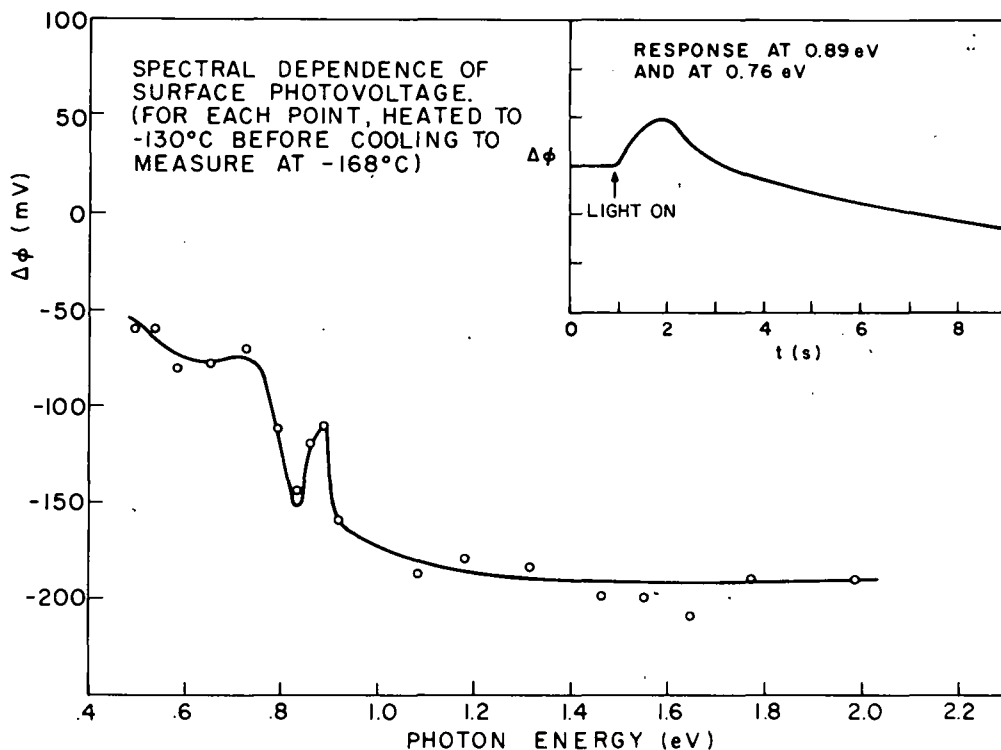
Figure 45.  Wavelength dependence of surface photovoltage after "freezing in" the high-temperature surface-state electron population by heating to -130°C and then recooling to -168°C before each point.  The inset shows the response with time which indicates both filling (+Δφ) and emptying (-Δφ) transitions.

Δφ we measure indicates a surface-state emptying transition.  However, we found that this was not the case; the structure at 0.76 and 0.9 eV is, in fact, due to two (or more?) electronic transitions which occur simultaneously and which produce Δφ's of opposite sign.  A recorder trace of this Δφ response is shown in the inset of Fig. 45.  Apparently, photons of appropriate energy can both fill and empty surface states.  We consider it not surprising that we see this effect most strongly at energies below the optical gap, away from the pervading effects of the fundamental absorption.

The rise time of the surface-state emptying transition (-Δφ) seen in the inset is very long, ∿2 min.  This strongly suggests that there is a thermal step in this transition.  The time constant, however, is neither a simple exponential nor a power law and, while it does decrease with increasing temperature, an analysis of it could not be made.  At photon energies greater than about 1 eV the time constant of -Δφ is much more rapid, ∿1 s.

We suggest that this occurs because the photons now have sufficient energy to bypass the thermal step.

The intensity dependence of the surface photovoltage $\Delta\phi$ is given in Fig. 46. The upper curve was taken at -168°C after heating to -130°C and recooling before each point (the lower three curves are shifted down one decade for clarity). It was taken at an energy of 1.55 eV because this was one energy which did not appear to produce multiple electronic transitions like those discussed in Fig. 45. It was felt that an intensity dependence curve at photon energies which produced multiple electronic transitions would provide data of dubious value in clarifying mechanisms and models. At -108°C, however, illumination at all energies gave similar behavior with no signs of multiple transitions. The significant features of the curves in Fig. 46 are a surprisingly extensive region of saturation extending over 2-4 orders of magnitude of intensity, followed by a logarithmic decrease with a slope of about 0.5, i.e., $\Delta\phi$ varies as $(\text{intensity})^{1/2}$. The photon flux exiting from our monochromator at 100% transmission is about $2 \times 10^{15}$ cm$^{-2}$ s$^{-1}$ (not particularly high) so that the saturation suggests either a low density of surface states and/or a very high capture cross section for photons. The square-root dependence, once saturation is over, indicates bimolecular kinetics for the surface-state emptying transition. These points are discussed in greater detail when we discuss the energy level diagram and the nature of the electronic processes involved.

b.  Bulk Photoconductivity Measurements

In dealing with surface photovoltage effects one of the questions that must be unequivocally answered is whether the surface photovoltage is produced by bulk transitions which produce carriers that can change the surface charge either by migration to the surface or by directly affecting the space charge in the barrier region. In order to answer this question, we have examined a property of this material that we know depends on bulk electronic transitions, that is, the bulk photoconductivity. In order to make such measurements without adding any contacts to the a-Si:H surface, the experimental arrangement illustrated in Fig. 47 was evolved and works as follows: the electron beam of our Auger apparatus, operating with an energy of 25 V and a current of 1 μA is directed onto the a-Si:H surface. A bias voltage is then applied to the sample in a standard retarded-beam configuration so that as the bias voltage approaches the beam voltage, the current flowing in the
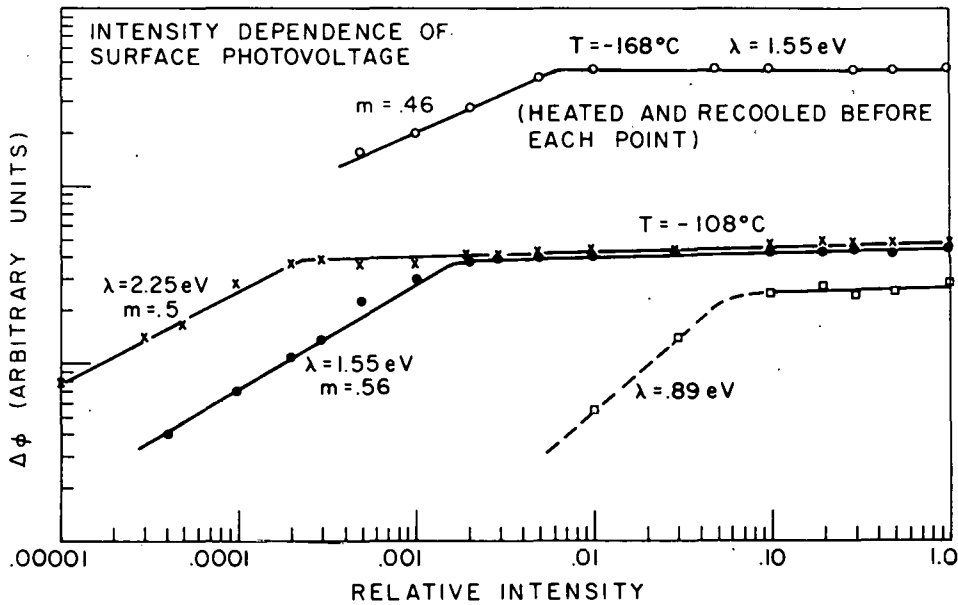
Figure 46.   Intensity dependence of the surface photovoltage.  The
             curves at -108°C are displaced one decade for the sake
             of clarity.  The saturated value at -168°C is about 0.22 V.
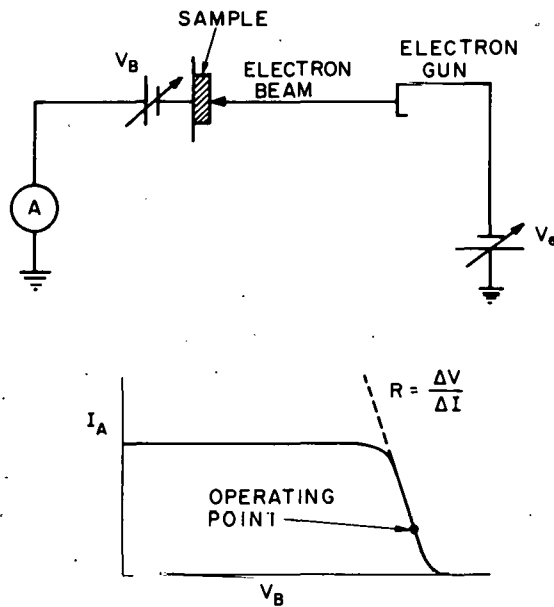


Figure 47.   Scheme for measuring bulk photoconductivity.

sample circuit will decrease as shown in the bottom of Fig. 47. We then characterize the straight line that approximates the decreasing current by a resistance given by $\Delta V/\Delta I$. If we now set $V_B$ at the operating point, we find that illuminating the sample (at low temperatures) increases I and decreases R. Thus, the electron beam itself acts as the "contact"; it strikes the surface with a (negligible) energy ~2-3 V that can be expected to cause no damage and penetrates ~1-2 atom layers. This system was successfully checked out by putting known resistances in the sample circuit, using a piece of metal in place of the sample, and determining a fixed value of 0.91 MΩ as the "equivalent" resistance associated with the electron beam. In Fig. 48 we show three such I-V curves for an a-Si:H sample at different temperatures and illumination conditions which demonstrate the basic ideas of the technique. The resistances given should have subtracted from them the resistance of the circuit when a metal replaces the a-Si:H. The only caution we have found necessary to apply is to ensure that the increase in photoconductivity, $\Delta I$, does not take us into the saturated beam current region, i.e., in our case $\geq 1$ μA.*



I-V CHARACTERISTIC OF SAMPLE CURRENT WITH IMPINGING ELECTRON BEAM

ELECTRON BEAM = 1 μA, -26 V
o  -168°C, IN DARK, R = 4.7 MEG.
•  -168°C, 1.77eV ILLUMINATION R = 2.85 MEG.
x  25°C, IN DARK, R = 0.91 MEG.

$\frac{I}{I_0}$

SAMPLE BIAS VOLTAGE, VOLTS
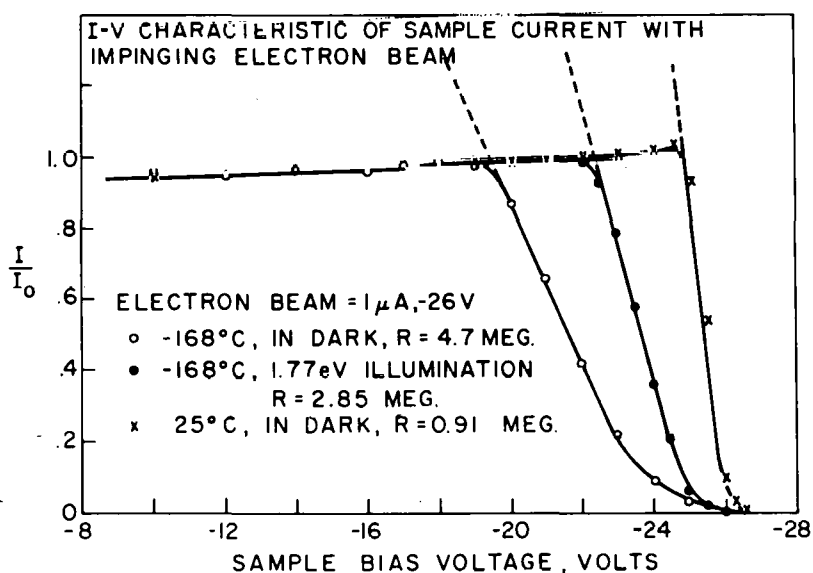
Figure 48.   Retarding beam characteristic of the Auger electron gun using a-Si:H as the target under various conditions.

---

*Another limitation we have found is that our sensitivity suffers drastically once the resistance of the film falls below about 1 MΩ.

The wavelength dependence of the photoconductivity (in arbitrary units) at -168°C measured with isophotonic flux by the technique described above is given in Fig. 49. A threshold of $\lesssim 0.4$ eV is observed, leading smoothly into a pronounced shoulder at 1.3 eV and then into a very large threshold at 1.6 eV. This is precisely the photoconductivity spectrum reported by Loveland et al. [61], using more traditional measuring techniques. We take the large onset at 1.6 eV to correspond to the optical gap and the shoulder at 1.3 eV to reflect the large increase in the gap density of states ($\gtrsim 5 \times 10^{18}/cm^3$) as reported by several workers, about 0.3-0.4 eV above the valence band [62]. As further evidence that we are indeed measuring the bulk photoconductivity, we have found that 3-eV light, which penetrates only about 0.02 μ into this material, produces an appreciably smaller photocurrent than 2-eV light which penetrates 0.5 μ.
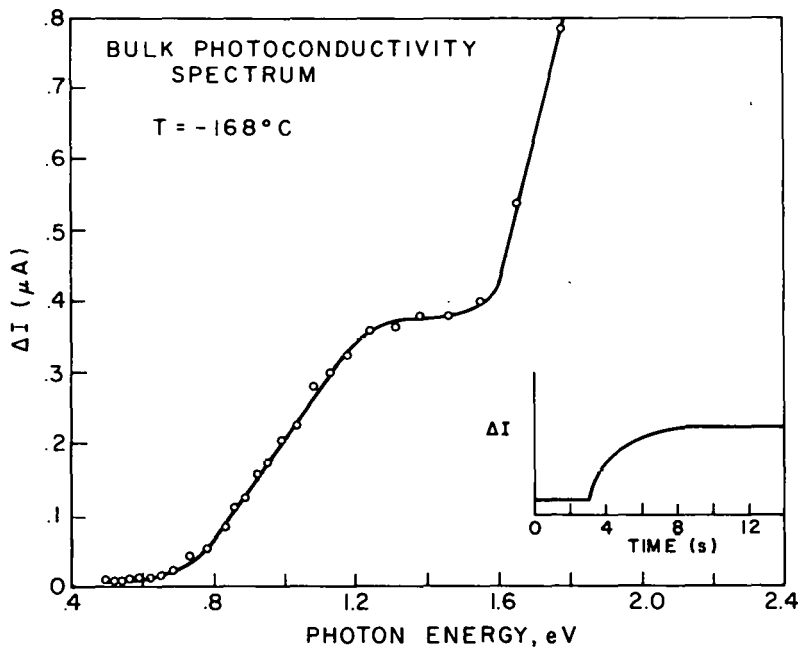


Figure 49. Bulk photoconductivity spectrum of a-Si:H at -168°C. The inset is a typical rise time of ΔI (compare to typical rise time of Δφ shown in Fig. 45).

61. R. J. Loveland et al., J. Non-Cryst. Solids 13, 55 (1973/74).
62. A. Madan and P. G. LeComber, Proc. 7th Int. Conf. Amorphous and Liquid Semiconductors, edited by W. E. Spear (CICL, University of Edinburgh, Scotland, 1977).

The intensity dependence of the photoconductivity is shown in Fig. 50 at T = -168°C. No saturation is observed. The photoconductivity decreases as (intensity)$^{1/2}$ indicating bimolecular kinetics both above and below the optical gap; this is not surprising considering the high density of gap states which serve as initial states for the photoconductive transitions.
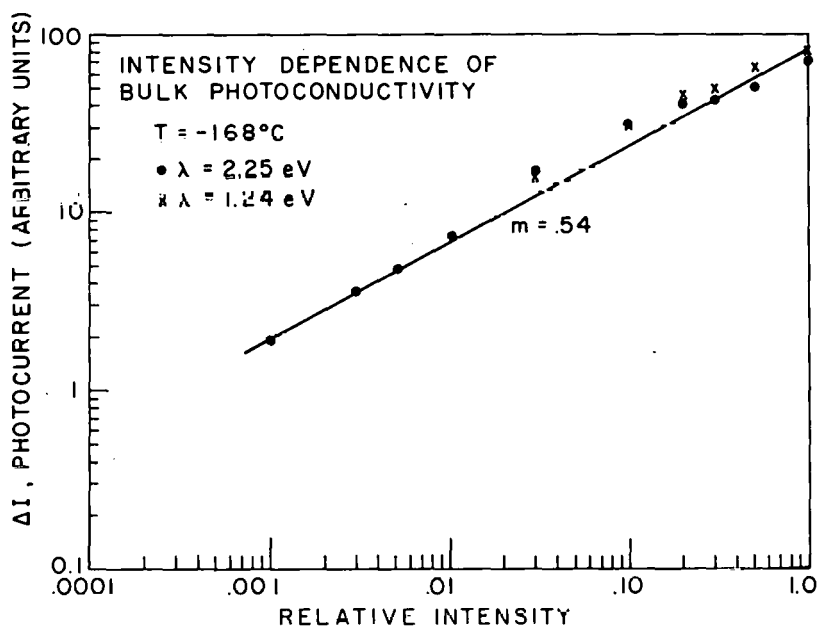


Figure 50. Intensity dependence of bulk photoconductivity. No sign of saturation is observed (compare to Fig. 46).

Returning to Fig. 50, note the inset where we have plotted a typical photo-conductivity response. This rise (and also the decay, not shown) is purely monotonic, shows no sign of the multiple electronic transitions found for the surface photovoltage, and has a rise time ∿2 s. In addition, the removal of the illumination completely restores the current to its value in the dark. Finally, the temperature dependence of the photoconductivity shows that it increases sharply with increasing temperature at all wavelengths and with no structure. We suggest that the markedly different nature of the photoconduc-tivity-short response times, different wavelength dependence, lack of multiple transition effects, and different temperature dependence, strongly indicate that the set of bulk electronic transitions which produce the photoconductivity does not determine in any material way the surface photovoltage behavior.

c. Discussion and Surface-State Energy-Level Diagram

In this section we apply the experimental results we have so far described to the construction of a surface-state energy-level diagram. Included here will be some isolated experimental results which help pinpoint some particular features of the energy-level diagram.

From the SPV measurements we have described we can list the basic low-temperature features of the surface-state energy levels as follows: they must be thermally isolated from both valence and conduction bands*. They (or a goodly fraction of them) must lie below the Fermi level; the state-emptying (optical) transition to the conduction band has a thermal step in it. Both state-filling and state-emptying transitions must be energetically possible with photons in the 0.7-0.9-eV region.

We estimate the energy of the thermal state-filling transition from the valence band in two ways, as follows: We had seen that raising the temperature from -168°C repopulates the surface states which had been previously emptied by illumination. The magnitude of this surface-state refilling can be gauged by the increase in $\Delta\phi$ observed under the conditions of curve (e), Fig. 44 [63]. The second experiment, involving state-filling from the valence band is one in which we cool the sample to -168°C, illuminate so as to empty the surface states and then warm the sample in the dark. This produces a rise in $\phi$ which we interpret as being due to the thermal refilling of the surface states. This data is shown in Fig. 51. We then estimate the thermal energy for state-filling from the leading edges of the curves in Figs. 51 and 44 plotted against reciprocal absolute temperature. This data is shown in Fig. 52 where we see good agreement between the two experiments and a state-filling thermal activation energy of about 0.2 eV.

We turn now to a discussion of the surface-state emptying transitions. We had mentioned in Section IV.I.3.a that, depending on the wavelength, some of the SPV response, $\Delta\phi$, can be separated into two components, one with a fast rise $\lesssim$1 s, and one with a much slower rise $\gtrsim$1-2 min. We attributed the slow component to the fact that this part of the transition goes through a rate-limiting thermal step, while the fast component is that part of the

*Actually, there remains a small thermal coupling between valence band and surface states which produces the small degree of restoration to the un-illuminated condition at -168°C seen in curve (a) Fig. 42.

63. R. Beyers et al., ibid.
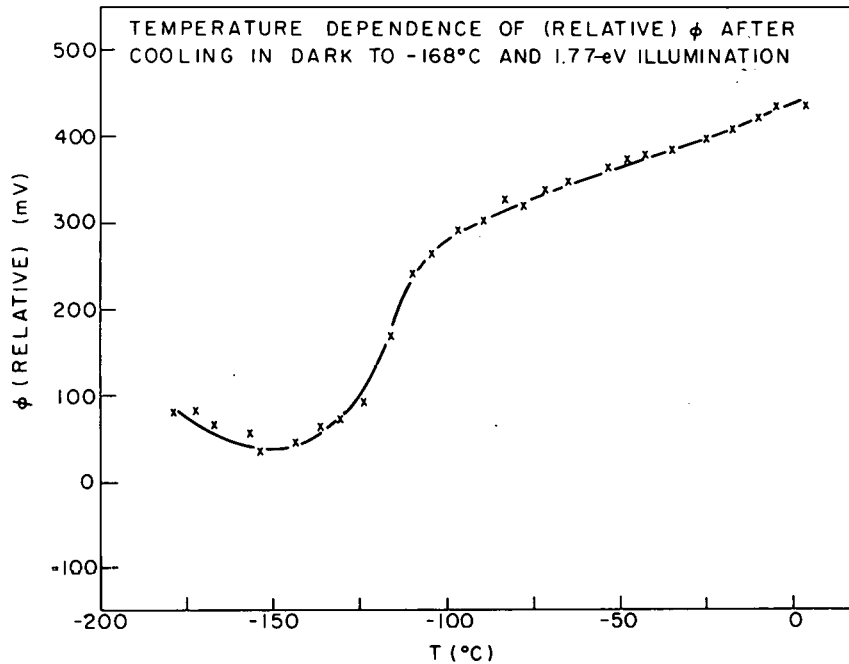
Figure 51. Change in φ with temperature after cooling to -168°C
and 1.77-eV illumination to empty surface states. The
increase in φ is thought to be caused by the thermal
refilling of the surface states.
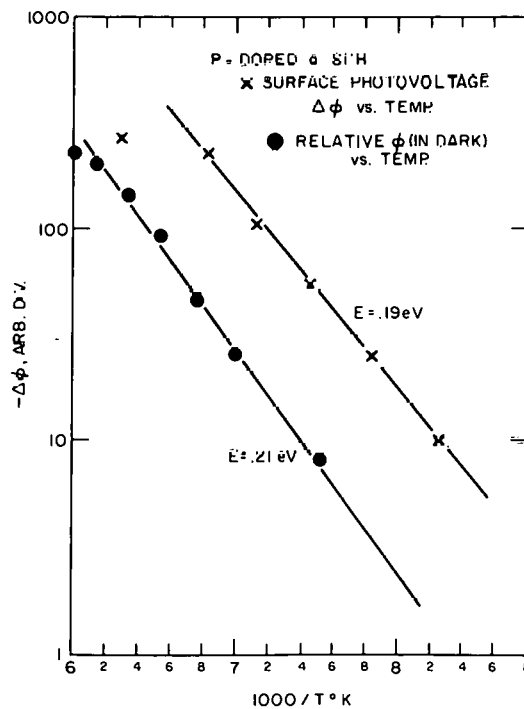


Figure 52. Reciprocal temperature curves of surface photovoltage and
relative band bending taken from data in Figs. 44 and 51.

transition that bypasses that thermal step. When the wavelength dependence of both components is plotted, Fig. 53 results. For the slow rise time, two peaks are clearly discernible, one at 0.62 eV and another smaller one at 0.95 eV. This suggests the presence of transitions between two discrete levels. The fast rise time shows only a threshold (although sharply defined) at 0.7 eV, beyond which only a sharp increase is seen. We interpret these data as follows: the wavelength peaks of the slow component at 0.95 and 0.62 eV represent the optical parts of the (optical-plus-thermal) transitions from the surface states to the conduction band: the sharp threshold of the fast component at 0.7 eV represents that energy at which the thermal step can be bypassed by optical transitions directly from the upper edge of the surface-state distribution to the bottom of the conduction band.
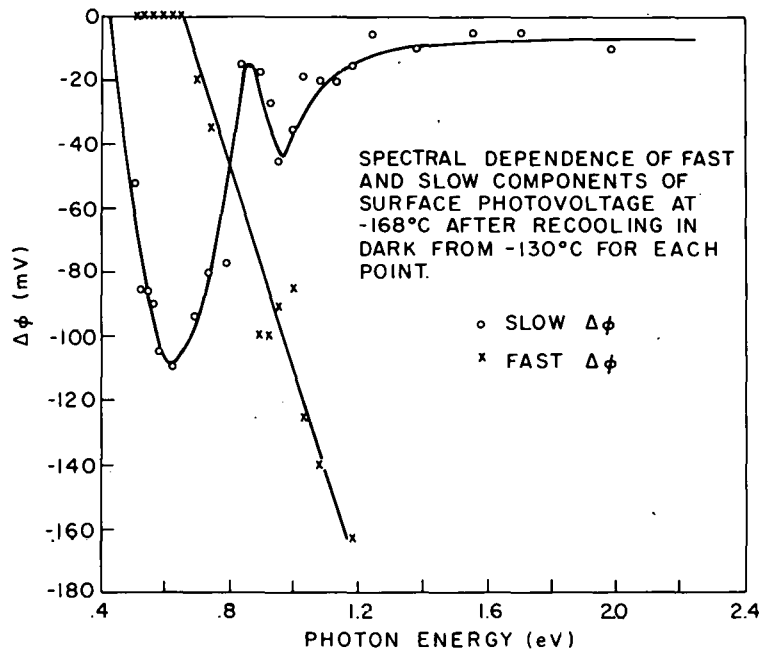


Figure 53. Wavelength dependence of the fast and slow components of $\Delta\phi$ at -168°C.

The considerations discussed above lead to the energy band scheme for the surface states shown in Fig. 54. The transitions, their energies, and their descriptions are self-explanatory. The magnitude of the band-bending is taken simply from the saturated values of $\Delta\phi$ in Fig. 46 (i.e., it is the maximum amount by which we can "unbend" the bands). The Fermi-level position

81

is taken from Beyers [22] who has measured it at different phosphorus dopings and at different temperatures. Note that it is consistent with our photo-conductivity spectrum with its threshold $\lesssim 0.4$ eV, and with the fact that our surface states can hold electrons once populated. It does not seem to be pinned by the surface states, in agreement with findings by von Roedern et al. [64].
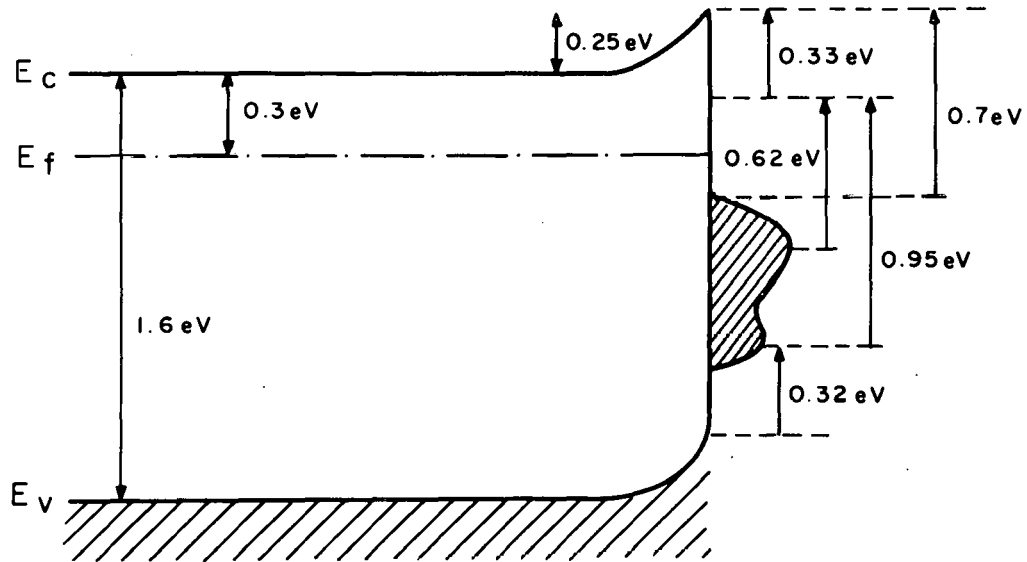


Figure 54. Energy band scheme for surface states on phosphorus-doped a-Si:H at low temperature.

We estimate the surface-state density as follows: We assume that each state is occupied by one electron, and that the total surface charge giving rise to the band-bending can be related to it by the expression:

$$V_B = \frac{Q_{SS}}{C_B} \cdot$$ (42)

where $V_B$ is the barrier height, $Q_{SS}$ is the charge residing in the surface states, and $C_B$ is the capacitance associated with the space charge region, $\chi$. $V_B$ is known, but $Q_{SS}$ is very difficult to measure directly. At -168°C, and with no direct surface contact, $C_B$ is also very difficult to measure directly*, although we were able to show that illumination does change the

---

64. B. Von Roedern et al., Solid State Commun. 29, 415 (1979).

*Attempts were made using the circuit in Fig. 47, but they were unsuccessful.

width of the depletion region. If we _assume_, however, that the depletion region is about 0.25 μm (i.e., half the thickness of the a-Si:H film), then we can estimate $N_{SS}$, the areal density of surface states, to within perhaps a factor of 2 or 3. The differential capacitance $C_d$ per unit area of a space charge region 0.25 μm wide is, in silicon, $8.6 \times 10^{-8}$ fd/cm$^2$. $C_B$ is related to $C_d$ by [65]:

$$C_B = 2C_d \qquad (43)$$

Using Eqs. (42) and (43), we can, therefore, calculate that $Q_{SS} = 2.1 \times 10^{-8}$ coulombs/cm$^2$, which corresponds to $1.3 \times 10^{11}$ electrons/cm$^2$, i.e., surface states/cm$^2$. The majority of these are considered to be distributed about an energy level approximately 0.95 eV down from the conduction band edge as shown in Fig. 54. While it is to be emphasized that this surface-state density is only an approximation to within a factor of about 2 or 3, its low value is consistent with the lack of Fermi-level pinning mentioned earlier. (It would be more correct, in considering Fermi-level pinning, to use the surface-state density per eV, in which case, another factor of two would be introduced.)

Having an estimate of $N_{SS}$ lets us also estimate a capture cross section of the surface states for photons. (We restrict ourselves here to only that wavelength where no multiple transitions are seen to occur, and at temperatures where only minimal surface-state refilling occurs during the optical emptying. This condition is λ = 1.55 eV at -168°C.) The initial slope of the Δφ response with time (i.e., $\frac{dV_B}{dt}$) when illuminated is converted to the flux of electrons leaving the surface states.

$$\frac{dn_e}{dt} = N_{SS} F \sigma \qquad (44)$$

where $n_e$ = the electron population leaving the surface states, $N_{SS}$ = the surface-state density, F = the photon flux ($2 \times 10^{15}$/cm$^2$s) and σ = the capture cross section. If we take for the photon flux F the value when the Δφ-intensity curve just breaks from saturation (see Fig. 46, top curve) we find that σ = $1 \times 10^{-15}$ cm$^2$. This is, of course, on the order of an atomic dimension and

---

65. H. K. Henisch, _Rectifying Semiconductor Contacts_ (The Clarendon Press, Oxford, England, 1957).

is consistent with our expectation of relatively high σ suggested by our saturation behavior.

d.  Changes Produced by Oxygen Adsorption

Oxidation of silicon by dry oxygen admitted into the vacuum chamber to pressures $\lesssim 10^{-3}$ Torr is very difficult and slow.  While there is some physi-sorption of oxygen as measured by Auger spectroscopy, there was no sign of any oxide-state silicon in the Auger spectrum.  This means that no Si bonds were broken and then remade with oxygen.  Only when we used the Auger electron gun to produce the well-known effect of electron-beam-enhanced oxygen adsorption, were we able to form oxides of any thickness.

When we grew 6-7 Å of oxide, as indicated by seeing only oxide-state silicon in the Auger spectrum, significantly different surface photovoltage response was observed.  The spectral dependence had a considerably higher threshold (1.2 eV compared to <0.5 eV), there were no signs of multiple sur-face electron transitions, and the magnitude of the overall surface photo-voltages was considerably smaller.  We interpret these results of mean (in part) that we are dealing with a considerably smaller density of surface states, and/or Si-SiO$_2$ interface states, on oxidized a-Si.  We suggest that this might be due simply to the electronegative oxygen removing dangling-electron surface states from the silicon.

4.  Intrinsic a-Si:H

a.  Surface Photovoltage and Bulk Photoconductivity Measurements

While P-doped a-Si:H has surface photovoltage signals only at low temper-ature, intrinsic a-Si:H has strong signals not only at low temperature but at room temperature as well.  Contrary to the behavior at low temperature where, at sub-bandgap illumination, there is no return to the dark condition, there is at room temperature complete and fast ($\lesssim$.25 s) return to the dark condition when the light is removed.  This means that even though light can produce a change in the equilibrium electron population of surface states, there is sufficient coupling between these states and the bulk bands so that after light has partially emptied them they can readily refill when the light is removed.

Figure 55 shows the spectral dependence of the SPV at room temperature for different surface conditons: (a) sputter-cleaned only, (b) sputter-cleaned and annealed at 250-300°C, and (c) with the one monolayer of O$_2$ adsorbed on

the surface. All signals were of the polarity which indicated that illumination empties surface states and flattens bands which had been bent upward by a negative surface charge.
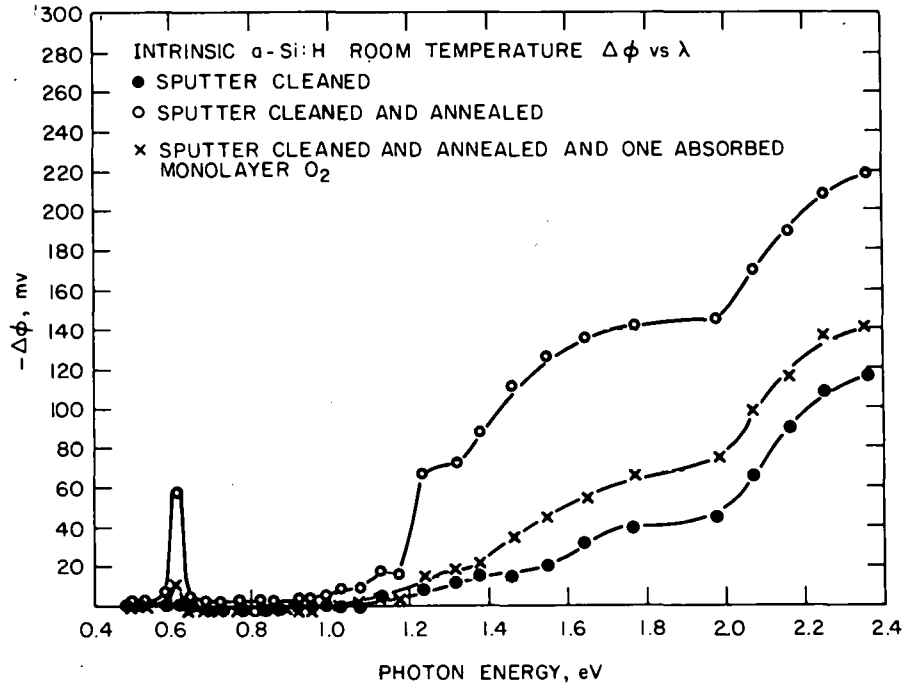


Figure 55. Spectral dependence of surface photovoltage at room temperature of intrinsic a-Si:H with different surface treatments.

Two noteworthy features are, first, that the spectrum is strongly affected by sputtering and oxygen adsorption, thus indicating directly that the states involved in the SPV (i.e., band-bending) are surface states, and, second, that there is an extremely well-defined peak at 0.62 eV that was not observed for P-doped material. At energies higher than 0.62 eV, there is first some small structure and then two broad shoulders beginning at about 1.3 and 2.0 eV, respectively. There is no sharp feature at the bandgap energy 1.6 eV.

At liquid nitrogen temperature, the SPV produced by illumination does not disappear when the illumination is removed. This is due to the strong isolation of the bandgap surface states from the valence band; i.e., there is no refilling of the surface states once emptied. Accordingly, in order to get a true spectral dependence of the SPV at liquid nitrogen temperature, we heated the sample to some intermediate temperature sufficient to refill the states

(-85°C) prior to recooling for each wavelength point, just as we did for P-doped material as discussed earlier. The spectral data so obtained is shown in Fig. 56. The data are similar to those found in Fig. 21, except that now the 0.62-eV response is larger compared to the rest of the spectrum, and the broad shoulders observed at room temperature have now been better resolved into broad peaks. Oxygen is seen to have similar effects at low temperature to those at room temperature.
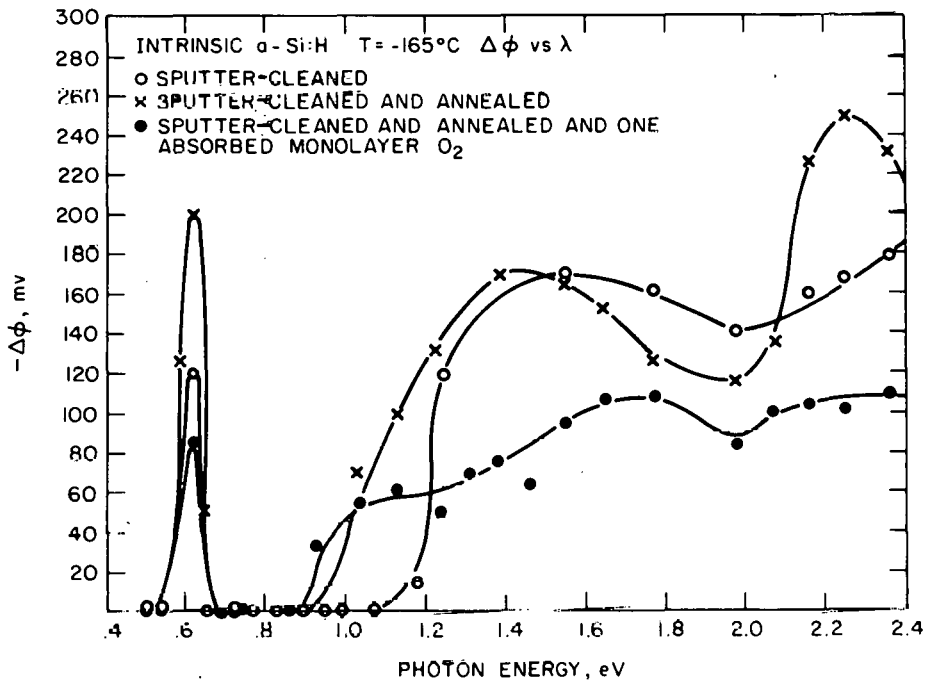


Figure 56. Spectral dependence of surface photovoltage at -165°C for intrinsic a-Si:H with different surface treatments. Note localized discrete transition at 0.62 eV in Figs. 45 and 46.

In order to verify that the electronic transitions which produce the band-bending changes $\Delta\phi$ directly involve primarily electron surface states and not electron bulk states, parallel measurements were made of the bulk photoconductivity employing the use of the Auger electron-gun beam as one electrode (see Figs. 47 and 48). The photoconductivity results are shown in Fig. 57 with the SPV spectrum included for comparison dashed curves. Note that the absence of photocurrent where strong SPV signals are seen, the strong feature in the photoconductivity at bandgap, the different rise and decay times, and

75
70 — INTRINSIC a:SiH        ● SPUTTER-CLEANED
      T= -165°C  ΔI vs λ       AND ANNEALED
65
      ○ SPUTTER-CLEANED
60       AND ANNEALED AND
         ONE ABSORBED
55 — — — Δφ vs λ       MONOLAYER $O_2$
50
45   BAND-BENDING SPECTRUM
       ← RISE TIMES
40   ~ I min
35
30
25                           ← PHOTOCURRENT
                               SPECTRUM
20                             RISE TIMES
                               ~ I sec
15
10
5

0.4  0.6  0.8  1.0  1.2  1.4  1.6  1.8  2.0  2.2  2.4

ΔI, PHOTOCURRENT - ARB. DIV.

PHOTON ENERGY, eV
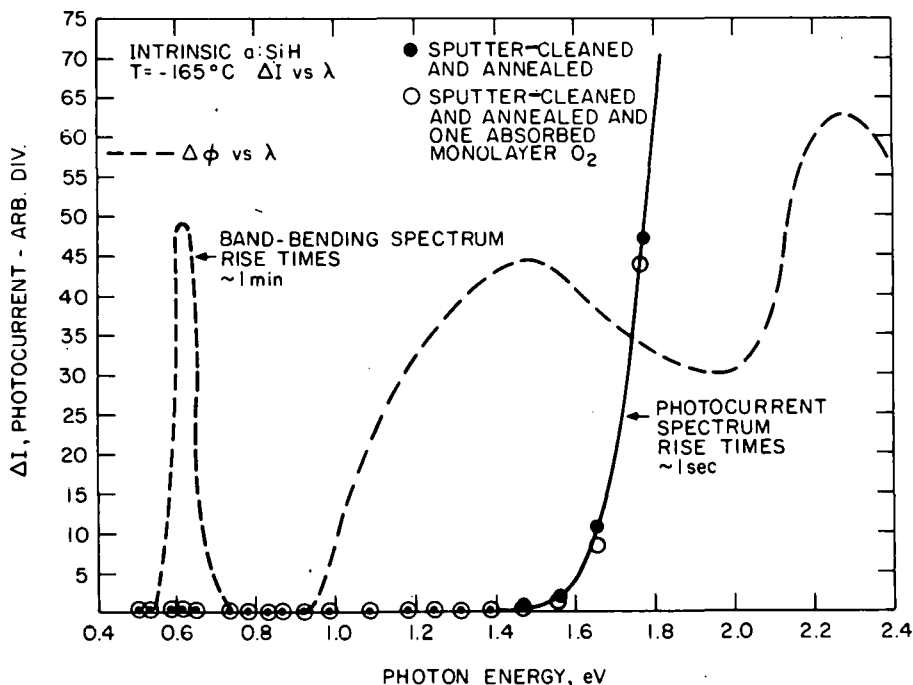
Figure 57.   Photoconductivity spectrum at -165°C of intrinsic a-Si:H.
Note absence of strong 1.3-eV shoulder seen for P-doped
material in Fig. 49.   Surface photovoltage spectrum (dashed
line for comparison).

the lack of significant change with surface treatment, all indicate that the
bulk photoconductivity transitions are not those which are producing the
changes in band-bending.   Further attention is called to the absence of the
marked photoconductivity shoulder at 1.3 eV seen in Fig. 49 (and also by
other workers) for P-doped material.

The intensity dependence of Δφ for intrinsic material (not shown) in-
dicates even stronger saturation than that for P-doped material, in that it
extends through even lower intensities than for P-doped material; see Fig. 46.
In the discussion, we will relate this to the lower overall band-bending ob-
served for intrinsic material.   As was done for P-doped material, we have
estimated the thermal energy required to refill emptied surface states by
two methods.   In both, we start at liquid nitrogen temperature with all
surface states emptied by illumination.   There is now no band-bending.   In
the first method, we heat the sample in the dark and measure the increase
in band-bending due to the thermal refilling or surface states.   In the
second, we measure the onset and subsequent increase in SPV as the temper-
ature increases which SPV occurs because of the refilled surface states.
Figures 58 and 59 show the results of these experiments.   Both figures
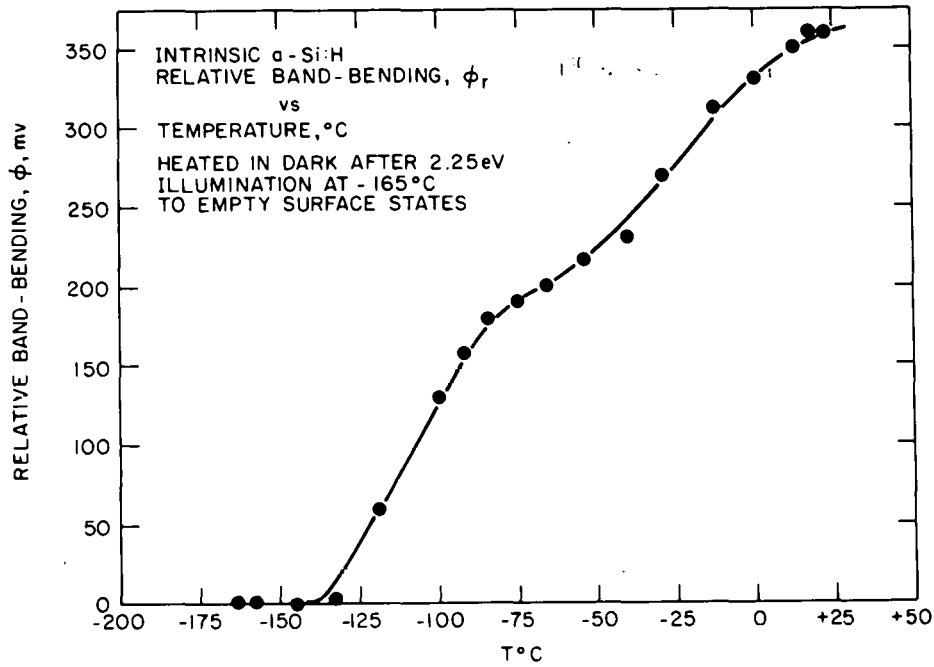
Figure 58. Temperature dependence of relative band-bending in the dark after surface states have been emptied at -168°C. Intrinsic a-Si:H.
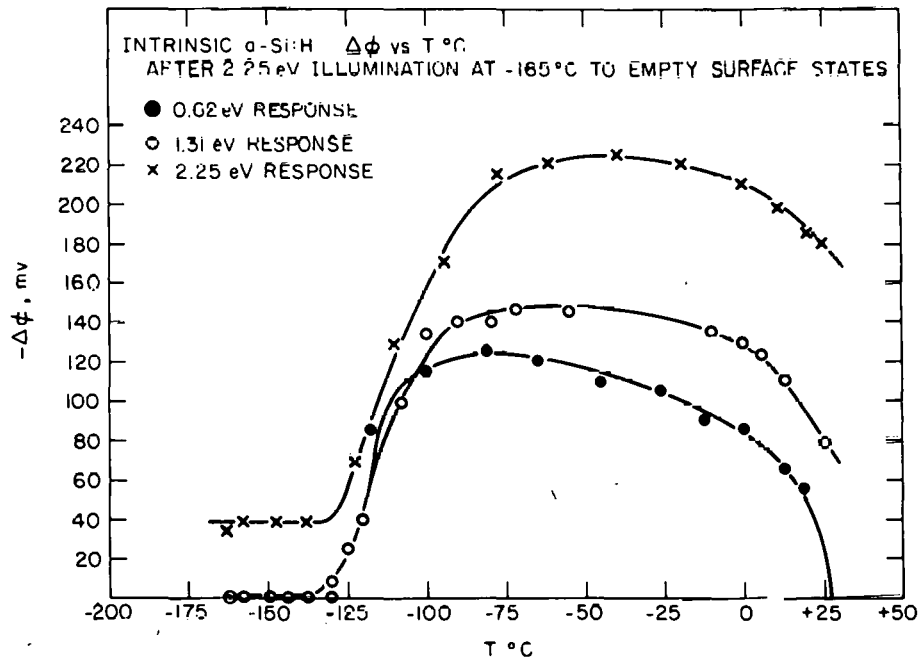


Figure 59. Temperature dependence of surface photovoltage after surface states have been emptied at -168°C. Intrinsic a-Si:H.

show similar behavior as for P-doped material and when the leading edges
of these curves are plotted vs reciprocal temperature, an activation energy
of about 0.2 eV results.

b.  Discussion and Surface-State Energy-Level Diagram

We have not yet evolved a consistent picture of the surface-state dis-
tribution and its properties that will explain all aspects of our experimental
data.  Experiments are still under way in an attempt to clarify the situation.
In this section we will discuss the surface of intrinsic a-Si:H, indicating
what we know, and also some of the remaining questions.

Essentially, we are dealing with a distribution of filled surface states
which lie below the Fermi level and are, to some degree, thermally isolated
from the valence band-in broad outline similar to the situation for P-doped
material.  But there are some differences.  The very sharp 0.62-eV transition
in Figs. 55 and 56 indicates a localized transition between two discrete
states in the bandgap.  The presence of a room-temperature SPV indicates a
greater degree of thermal isolation between the bottom of the surface-state
distribution and the valence band than was found for P-doped material.  The
resolved peak in the SPV spectrum at 2.25 eV, its much faster rise time
($\sim$0.25 s) than that at 0.62 eV or 1.45 eV, and the fact that this fast re-
sponse returns to its dark value at -168°C suggest that the 2.25-eV response
be due to a transition from levels below the top of the valence band at the
surface directly to the conduction band.  Such levels would have strong
coupling to the valence band even at low temperature.  Finally, the overall
maximum saturated band-bending we observe in intrinsic material is lower
($\sim$0.15 eV) than that found for P-doped material ($\sim$.25 eV).  An energy level
model of the surface at low temperature is shown schematically in Fig. 60,
and is constructed as follows: the Fermi level is derived from the tempera-
ture dependence of the dark conductivity above room temperature.  Next,
for the placement of the discrete 0.62-eV transition, we require an estimate
of its thermal activation step to the conduction band.  We have obtained
this from the temperature dependence of the initial slope $\frac{d}{dt}$ (-$\Delta\phi$) t = 0 of
the rise-time curves, since the initial part of the curve is given by a
single exponential factor e-$\alpha$t, in which case the initial slope is propor-
tional to $\alpha$.  When these slopes are plotted vs reciprocal absolute temper-
ature, a straight line results whose slope indicates a thermal activation
energy of 0.11 eV (see Fig. 61); thus, we can locate the 0.62-eV transition
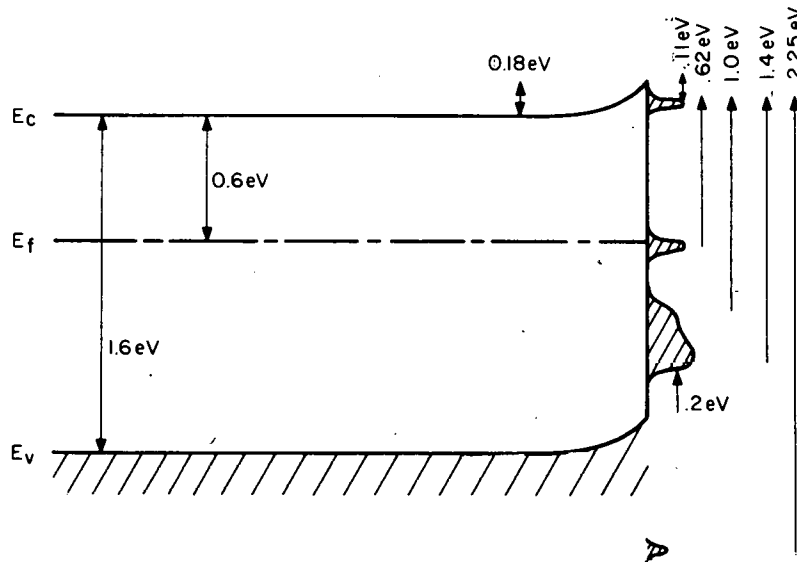
Figure 60. Energy level scheme for surface states on intrinsic
a-Si:H at -165°C.
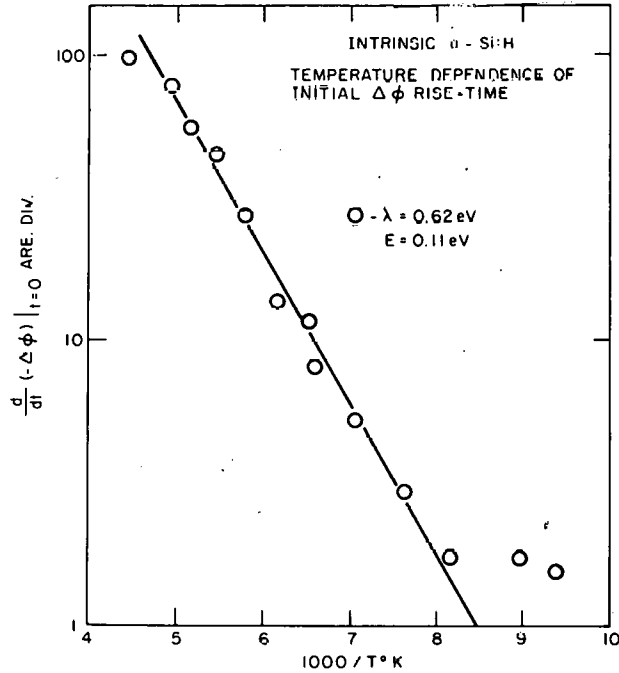


Figure 61. Reciprocal temperature plot of initial rise time of 0.62-eV
surface photovoltage signal. Activation energy is associated
with the thermal step of the 0.62-eV transition.

and its thermal step as shown in Fig. 60. Note that the initial state of the 0.62-eV transition lies just below the Fermi level.

Figure 56 indicates next that below the initial state of the 0.62-eV transition lies a distribution of states with a threshold at about 1.0 eV. This distribution of states is isolated from the valence band as indicated by the fact that it does not refill at low temperature after emptying. We associate the thermal energy required for this refilling with the energy separation between the bottom of the surface-state distribution and the valence band. Both Figs. 58 and 59 indicate from the rise of $\Delta\phi$ with temperature that the states have refilled by about -85°C. When the leading edge of this rise is plotted vs reciprocal absolute temperature, it indicates an energy of about 0.2 eV (similar to that for P-doped material when analyzed in this manner). Thus, we can locate this distribution of surface states as shown in Fig. 60.

The major differences between the energy level scheme shown in Fig. 60 and the corresponding scheme for P-doped material (Fig. 54) can be accounted for by the fact that the P-doped material has more surface states within the bandgap than intrinsic material (as has been well established for bulk states in the bandgap). Specifically, this can account for: (a) the larger SPV (i.e., band-bending) at low temperature for P-doped material, (b) the better-resolved wavelength dependence of the SPV for the intrinsic material, including the sharply defined, discrete transition at 0.62 eV, (c) less thermal isolation between valence band and the surface state distribution for P-doped material (even though similar thermal energies are indicated), (d) saturation of the SPV signal extending to lower intensities for the intrinsic material. Finally, it is to be noted that while the inclusion of P as a dopant might itself introduce more (extrinsic) surface states in the bandgap, note that the lower Fermi level of the higher resistivity intrinsic material would also contribute to a smaller number of filled surface states. As estimation of the surface-state density for the intrinsic material cannot be as readily attempted as for P-doped material. The much higher resistivity of intrinsic material might mean a larger depletion region and smaller barrier capacitance; on the other hand, a smaller surface barrier (band-bending) would ordinarily mean a smaller depletion region and larger barrier capacitance. We simply have no independent experimental data on depletion layers in intrinsic material. All we can really say is that since $V_s$, the surface barrier is smaller, and

$C_s$, the surface barrier capacitance is <u>likely</u> to be smaller, $Q_s$ (the surface charge) $= C_s V_s$ is also likely to be smaller, and we associate this smaller surface charge with a smaller surface-state density for intrinsic material.

The most fundamental questions we cannot yet explain satisfactorily are how (why) empty 0.62-eV levels refill at the same temperature at which the lower-lying distribution of levels fill, as indicated in Figs. 58 and 59; and and why, if 1.3-eV photons empty 0.62-eV levels (as they are found to do) <u>in addition to</u> levels at 1.3 eV, isn't $\Delta\phi$ at 1.3 eV significantly greater than $\Delta\phi$ at 0.62 eV. There may be some connection between the 0.62-eV levels and the lower-lying distribution of levels that we do not yet understand. Further work will continue along these lines.

5.  Dehydrogenation Experiments

Dehydrogenation for both P-doped and intrinsic material was accomplished by heating at 550°C for 30 min. Earlier experiments had indicated that this removed $\gtrsim$99% of the hydrogen.

For P-doped material, no photoconductivity was seen at any wavelength at any temperature after dehydrogenation. This was not very surprising after we found that the film resistance (at -168°C) had changed from $4.7 \times 10^6$ (hydrogenated) to $0.07 \times 10^6$ (dehydrogenated). The decrease in resistivity is presumably due to the large increase in bandgap states accompanying the dehydrogenation.

No surface photovoltage was seen under any conditions at any temperature, and this <u>was</u> somewhat surprising. This might mean that the density of surface states has decreased sharply due to the dehydrogenation; however, we consider this unlikely. We think a more likely possibility is that the dehydrogenation has increased the bandgap states density so much that, especially near the valence band, it has removed the electronic isolation between surface states and valence or conduction bands required for the observation of a surface photovoltage.

For intrinsic material, dehydrogenation resulted in a radically different surface-state situation. At room temperature there was no surface photovoltage. However, at -168°C there were strong photovoltage signals, but they were all of a polarity which indicated upward band-bending; i.e., surface-state filling transitions. The wavelength dependence of this upward band-bending was entirely different from that for the band-flattening observed for hydrogenous

material. Furthermore, for the dehydrogenated material, the wavelength dependence of the surface photovoltage and of the bulk photoconductivity are the same as shown in Fig. 62, suggesting that now bulk transitions are producing the changes in surface band-bending. The suggested mechanism for this is, therefore, electron excitation from bulk states below the Fermi level to the conduction band, and then over the surface barrier to fill empty surface states. The now-empty surface states could be due to unsaturated bonds at the surface, now that hydrogen has been removed.
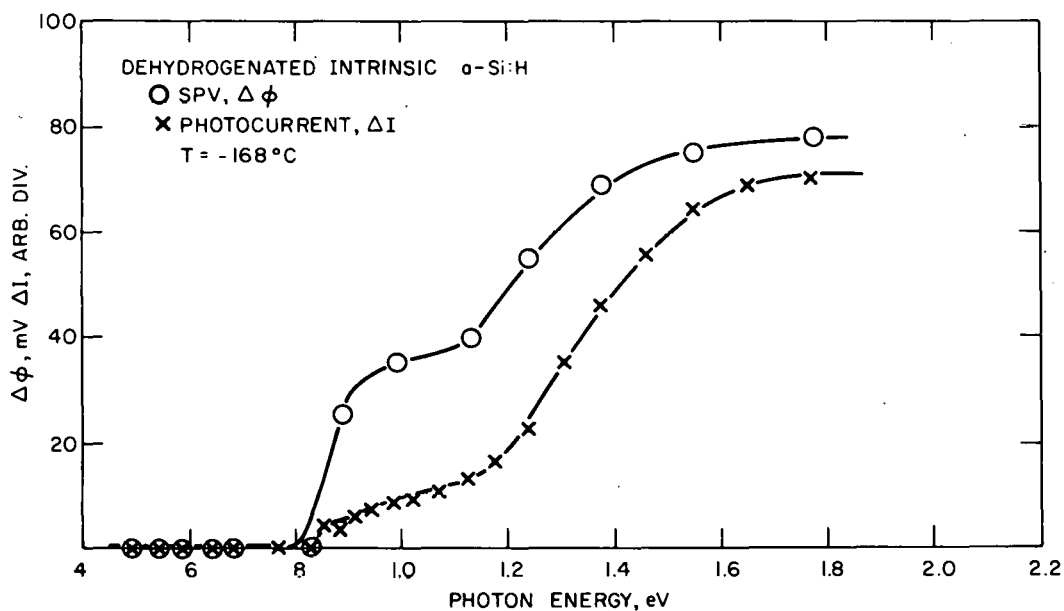


Figure 62. Spectral dependence of surface photovoltage and bulk photo-conductivity for dehydrogenated intrinsic a-Si:H. Note strong similarity of spectra.

SECTION V

FORMATION OF SOLAR-CELL STRUCTURES

A.  STACKED a-Si:H SOLAR CELLS

1.  Introduction

Recently, there has been a revival of interest in multiple-junction (stacked) solar cells, because this concept holds promise of high efficiencies [66].  The idea behind the stacked cells is one of matching different ranges of the solar spectrum to the bandgaps of the cells [67].  Ideally, a monolithic stack of cells is desired; however, with single crystal cells, problems with epitaxy arise.  Stacked cells consisting of single-crystal homojunctions and heterojunctions have been proposed [66,68-70].  A two-cell stack based on AlGaAs/GaAs materials system has been fabricated, thus far yielding efficiency of 9% [71].

Hydrogenated amorphous silicon (a-Si:H) solar cells have been reported with efficiencies of up to 5.5% [13].  We have considered the concept of stacked cells as a means of increasing the efficiency of the a-Si:H cells and arrived at some interesting possibilities.  The first of these is that a-Si:H occurs with a range of bandgaps from about 1.5 to 1.8 eV, depending on the hydrogen content [72].  Hence, there is a possibility of bandgap matching over a limited range.  The next possibility arises from the observation [73] that a-Si:H cells show maximum efficiency at a thickness of

66.  For recent references on the subject of stacked cells see R. L. Moon, L. W. James, H. A. Van der Plas, T. O. Yep, G. A. Antypas, and Y. Chai, Conf. Record 13th IEEE Photovoltaic Spec. Conf., IEEE, New York, p. 859, 1978.
67.  E. D. Jackson, Trans. Conf. on the Use of Solar Energy, Tuscon, Arizona, 1955, (U. of Arizona Press, Tuscon, 1958) Vol. 5, p. 122.
68.  M. F. Lamorte and D. Abbot, Ref. 66, p. 874.
69.  L. M. Fraas and R. C. Knechtli, Ref. 66, p. 886.
70.  M. Arienzo and J. J. Loferski, Ref. 66, p. 898.
71.  S. M. Bedair and M. F. Lamorte, Appl. Phys. Lett. $\underline{34}$ (1), 38 (1979).
72.  J. J. Hanak, P. J. Zanzucchi, D. E. Carlson, C. R. Wronski, and J. I. Pankove, Proc. 7th Intern. Vac. Congr. and 3rd Intern. Conf. Solid Surfaces, edited by R. Dobrozemski, et al., (F. Berger and Sohne, Horn, Austria, 1977) p. 1947.
73.  J. J. Hanak, V. Korsun, and J. P. Pellicane, 1979 Photovoltaic Solar Energy Conf., Berlin (West), Germany.

about 500 nm because of low depletion width. At this thickness much of the useful light is not absorbed. Hence, several thin cells having appropriate thicknesses and combined in a stacked cell should result in a more efficient use of the incident light.

Finally, because of low hole diffusion length and depletion width there is an increased chance of recombination with thickness; hence, higher quantum efficiency would be expected in thin cells. This observation also gives support to the idea of stacked a-Si:H cells.

Marfaing [74] recently proposed stacked cells based on solid solutions of a-Si:H and a-Ge:H materials, which have optical bandgap shifting linearly with composition from 1.65 to 0.95, respectively [75]. This system would permit bandgap matching over a wider range. Undoubtedly, a stacked cell incorporating all of the preceding possibilities would result in optimum efficiency.

The question arises regarding the ohmic connection between each active junction. In the case of single-crystal materials n+p+ tunnel junctions have been proposed and used with some success [71]. For the a-Si:H, a-Ge:H stacked cell, n+p+ tunnel junctions have also been proposed [74]. However, because of the fact that a-Si:H cannot be doped to sufficiently high conductivities and that the n+p+ junction constitutes a solar cell, although inefficient [73], we anticipated that this type of tunnel junction might cause a decrease in the expected $V_{oc}$ of the stacked cell. However, because of the lack of constraint of epitaxy, several other cell interconnections can be envisioned for a-Si:H stacked cells.

In this initial experimental study, stacked cells have been fabricated of a-Si:H material having the same optical bandgap throughout the cell structure. This was done to simplify the demonstration of the concept and to serve as a vehicle for comparison of different cell interconnections.

2. Experimental Results and Discussion

The type of solar cells used in this work for fabricating a stacked cell was an inverted p+in+ a-Si:H cell described previously [73]. The stacked

74. Y. Marfaing, ibid.
75. A. Onton, H. Wieder, J. Chevallier, and C. R. Guarnieri, Proc. 7th Intern. Conf. Amorphous and Liquid Semicond., W. E. Spear, edited by G. G. Stevenson (CICL, University of Edinburgh, Scotland, 1977).

cells that were fabricated consisted of two cells having a structure shown in Fig. 63. The thicknesses of the i layers were designed to yield approximately the same current. The estimates of the appropriate thicknesses were obtained graphically as follows. The expected $J_{sc}$'s of the first and second cells of a two-cell stack as a function of the thickness of the i layer of the first cell were plotted in Fig. 64. The $J_{sc}$ data for the first cell were taken from Ref. 73; the $J_{sc}$ first increases with thickness and then saturates at 500 nm. The data for the second cell were obtained by passing simulated AM1 sunlight through an a-Si:H film filter having a graded thickness from 0 to 600 nm and measuring the $J_{sc}$ generated by the transmitted light by means of an a-Si:H solar cell. This second cell had the i-layer thickness of 500 nm and $J_{sc}$ in AM1 light of about 7 mA/cm$^2$. The $J_{sc}$ decreases because of the increasing absorption of the light by the i layer of the first cell, simulated by the filter. The $J_{sc}$ data have been corrected for the absorption of the glass substrate and of 20-nm-thick p+ and of 20-nm thick n+ a-Si:H layers intended to be used in the first cell. In Fig. 64 the $J_{sc}$ of the stacked cell would follow the curve of the first cell before the intersection and the curve of the second cell after the intersection. The highest $J_{sc}$ occurs at the intersection where the $J_{sc}$'s for both cells are equal. Hence the designed thickness of the i layer of the first cell was about 82 nm.

STACKED a-Si:H SOLAR CELL
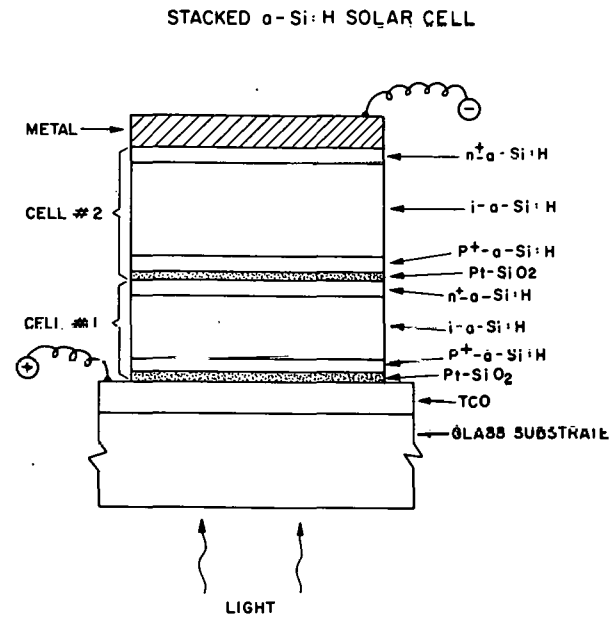


Figure 63. Schematic diagram of a cross section of a stacked cell consisting of two p+in+ a-Si:H cells and having a n+/Pt-SiO$_2$/p+ tunnel junction.
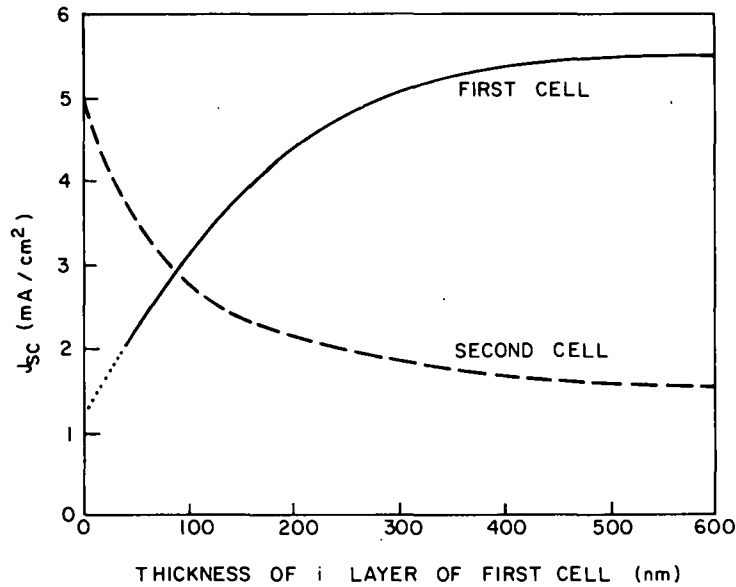
Figure 64.  Expected $J_{sc}$ of the first and second cells of a stacked
cell as a function of the i-layer thickness of the first
cell.

Three different tunnel junctions have been tried,. including (a) n+p+
a-Si:H (the back side of the first p+in+ cell and the front side of the
second cell), (b) Pt-SiO$_2$ cermet about 10 nm thick and containing 10 to 15
vol % Pt, between the n+ and the p+ layers, and (c) thin Ti layer, 3 to 5 nm
thick, between the n+ and the cermet layers of junction b.

The corresponding I-V curves taken under simulated AM1 sun illumination
are shown in Fig. 65a to 65c, respectively.  The first two curves show a
second hump in the forward-bias region above $V_{oc}$ due to the fact that the
tunnel junctions a and b contain a barrier.  The IV curve obtained with
tunnel junction c shows a relatively normal behavior.  The solar-cell per-
formance parameters of the three cells are shown in Table 7, wich shows, in
addition, the data for the front, single cell used in stack c.  The $V_{oc}$ of
the stacked cell c is slightly more than twice that of the single cell,
whereas the $V_{oc}$ of stacked cells a and b show substantially lower values.
Device a, having the n+p+ tunnel junction is the worst of the three, showing
the expected depression of $V_{oc}$ in excess of 0.6 V.

The cell structure just described allows for the fabrication of stacked
cells having more than two active junctions.  A three-cell stack, having
junctions of the type c (of Table 7), had $V_{oc}$ of 1.92 V, $J_{sc}$ of 2.61 mA/cm$^2$,
FF of 0.50 and η of 2.5%.  A large (35 cm$^2$) stacked cell consisting of three

97
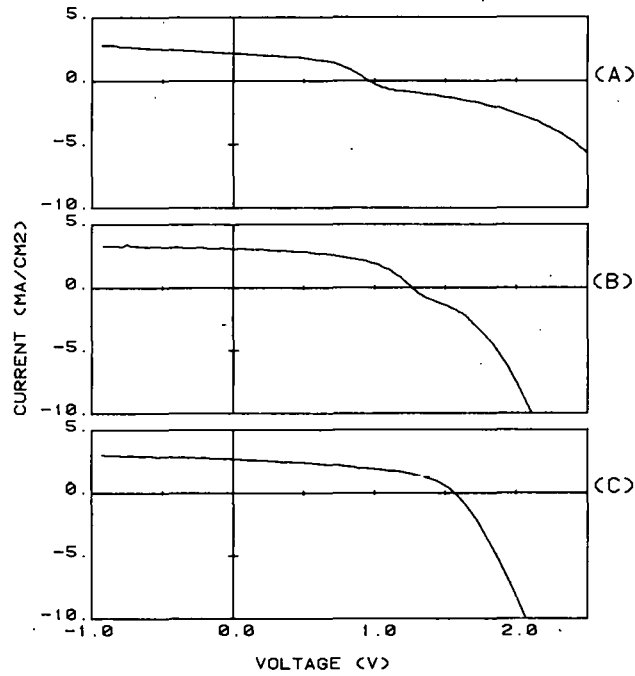
Figure 65.   I-V curves of 2-cell stacked cells using three different
tunnel junctions listed in Table 7.

TABLE 7.   PERFORMANCE OF a-Si:H STACKED CELLS
HAVING DIFFERENT INTERCONNECTIONS

| Sample | Interconnection | $V_{oc}$ (V) | $J_{sc}$ (mA/cm$^2$) | FF | Eff. (%) |
|---|---|---|---|---|---|
| a(2-cell stack) | n+p+ | 0.96 | 2.15 | 0.50 | 1.02 |
| b(2-cell stack) | n+/Pt-SiO$_2$/p+ | 1.26 | 3.09 | 0.51 | 1.99 |
| c(2-cell stack) | n+/Ti/Pt-SiO$_2$/p+ | 1.57 | 2.67 | 0.47 | 1.98 |
| c(front cell) | - | 0.76 | 2.83 | 0.55 | 1.18 |

cells has been made in which the n+/Pt-SiO$_2$/p+ tunnel junctions were used.
Its performance is shown in Fig. 66, showing $V_{oc}$ of 1.75 V.  Thus, far, none
of the stacked cells have exceeded the efficiency of a single p+in+ cell (3.2%)
made in the same apparatus.  A part of the problem is due to the additional
light losses introduced with the added layers.  Another problem is that the
thicknesses of all of the layers have not been optimized.

B.   MATERIALS STUDIES FOR p-i-n a-Si:H SOLAR CELLS

1.   Introduction

    In a previous Final Report [31] we described an automated method of syn-
thesis and testing of solar-cell materials and structures.  This method is
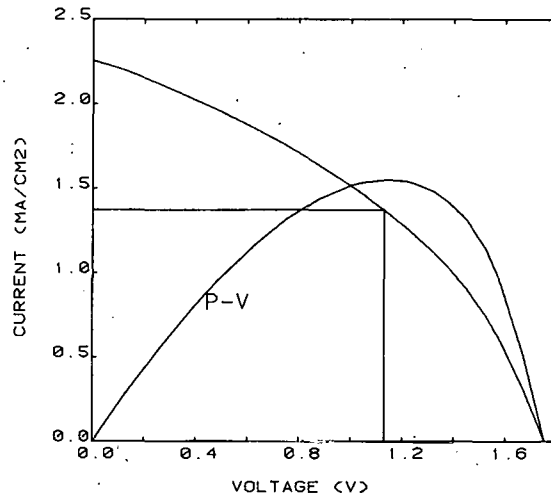
V-OC       J-SC     F.F.      EFF.
1.750      2.25     0.39      1.55%

1/SLOPE @V-OC(OHM/CM2/CELL)
301.1

Figure 66.  I-V curve of a 3-cell stacked cell (active area: 35 cm$^2$) on a molybdenum substrate.

based on the use of planar smaples which have graded parameters in one or two directions along the plane.  The use of this technique leads to a substantial acceleration of the optimization of the materials for a-Si:H solar cells.  We have used this technique in the optimization of some of the materials' parameters in the cell structure consisting of glass substrate/ ITO/Pt-SiO$_2$ front cermet/p+in¹ a-Si:H/metal.  Thus far, the most obvious parameters have been chosen, including the thicknesses of all the layers, the composition of the cermet and the substrate temperature used during the deposition of the a-Si:H layers.  The results of these stuides [73] will follow below.  Also included are more recent results on the dependence of solar-cell performance on rf power used for the gas discharge for the deposition of a-Si:H.

2.  Experimental Methods

The samples consisted of a plate of float-glass substrate, 7.6x7.6 cm$^2$ in area, having a continuous ground electrode of indium-tin-oxide(ITO)*, a

---

*Most of the substrates have been supplied by Triplex, England; sheet resistivity 10 ohm/□; ITO thickness 2000-3000 Å; optical transmission 85%.  Thinner ITO samples were sputtered in-house.

continous multilayer solar-cell structure and a matrix of 25x25 square metallic film electrodes $2.5 \times 10^{-2}$ cm$^2$ in area, and on 0.25-cm centers. The variables of interest are graded along the X- or X- and Y-directions.

The deposition of the films has been done in a diode radio-frequency (rf) sputtering system equipped with a disk target 14.6 cm in diameter and a heated, grounded graphite substrate holder, 4 to 6 cm distant from the target.

The a-Si:H layers have been deposited by the decomposition of silane by the rf capacitive glow discharge technique [76]. Pure SiH$_4$ was used except in the case of doped films, in which case 1% mixtures of PH$_3$ or B$_2$H$_6$ in hydrogen were used to form a 0.1% mixture of a dopant in SiH$_4$. Except where they were selected as a variable, other conditions were kept constant as follows: SiH$_4$ flow = 20 SCCM, total pressure = 20 mTorr, substrate temperature = 330°C, and rf power = 0.5 W/cm$^2$. The deposition rate of a-Si:H was about 900 Å/min.

The cermet and metal films were deposited by rf co-sputtering and sputtering, respectively. For the cermet layers a composite target of a SiO$_2$ disk overlayed with one or more rectangular metal strips was used. Either graded or constant composition films were deposited. Their composition was determined by methods described earlier [77].

Films having graded thickness were obtained by slowly opening or closing a planar, motor-driven shutter covering the substrate as the film was deposited. Graded substrate temperature was obtained by using a graphite substrate holder heated on one end and cooled on the other.

Samples shown in Fig. 67. were mounted in an apparatus capable of scanning along the X- and Y-directions, contacting any cell, applying light (simulated AM1 sun) and measuring the current-voltage (I-V) characteristics between -1 and +1 V. The control of the measuring equipment and the subsequent calculations were performed by a programmable desk-top calculator. The I-V curves were analyzed for the open-circuit voltage ($V_{oc}$), the short-circuit current density ($J_{sc}$), the fill factor (FF), the cell efficiency ($\eta$), and effective series resistance at $V_{oc}$($R_a$). The approximate time to test and evaluate a single cell was 70 s.

---

76. J. C. Knights, Philos, Mag. <u>34</u>, 663 (1976).
77. J. J. Hanak, H. W. Lehmann, and R. K. Wehner, J. Appl. Phys. <u>43</u>, (4), 1666 (1972); J. J. Hanak and B. F. T. Bolker, J. Appl. Phys. <u>44</u>, (11), 5142, (1973).
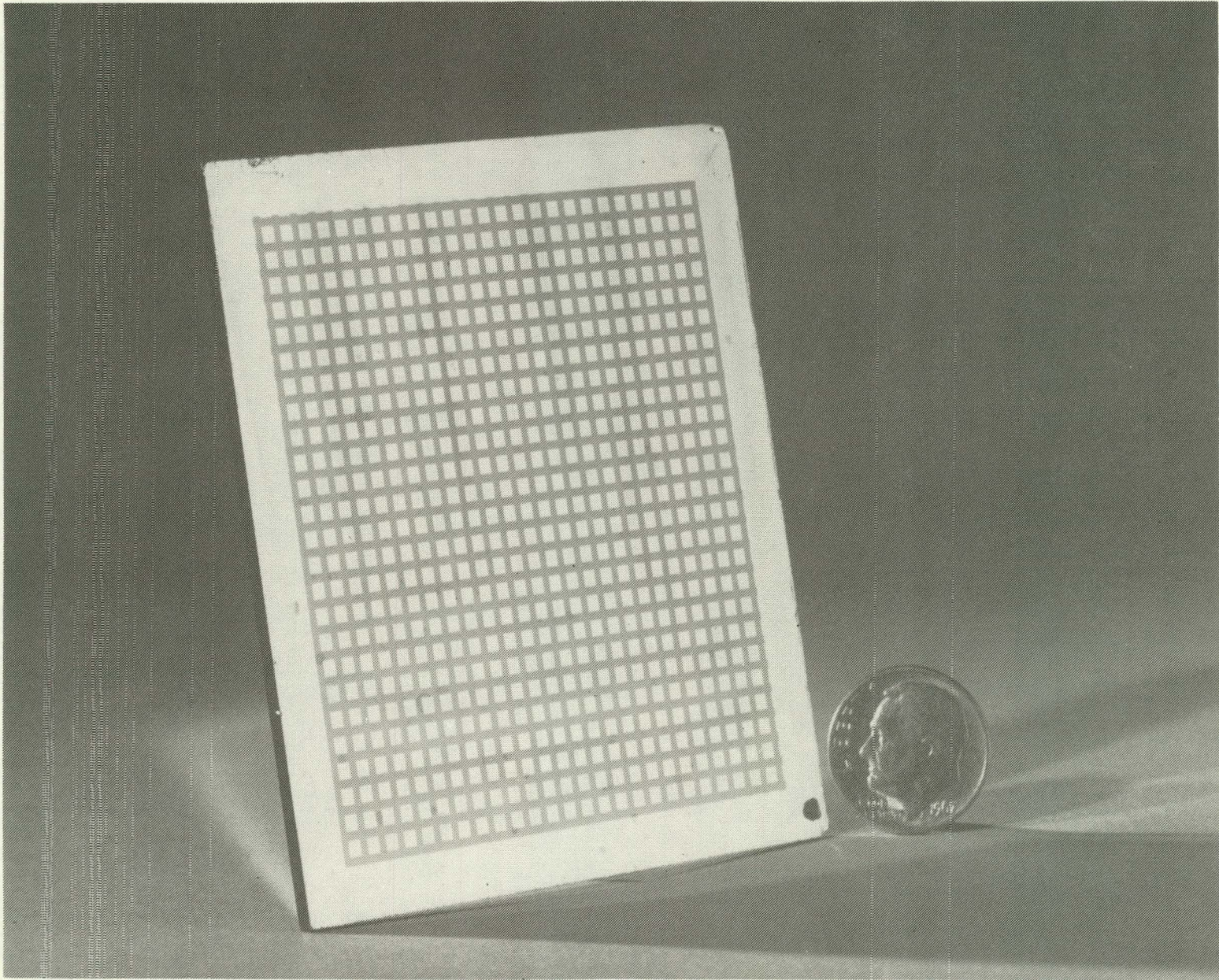
Figure 67. Rear view of a solar-cell sample having graded variables in the x- and y-directions.

The dependence of a given property on a single variable was plotted on an X-Y plot as one or more curves corresponding to one or more rows of cells. A dependence on two variables was plotted in the form of contours of the property vs the substrate coordinates which were related to the variables.

## 3. Results and Discussion

### a. Composition and Thickness of the Front Cermet Layer

Thin $Pt_x (SiO_2)_{1-x}$ cermet layers as front contacts to a-Si:H layers have been shown to enhance the performance of solar cells [76]. Whether these layers act as Schottky barriers remains to be demonstrated. They may act as controlled MI layers of MIS structures or, possibly, as tunnel junctions between the $n^+$-type ITO and the $p^+$-type a-Si:H layers.

The sample used was a solar cell having the cermet thickness variation in the X-direction from 60 Å to 260 Å and the composition in the Y-direction from 15 to 55% Pt by volume (Fig. 68). The variation was not strictly linear. The optical density decreased diagonally across the sample from 0.95 to 0.25 corresponding to the lowest and highest thickness and Pt content end points. The photovoltaic properties of $V_{oc}$, $J_{sc}$ and $\eta$ all showed distinct dependences on the transmittance, in particular $J_{sc}$, which is shown in Fig. 69. With decreasing transmittance, $V_{oc}$ decreased from 750 mV to 670 mV, and $\eta$ decreased from 1.8 to 0.6%.

In another sample having a constant Pt content of 12 vol % (near minimun tolerable because of series resistance [78]) the cermet thickness was varied in steps from 0 to 238 Å. The results shown in Fig. 70 clearly indicate inferior $V_{oc}$ and $\eta$ obtained with bare ITO and a gradual increase over the range of 120 Å. This variation is believed to be due to the porosity of the cermet film in this range of thickness.

The composition and thickness of $Pt-SiO_2$ adopted as optimum are 10 to 15 vol % Pt and 120 Å, respectively.

---

78. B. Abeles, Ping Sheng, M. D. Coutts, and Y. Arie, Advances in Physics 24, (3), 407 (1975).
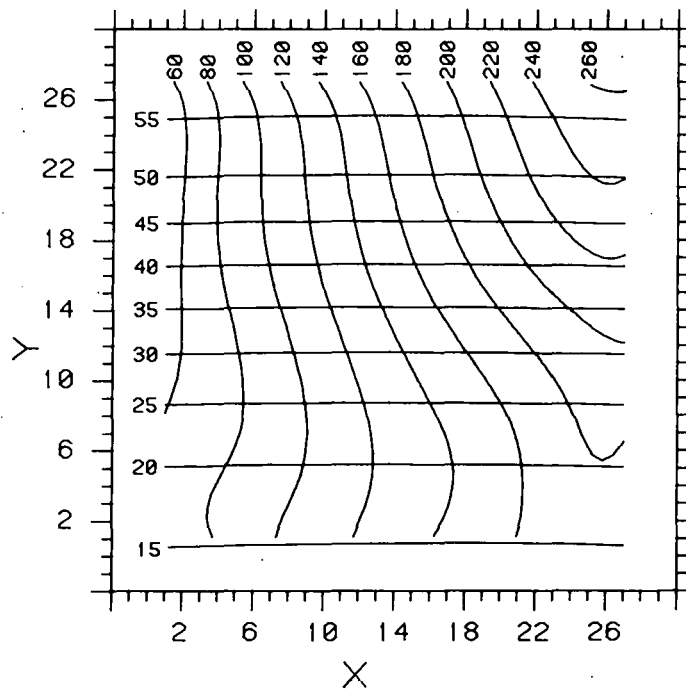
Figure 68. Contours of composition (vol % Pt, along y) and thickness (Å, along x) of the Pt-SiO$_2$ cermet as a function of substrate position.

J-SC (MA/CM2)
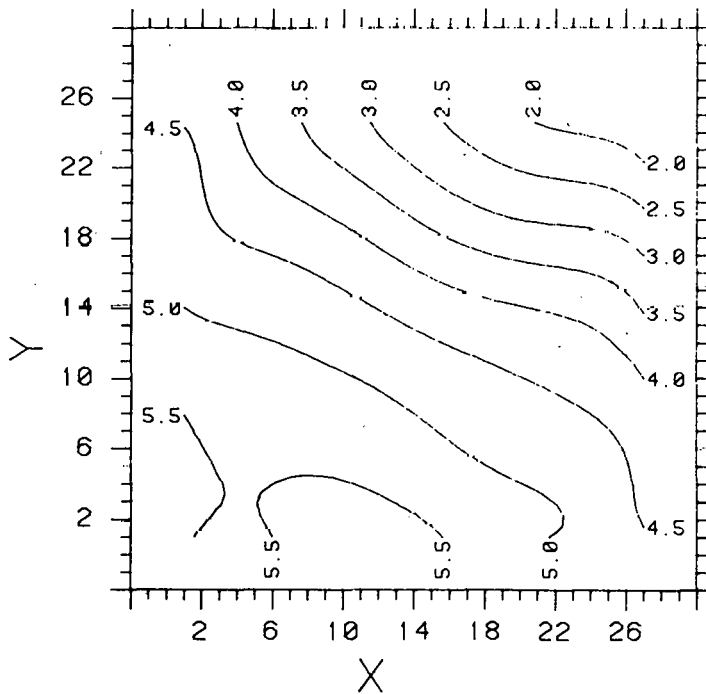


Figure 69. Dependence of J$_{sc}$ on the thickness (x) and Pt content (y) of the cermet layer shown as a function of substrate position.

103
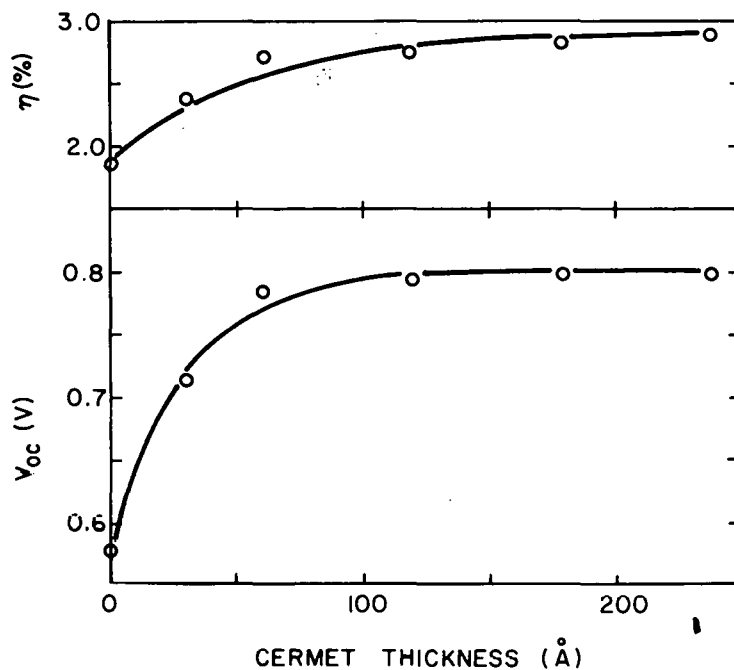
Figure 70. Dependence of cell efficiency and $V_{oc}$ on thickness of
Pt-SiO$_2$ cermet (12 vol % Pt).

b.  The Thickness of the ITO Layer

The transparent ITO front electrode doubles as antireflection (AR) coating,
having a refractive index of about 2.0 [79].  A thickness of 700 Å would be
required for a 1/4-wave AR coating at the wavelength of 0.56 μm, the point of
maximum efficiency of p$^+$-i-n$^+$ a-Si:H cells [11].  From this thickness one must
subtract the Pt-SiO$_2$ cermet thickness of 120 Å, which has similar refractive
index, leaving a net of 580 Å as the optimum ITO thickness.  The sheet resis-
tivity of such a film is just under 100 ohm/□.  A reflectance curve taken of
a cell having approximately optimum ITO and cermet thicknesses showed a minimum
of 12.5% over a broad range of the visible spectrum.  Combined losses due to
absorption and reflection were about 30% excluding absorption losses in the
p$^+$-a-Si:H layer.

c.  The Thickness of the p$^+$ a-Si:H Layer

The dependence of $V_{oc}$, $J_{sc}$, FF and η are shown in Fig. 71.  Most strongly
affected is $V_{oc}$ which rises over at least 600 Å, with the steepest rise occur-
ring at 250 Å.  The variation in $J_{sc}$ over this range is minimal due to two

79.  D. Fraser and H. D. Cook, J. Electrochem. Soc. 119, 1368 (1972).
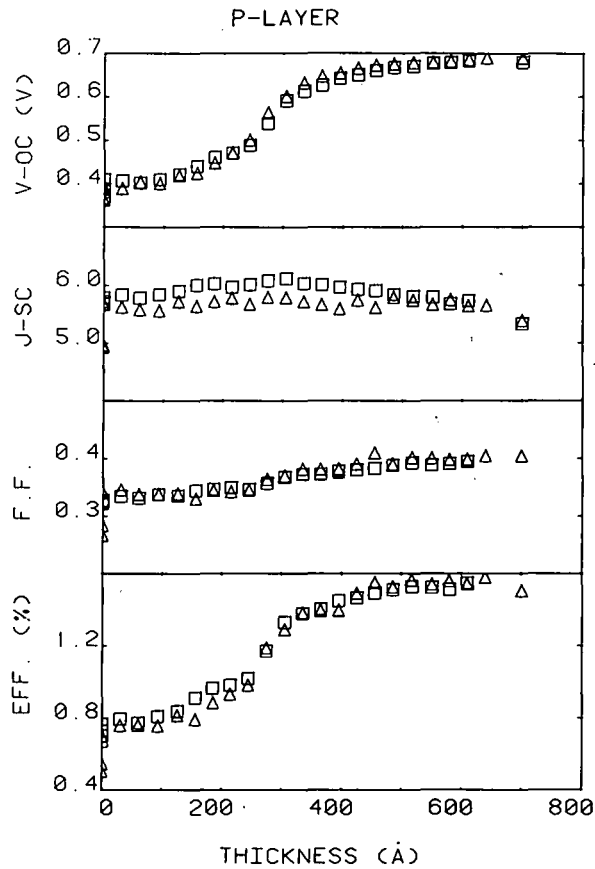
Figure 71. Dependence of $V_{oc}$ (V), $J_{sc}$ (mA/cm$^2$), FF, and $\eta$(%) on thickness of $p^+$-a-Si:H layer.

opposing effects; the increasing $V_{oc}$ tends to increase $J_{sc}$ by providing a higher field to extract carriers, while the increasing optical absorption in the $p^+$ layer tends to diminish $J_{sc}$. The FF increases monotonically with the $p^+$ layer thickness. The net result is that $\eta$ increases most strongly of the four properties and has a dependence on thickness similar to that of $V_{oc}$.

d. The Thickness of the Undoped i-a-Si:H Layer

The dependence of $V_{oc}$, $J_{sc}$ and $\eta$ on thickness of the i-a-Si:H layer are shown in Fig. 72. At zero thickness of this layer the $p^+$-$n^+$ junction shows photovoltaic characteristics although the cell performance is low. A steep, nearly linear increase in all three properties takes place in the range of 0 to 5000 Å of the i-layer thickness, which is equal to the combined reported
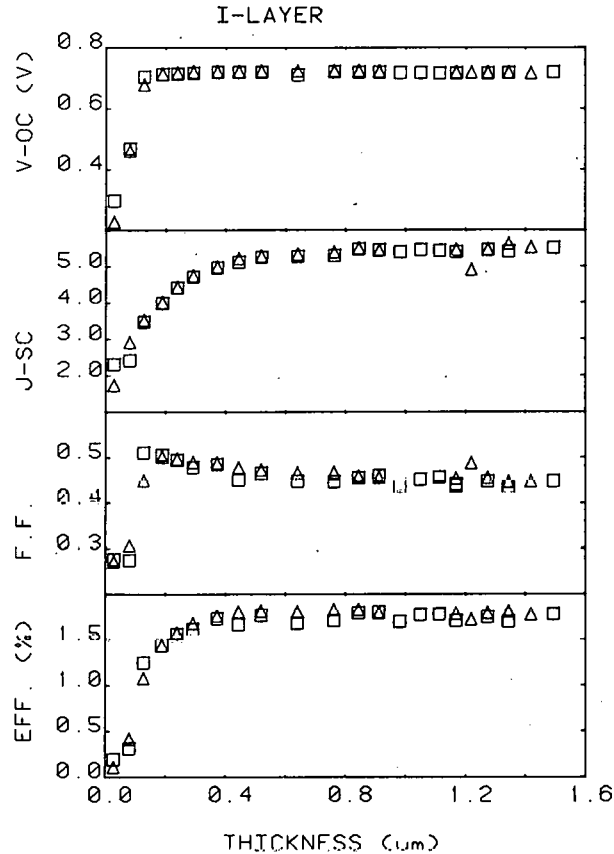
Figure 72.  Dependence of $V_{oc}$, $J_{sc}$, FF, and $\eta$ on thickness of the i-a-Si:H layer.

depletion width of 3000 Å [80] and the hole diffusion length of 2000 Å [80]. Saturation in all three properties takes place above 5000 Å, indicating that it does not pay to make the i-layer much thicker than 5000 Å.

e.  The Thickness of the $n^+$ a-Si:H Layer

The $n^+$-layer has been used in a-Si:H Schottky-barrier cells primarily for improving the ohmic contact to the back electrode [11].  Present data (see Fig. 73) indicate only a very slight increase in $V_{oc}$ (30 mV), but otherwise a gentle decrease of $J_{sc}$ and $\eta$ with the $n^+$ layer thickness.  In fact, as seen in Fig. 73 the $R_s$ is at its minimum when the $n^+$ layer thickness is zero.  Hence, there appears to be no reason for using the $n^+$ layer.  It is possible that

80.  C. R. Wronski, IEEE Trans. Electron Devices ED-24, (4), 351 (1977).
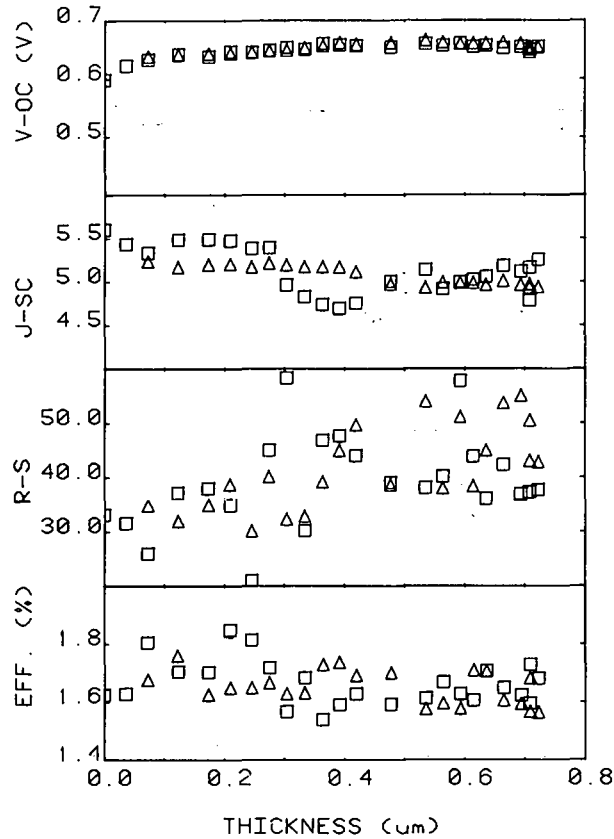
Figure 73. Dependence of $V_{oc}$, $J_{sc}$, $R_s (\Omega\text{-cm}^2)$, and $\eta$ on the $n^+$-a-Si:H layer.

rf sputtering of the back metal electrode in the present case circumvents the necessity of the $n^+$ layer, or that a very thin $n^+$ layer was deposited on the covered part of the sample.

f.  Deposition Temperature $(T_s)$ of the a-Si:H Layers

The dependences of the solar-cell performance on $T_s$ is shown in Fig. 74, which also includes data on the hydrogen content of rf (c) deposited a-Si:H. The FF is constant in this range of $T_s$ and has a value of about 0.50. The maximum in $\eta$ at 215°C can be attributed primarily to increasing $V_{oc}$ with hydrogen content, following also the dependence of the optical bandgap, $E_g$, reported earlier [72]. At temperatures below 200°C the material starts becoming more resistive and $\eta$ decreases as the electronic properties degrade [72]. Additional samples show a sharp drop in $J_{sc}$ above 370°C.

g.  Other Variables

We have studied the effect of the rate of $SiH_4$ gas flow on cell performance from 20 to 50 SCCM. The range of flow rates was sifficiently high that the rate
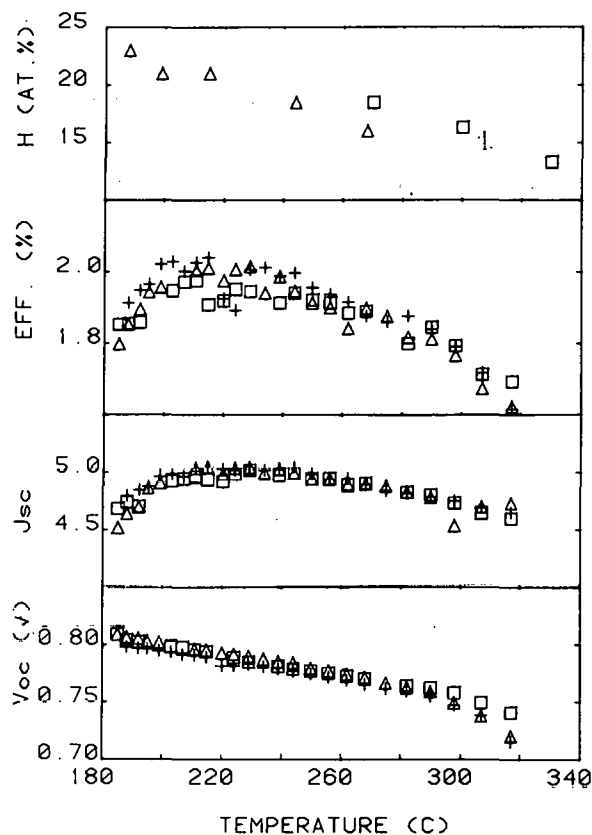
Figure 74. Dependence of $V_{oc}$, $J_{sc}$, η of the cells and the hydrogen content (at. %) of the i-a-Si:H on $T_G$.

of deposition of a-Si:H was essentially unaffected. There was a slight increase in efficiency at 30 SCCM which persisted up to 50 SCCM. Hence, the flow rate of 30 SCCM has been adopted as optimum for our deposition system.

Application of a negative bias on a substrate during rf sputtering is known to affect the properties of deposited films markedly [81]. In a cursory study we have applied a bias ranging from -70 to -340 V; η decreased from 1.8% at zero bias to 0.9% at -340 V. There was also an increase in the incidence of shorting with the bias.

Gas pressure and power applied to the discharge are known to affect the hydrogen content of a-Si:H [82]. A cursory study of the effect of pressure in the range of 5 to 200 mTorr favored the lower pressures slightly; hence, the reason for using 20 mTorr. The effect of rf power was first studied in the range of 0.15 to 1.5 W/cm$^2$. No distinct dependences were observed in the initial study.

81. J. S. Logan, IBM, J. Res. Dev. 14, (2), 172 (1970).
82. D. E. Carlson, C. W. Magee, and A. R. Triano, J. Electrochem. Soc. 126, 688 (1979).

## h. Summary of the Optimized Parameters

A summary of the results of the optimization study is given in Table 8. It should be emphasized that these data are valid primarily for the equipment, deposition technique and the cell structure discussed.above. However, it

TABLE 8.  LAYERS IN a-Si:H $p^+$-i-$n^+$ SOLAR CELLS AND
SOME OPTIMIZED INDEPENDENT VARIABLES

| Layer/Variable | Thickness Å | Composition | Depos. Temp.°C | Gas Flow Rate SCCM | Gas Pressure mTorr |
|---|---|---|---|---|---|
| ITO | 580 | - | - | - | - |
| Pt-SiO$_2$ | 120 | 10-15 vol % | 50-100 | - | - |
| P$^+$-a-Si:H | 450 | $*10^{-4}$-$10^{-3}$ $B_2H_6$/SiH$_4$ | 215 | 30 SiH$_4$ | 20 |
| i-a-Si:H | 5,000 | 21 at.% H | 215 | 30 SiH$_4$ | 20 |
| n$^+$-a-Si:H | 0-1,000 | $*2\times10^{-3}$ PH$_3$/SiH$_4$ | 215 | 30 SiH$_4$ | 20 |
| Metal | 1,500 | $*$Ti,Nb,Mo | 50-100 | - | - |

Dashed out blocks are not relevant to this study.
*Data from D. E. Carlson [83].

seems reasonable to assume that several of the optimized parameters should be valid independently of these constraints.

## i. Solar Cell Fabricated with Optimized Parameters

A $p^+$-i-$n^+$ cell has been fabricated with approximately the optimized parameters shown in Table 8.  The results in Table 9 were obtained under simulated AM1 sun illumination.

TABLE 9.  PERFORMANCE DATA FOR OPTIMIZED INVERTED SOLAR CELL

| $V_{oc}$ (mV) | $R_s$ at $V_{oc}$ (ohm-cm$^2$) | $J_{sc}$ (mA/cm$^2$) | FF | $\eta$ % |
|---|---|---|---|---|
| 796 | 22 | 7.3 | 0.507 | 2.9 |

83.  D. E. Carlson, Private Communication.

The cell had an area of 0.024 cm$^2$. The dependence of collection efficiency (C.E.) for this type of cell on wavelength ($\lambda$) is shown in Table 10 which indicates severe losses in C.E. especially at the low wavelengths.

TABLE 10.  COLLECTION EFFICIENCY OF INVERTED p$^+$-i-n$^+$ CELL VS WAVELENGTH

| $\lambda(\mu m)$ | 0.40 | 0.45 | 0.50 | 0.55 | 0.60 | 0.65 | 0.70 |
|---|---|---|---|---|---|---|---|
| C.E.(%) | 7 | 22 | 41 | 57 | 56 | 32 | 10 |

4.  Conclusions

Optimum values of several important independent variables have been determined for the layers of P$^+$-i-n$^+$ a-Si:H solar cell structure by the use of graded samples.  A solar cell made with the optimized variables and illuminated through the protective glass substrate had efficiency of 2.9%, which falls short of the best published values of 5.5% and 4.8% reported for the Schottky barrier cells [13] and for the p$^+$-i-n$^+$ cells [84], respectively.  This difference is partly due to the absorption and reflection losses of the substrate and the contacting layers (see Section B), then to strong absorption of the lower wavelengths by the p$^+$ a-Si:H layer, and, finally, to possible qualitative differences of the a-Si:H layers made by different techniques.

It is surmised that the front Pt-SiO$_2$ cermet contact enhances V$_{oc}$ and $\eta$ probably by acting as a high work-function tunnel barrier.  It has optical transmission exceeding 95% at its optimum thickness and composition.

The p$^+$ a-Si:H layer also enhances V$_{oc}$ and $\eta$ and, abruptly so, at a thickness of 250 Å; apparently, this is the minimum finite thickness needed for the formation of a p$^+$-i homojunction.

The i-a-Si:H layer enhances J$_{sc}$ within the first 5000 Å, which is the combined distance of the depletion width and the hole diffusion length.

The n$^+$ a-Si:H layer used to promote ohmic contact in Schottky-barrier cells may not be needed with inverted p$^+$-i-n$^+$ cells having rf-sputtered back-metal electrodes.

The optimum deposition temperature for the a-Si:H films deposited by the rf(c) method has been shown to be about 215°C.

The results of the preceding optimization studies indicate two major problem areas.  One of these is the low quantum efficiency of the p-i-n cell

84.   H. Okamoto, Y. Nitta, T. Adachi, and Y. Hamakawa, ICSFS, Tokyo, Japan, July 5-8, 1978.

at low wavelengths. This is due to the absorption by a rather thick (450-$\overset{\circ}{A}$)
p+ layer. Either the doping or the quality of the layer must be improved so
that a much thinner p+ layer can be used. The second problem area is the low
diffusion length in the i layer. We have decided first to seek ways to improve
the quality of the i layer.

## C. DEPENDENCE OF SOLAR-CELL PERFORMANCE ON rf POWER

One parameter that appeared likely to affect the quality of the i layer
(as well as the doped layers) of a-Si:H was the deposition rate, controlled
by the rf power. The reason for this possibility is that the kinetics of the
deposition and, hence, the structure of the a-Si:H would likely be affected
by the rate. In addition, for low rf power the bombardment of the film by
electrons and ionic species would be diminished during the growth, resulting
in less damage to the films.

In order to test the effect of rf power on cells performance, measure-
ments have been made on solar cells having the inverted structure of
glass/ITO/Pt-SiO$_2$/p+in+/Ti, and deposited in a temperature gradient of 180
to 325°C at three different levels of rf power from 0.06 to 0.9 W/cm$^2$. The
summary of the optimum performance values are given in Table 11. There was
a major improvement in all performance parameters with decreasing rf power.
In addition, there was a substantial decrease in series resistance at $V_{oc}$
from >20 down to about 14 $\Omega$-cm$^2$ with decreasing rf power. Another noteworthy
result is that the optimum deposition temperature ($T_s$) shifts to lower values
with decreasing rf power.

TABLE 11. SUMMARY OF THE OPTIMUM PERFORMANCE VALUES FOR a-Si:H
SOLAR CELLS DEPOSITED IN A TEMPERATURE GRADIENT AT
DIFFERENT rf POWER

| rf Power W/cm$^2$ | Max. Eff. (%) | $T_s$ at Max. Eff. (°C) | Max. Jsc (mA/cm$^2$) | Max. $V_{oc}$ (V) | Max. FF |
|---|---|---|---|---|---|
| 0.06 | 3.0 | 190 | 6.16 | 0.867 | 0.59 |
| 0.15 | 2.6 | 200 | 6.18 | 0.848 | 0.54 |
| 0.9 | 2.0 | 250 | 5.22 | 0.791 | 0.50 |

A sample having an area of 1.57 cm$^2$ and deposited at 0.06 W/cm$^2$ at $\sim$190°C (on the same substrate as the second sample in Table 11) has been measured at simulated AM1 and 2.5xAM1 illumination. In both cases efficiency of 3% has been achieved. When measured in AM1 sunlight the efficiency of this cell was 3.2% (see Fig. 75). This is the best result to date for a large or small inverted cell in our effort. With optimized ITO the efficiency is expected to exceed 3.5%.



| V-OC | J-SC | F.F. | EFF. |
|------|------|------|------|
| 0.815 | 6.39 | 0.60 | 3.21% |
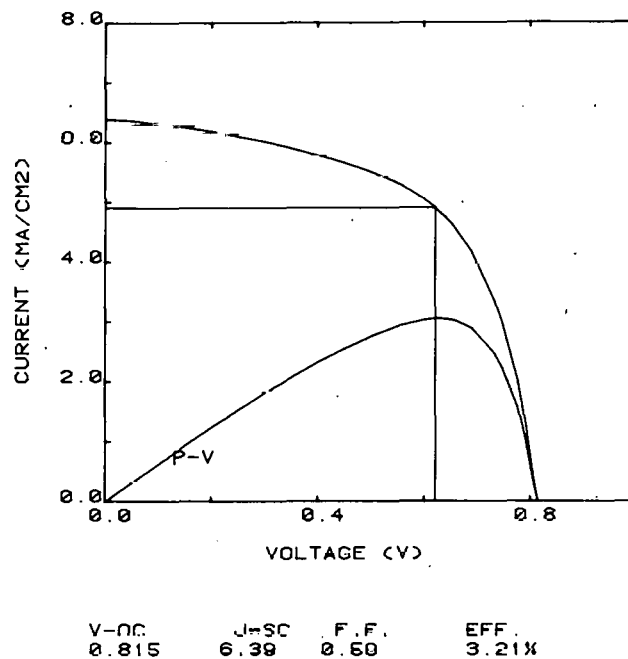
Figure 75.    I-V characteristics under AM1 illumination for a p-i-n
cell mode at low rf power.

Another important observation is that eleven or twelve 1.6-cm$^2$ cells on the substrate of the low power sample were not shorted and had an unusually high (4x10$^6$ $\Omega$-cm$^2$) dark-series resistance at a reverse bias, indicating excellent junction quality.

The reason for the improvement of solar-cell performance with decreasing rf power is apparently a decrease in the ratio of the SiH/SiH$_2$ groups in the a-Si:H, observed by H. Weakliem, as well as other groups working on a-Si:H. Interestingly, in the case of reactively sputtered a-Si:H, this ratio varies directly with rf power which was also observed by different laboratories. The shift of the optimum performance with rf power to lower temperatures is probably associated with the decrease of hydrogen content in the a-Si:H with decreasing power [82] and its increase with decreasing T$_s$ [72].

The cell yielding the 3.2% efficiency had a 360-Å thick p+ layer and a 8000-Å thick i layer.  B. Faughnan measured its quantum efficiency and found that Q.E. was only 3% at $\lambda$ of 0.4 µm, 26% at 0.5 µm, 44% at 0.58 µm and 8% at 0.7 µm.  In other words, large losses of light occurred in the substrate and layers preceding the i layer.  We expect substantial improvements in the cell efficiency by improving the light transmission into those layers.

Measurements of dI/dV at $J_{sc}$ as a function of light wavelength, done by G. Swartz on this sample, indicated that the i layer maybe fully depleted. If this is true, one can expect higher efficiency from cells thicker than 0.5 µm, which heretofore appeared to be the limiting depletion width.

## D.  DEPENDENCE OF DARK AND LIGHT CONDUCTIVITY OF p+, i and n+ a-Si:H SAMPLES ON $T_s$ AND rf POWER

In view of the improved cell performance for p+in+ cells deposited at lower rf power, two groups of p+, i and n+ a-Si:H samples have been deposited on $SiO_2$ substrates in a $T_s$ gradient of 180 to 325°C for conductivity measurements.  One group was deposited at rf power density of 0.9 W/cm$^2$ (samples 1 to 3 in Table 12) and the second group at 0.06 W/cm$^2$.  Dopant concentration ratios $B_2H_6/SiH_4$ and $PH_3/SiH_4$ of 1 x 10$^{-3}$ and 2 x 10$^{-3}$ were used for the p+ and the n+ layers, respectively.  The results in Table 12 summarize the highest conductivities obtained at corresponding $T_s$.  A comparison of samples deposited at different rf power shows: (a) a substantial improvement in photoconductivity (PC) of the p+ layer deposited at the lower power, (b) no change in PC for the i layer with power, and (c) a 10$^{-3}$X decrease in the dark conductivity and a 10$^{-1}$X decrease in PC of the n+ layer deposited at the lower power.

## E.  IMPORTANCE OF THE n+ LAYER IN THE p+in+ CELLS

The preceding data (also in Ref. 73) on the dependence of the cell performance on the thickness of the n+ layer has shown only a minor increase in $V_{oc}$ (50 mV) with the addition of the n+ layer.  In order to ascertain this result solar cells having the structure of glass/ITO/Pt-$SiO_2$/p+i a-Si:H/Ti were deposited on a substrate in a temperature gradient of 180 to 325°C, and their performance was measured.  Subsequently, the Ti layer was etched off and an n+ a-Si:H layer was deposited as well as the Ti electrodes. Figure 76 gives the comparison of $V_{oc}$ over the temperature range, showing

113

TABLE 12.  DARK AND LIGHT CONDUCTIVITIES OF a-Si:H LAYERS
DEPOSITED AT TWO DIFFERENT rf POWER LEVELS

| Sample | Type | F % | rf Power $W/cm^2$ | Light $\sigma(\Omega\text{-cm})^{-1}$ | $T_s$ (°C) | Dark $\sigma(\Omega\text{-cm})^{-1}$ |
|--------|------|-----|-------------------|---------------------------------------|-----------|--------------------------------------|
| 1 | p+ | 0 | 0.9 | $4\times10^{-6}$ | 270 | $<8\times10^{-7}$ |
| 2 | i | 0 | 0.9 | $4\times10^{-6}$ | 270 | $<8\times10^{-7}$ |
| 3 | n+ | 0 | 0.9 | $2\times10^{-3}$ | 280 | $4.5\times10^{-4}$ |
| 4 | p+ | 0 | 0.06 | $1.2\times10^{-5}$ | 180-325 | $<1\times10^{-7}$ |
| 5 | i | 0 | 0.06 | $4\times10^{-6}$ | 275 | $<1\times10^{-7}$ |
| 6 | n+ | 0 | 0.06 | $8.5\times10^{-5}$ | 300 | $<2\times10^{-7}$ |
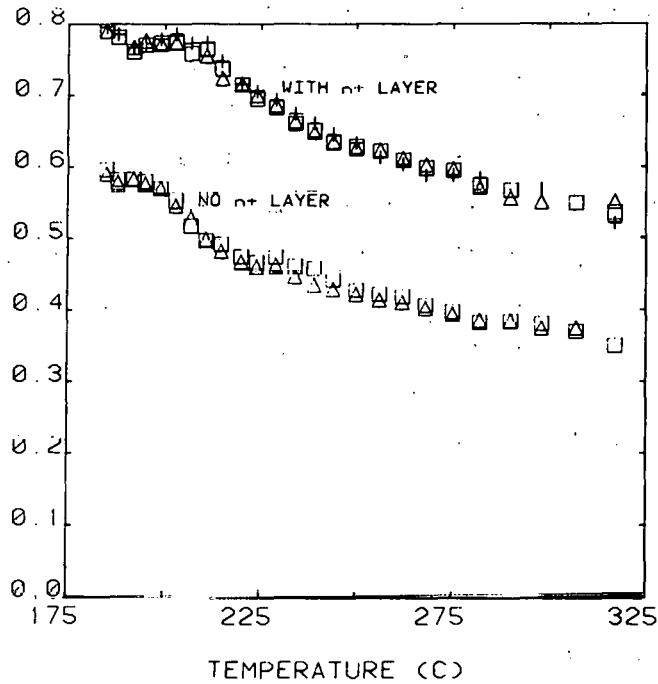


Figure 76.  $V_{oc}$ as a function of substrate temperature for cells with and without an $n^+$ a-Si:H layer.

an increase of about 0.18 V over the entire range for the cells having the n+ layer. A significant decrease in the effective series resistance and an increase in the fill factor occurred as well.

The previous result [73] which showed little effect of the n+ layer on cell performance was apparently due to the presence of a very thin n+ layer in the region of the sample where its thickness was believed to be zero (region partially covered with a shutter during the deposition).

Because of the low conductivities and photoconductivities obtained, it is imperative to study the dependence of conductivity as a function of higher p+ and n+ doping. This work is now under way.


F. CONCLUSIONS

In addition to the conclusions given in Section V.B.4., the following observations have been made:

(1) The rf power used during the deposition and, hence, probably the deposition rate, has a significant effect on the solar-cell performance. It appears that the improved performance is due to the structural changes, namely the increase of the $SiH/SiH_2$ ratio with decreasing rf power observed by other workers. In view of this result other parameters likely to affect the kinetics and the a-Si:H structure should be studied (e.g., gas pressure, cathode-substrate distance, annealing).

(2) The importance of the n+ layer in providing a substantial back field and promoting an ohmic contact has been reconfirmed.

(3) Severe light losses (reflection and absorption), perhaps as much as 50%, have been shown to occur in the inverted p+in+ structure, especifically in the glass/ITO/Pt-$SiO_2$ cermet/p+ a-Si:H layers which account for the relatively low (3.2%) solar-cell efficiency. Decrease in light losses should be sought through better light-coupling and thinner, higher-doped p+ layers.

THEORETICAL AND EXPERIMENTAL EVALUATION OF SOLAR-CELL PARAMETERS

A.  HOLE DIFFUSION LENGTH MEASUREMENTS

The hole diffusion length is an important factor in a-Si:H solar cells. It is believed to be so small that the hole collection is restricted to in and around the high field-depletion region; the rest of the cell remains inactive [13]. For this reason, we are interested in measuring the diffusion length, and finding out how it varies with deposition conditions. In the material studied, the hole diffusion length was less than 350 Å.

Our experiment was done on a large-area structure consisting of an undoped layer of graded thickness (0-1.4 μm) sandwiched between a uniform thin p+ layer, and a uniform thin n+ layer as shown below in Fig. 77. The undoped material is n-type. Thus, the depleted space-charge region was on the p+ side of the cell. The sample length was approximately 7 cm. The p+ layer was on ITO-coated glass; the n+ layer was covered with a semitransparent metal contact. The a-Si:H was made by J. Hanak of RCA Laboratories with an rf capacitance discharge at a substrate temperature of 330°C.
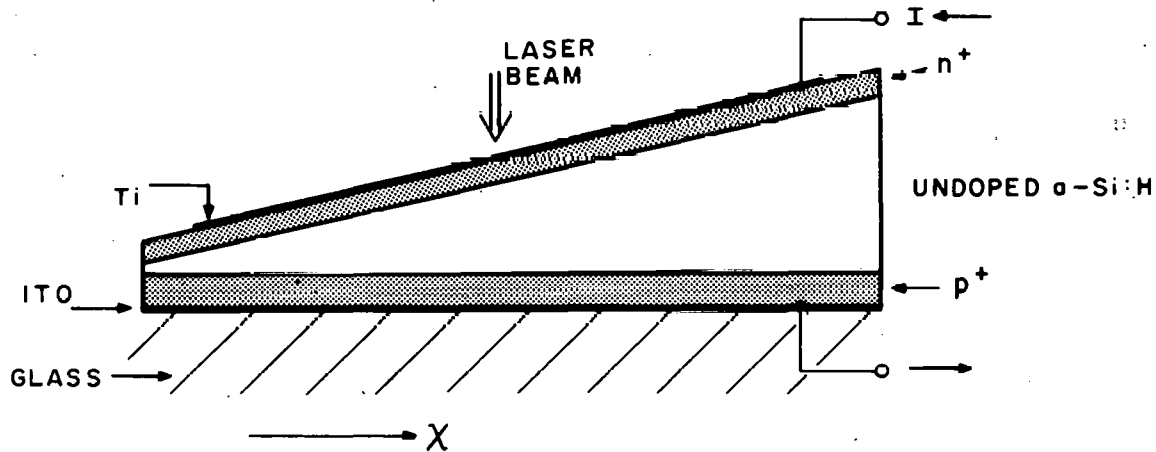


Figure 77.  a-Si:H Structure used for hole diffusion measurements.

The need for a graded thickness p-i-n cell is clear. Holes are minority carriers in undoped a-Si:H and, thus, are not easily measured. We did it by

116

generating hole-electron pairs on the n+ side of the structure with a ∿1-mm-
diameter HeCd laser beam ($\lambda$ = 4413 Å), and measuring the current due to holes
collected by the space charge region on the p+ side. These holes either, (1)
diffused through the undoped layer into the depletion region, or (2) were
generated in the depletion region itself. In the latter case, it is the light
that must get through the undoped layer. The only variable here is the thick-
ness of the undoped layer at the laser beam position. By repeating the measure-
ments with the laser beam at different positions, we found the variation of
current with undoped layer thickness. This was then used to evaluate the
diffusion length.

The thickness of the undoped layer, and its absorption coefficient must be
accurately known for this measurement. The thickness was measured with a stylus
profilometer. The optical absorption was measured by scanning a laser beam
along the cell, and measuring the transmitted light. This was done with (1) a
6328-Å HeNe laser and, (2) a 4413-Å HeCd laser. The variation of transmitted
light with undoped layer thickness gave the absorption coefficients. The
results agreed with those of Zanzucchi et al. [35] on material made under
similar conditions. For the HeCd laser beam, the penetration depth ($1/\alpha$)
was 350 Å.

The HeCd beam was then used to generate current. With the beam on the
thin end of the structure (on the left in Fig. 77), it generated a dc current
with a polarity consistent with the collection of holes on the p+ side. There
were also two pulses; one when the light was turned on, and one when it was
turned off. With the beam at the thick end, only the pulses were seen. Their
polarity and variation with light intensity were consistent with a Dember effect
due to electrons that quickly diffused into the undoped layer until steady-
state was set up. The dc current is of interest here. This is shown plotted
in Fig. 78 as a function of thickness. There is a break at ∿0.3 μm, after
which the current (I) falls exponentially following

$$I = I_o \exp (-t/\ell)$$

where $I_o$ and $\ell$ are constants, and t is the undoped layer thickness. From the
slope we find $\ell$ = 360 Å.

Two conclusions can be drawn here. The first concerns the thickness of
the space-charge width. The break at 0.3 μm should occur when the undoped
layer becomes thicker than the space-charge width. Thus, the width is

CURRENT (A)

10^-5

10^-6

10^-7

10^-8

$\ell = 360 \text{ Å}$

0    .1    .2    .3    .4    .5    .6

UNDOPED LAYER THICKNESS ($\mu$m)
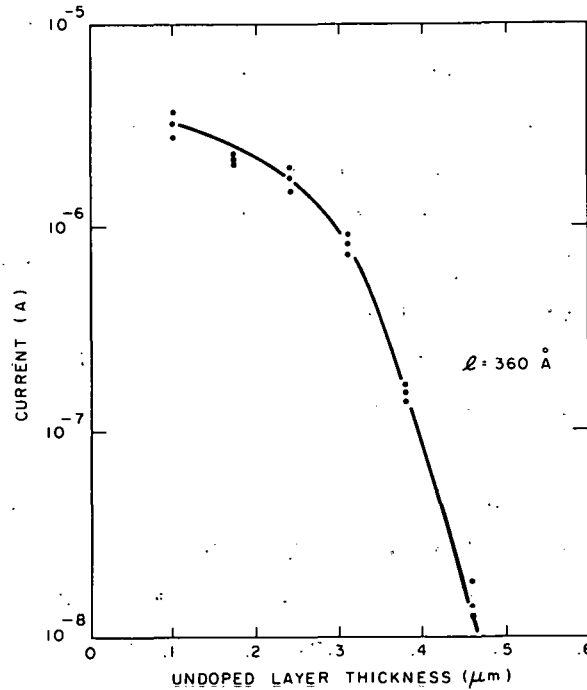
Figure 78.  Current generated by a HeCd laser beam as shown in Figure 77.

$\sim$0.3 µm.  This agrees within experimental error with short-circuit current measurements made by Hanak et al. on a similar sample [73].  Our second conclusion concerns the diffusion length.  If it is very large, then it would be given simply by the value of $\ell$.  If it is small, then $\ell$ would become $\alpha^{-1}$, the inverse of the optical absorption coefficient.  This is because in this case only holes generated inside the space-charge region are collected.  Thus, the variation with thickness must be due to the absorption of the light in the field-free region of the undoped layer.  This is what we find, at least within experimental error.  The conclusion is that the hole diffusion length is much smaller than $\sim$350 Å.  Longer diffusion lengths have been reported [80] but these were calculated from capacitance and optical measurements on a uniform, small area Schottky-barrier cell.  Our technique is, in principle, more accurate.

Crandall et al. has shown that an electric field helps to separate hole-electron pairs generated by the light [22].  Such an effect could clearly influence our results.  In their model, however, thermal effects still give a zero field-separation efficiency of 25 to 50% at room temperature, and our measurements extend over two orders of magnitude in current.  Thus, our conclusion is still valid.

From Fig. 78 and the laser power, we calculated a maximum quantum effi-
ciency (charges out per photons in) of ∿1.4%, taking reflection losses into
account. This low value can be due, in part, to absorption losses in the
upper contact and in the ∿1100-Å-thick n+ layer.

In summary, a graded thickness p-i-n cell was used to measure the hole
diffusion length. It is less than 350 Å in undoped a-Si:H made in an rf
discharge at $T_s$ = 330°C. The results also show a depletion width of ∿0.3 μm
at the p+ side of the cell.

## B. CARRIER GENERATION, RECOMBINATION, AND TRANSPORT IN a-Si:H SOLAR CELLS

### 1. Introduction

When solar cells become available in large areas at low cost, they will
make a significant contribution to our energy needs. An important step in
this direction has been the discovery of the amorphous silicon solar cell
[11]. Efforts to develop this cell are now under way in several labora-
tories [32,85-90]. The amorphous silicon material, a-Si:H, is really an
alloy that may contain as much as 30% hydrogen. Its optical properties
and the generation and transport of carriers are quite different from what
one observes in the more familiar crystalline Si solar cell [18,91]. We will
review the properties of a-Si:H solar cells, emphasizing carrier generation,
transport, and recombination.

85. I. Solomon, J. Dietle, and D. Kaplan, J. Phys. (Paris) 39, 1241 (1978).
86. J. I. B. Wilson, J. McGill, and S. Kinmond, NATURE, 272, 152 (1978).
87. W. E. Spear, P. G. LeComber, S. Kinmond, and M. H. Brodsky, Appl. Phys.
    Lett. 28, 105 (1976).
88. B. T. Debney, Solid State and Electronic Devices Special Issue, June 1978
    S-15 (1978).
89. Y. Hamakawa, H. Okamoto, and Y. Nitta, Appl. Phys. Lett. 35, 197, (1979);
    M. J. Thompson, J. Allison, M. M. Al-Kaisi, Solid State Electron Devices
    2 (1978); B. Abeles, G. D. Cody, T. Tiedje, and C. R. Wronski, 21st
    Electronic Materials Conference, Boulder, CO, June 17, 1979.
90. Y. Kuwano, J. Electron. Eng. 16, 65 (1979).
91. H. J. Hovel, Semiconductors and Semimetals (Academic Press, New York,
    1975) edited by R. K. Willardson and Albert C. Beer, Vol. 11 "Solar Cells."

## 2. a-Si:H vs Crystalline Si Solar Cells

The different optical and transport properties of a-Si:H and crystalline Si result in very different values of useful thickness for the two kinds of solar cell. Figure 79 shows this, schematically, for Schottky-barrier solar cells on n-type material. For crystalline Si solar cells, (a), the total wafer thickness is typically 250 $\mu$. For a donor concentration of $2 \times 10^{15}$ $cm^{-3}$ the Schottky-barrier thickness or depletion width, W, is 1.0 $\mu$, whereas the minority carrier (hole) diffusion length may be 200 $\mu$. Much of the useful light in the visible and near infrared spectrum penetrates into the crystal well beyond the Schottky barrier before it is absorbed. For blue light (5400 $\overset{\circ}{A}$) the mean free path of a photon before absorption is 1.4 $\mu$, and for red light (8000 $\overset{\circ}{A}$) the mean free path is 10 $\mu$. These distances are shown by arrows in part (a) of Fig. 79. The quantum efficiency for free-carrier production is nearly 1, both in the barrier and in the field-free region beyond. Since most of the light is absorbed in the field-free region, the minority carriers must diffuse to the barrier, where they are swept to the collecting electrode by the electric field in the barrier. For light in the visible part of the spectrum, the collection efficiency is high, since the minority-carrier diffusion length, $L_p$, is much greater than the penetration depth of the light. A few of the carriers recombine before being collected. Collection efficiency can be increased by making cells with suitable gradients of the donor concentration. This builds in a modest electric field that favors the transit of minority carriers to the strong field region of the barrier.

Figure 79(b) shows the contrasting properties of a solar cell made from a-Si:H. The total cell thickness is typically 1 $\mu$ and, in a good cell, W will be at least half of the total thickness. This is truly a thin-film device. Even though the layer of active material is very thin, light absorption is adequate because the optical absorption constant, $\alpha$, through the visible range, is much larger than it is for crystalline silicon [35]. Penetration depths for two wavelengths are indicated in Fig. 77(b). Much of the light is absorbed within the barrier region where there is a high-electric field. If this were not the case, the cell could not function with a useful efficiency. The reason for this is that, in a-Si:H, the photoexcitation of free holes and electrons requires in addition to light
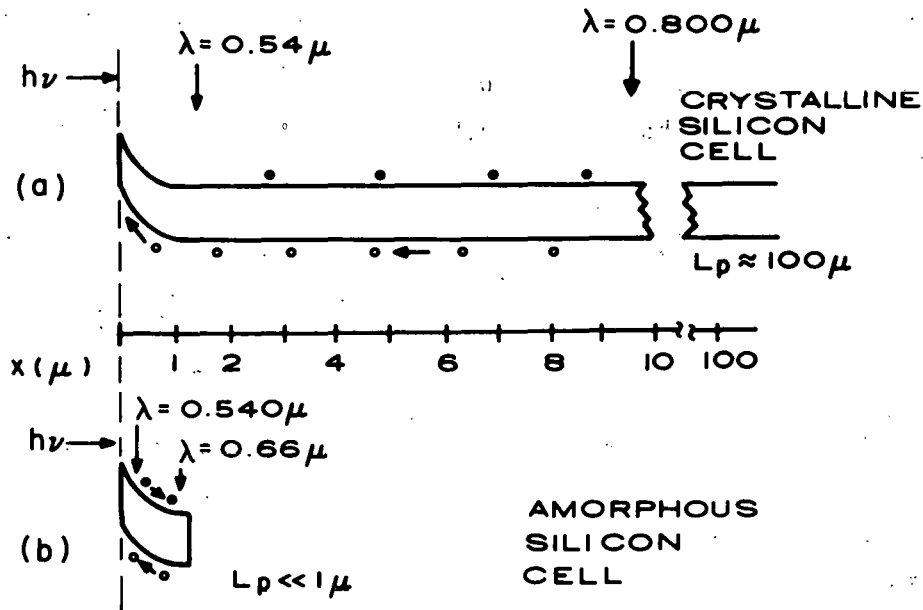
Figure 79. Comparison of the dimensions of solar cells made of single-crystal silicon and a-Si:H. (a) Single-crystal solar cell. The light penetrates far beyond the barrier region. The penetration depths for red and blue light are indicated by arrows. (b) a-Si:H solar cell. This cell is much thinner than the single-crystal cell and the optical absorption constant is larger. Arrows show penetration depths for red and blue light.

an electric field. As a result, only the light absorbed in the barrier makes a significant contribution to the solar-cell current. Once separated, holes and electrons move off in opposite directions to the electrodes. Some reach the electrodes and others recombine before doing so.

If we want to compare their behavior in solar cells, the essential distinction to make between crystalline and amorphous silicon is that between a good semiconductor and a low-mobility photoconductor. The solar cell of crystalline silicon makes effective use of the high mobility, good minority carrier lifetime, and long diffusion length that have helped to make silicon the material of choice in semiconductor device technology. It suffers somewhat from the disadvantage that the optical absorption is not very strong. To get total absorption, the cell must be thick, using more of an expensive material than one would like. The a-Si:H fits more comfortably into the family of low-mobility photoconductors that are at the heart of electrostatic

copying [92] and television camera tube technology [93]. High optical absorption and ability to deposit large areas offer the promise of thin-film solar cells that can be fabricated cheaply and still have useful efficiency. Low mobility and the other effects that go with it will mean that material control and careful design must be combined to achieve a workable solar cell with a-Si:H. In what follows, we will discuss some of the physics involved, making use of photoconductor terminology and ideas [48]. We will begin with the first thing that happens in a solar cell: production of free electrons and holes.

## 3. Carrier Generation

Many workers have indicated that coulomb attraction between hole and electron plays an important part in the photoexcitation of carriers [94-99]. This effect, often called "geminate recombination," is important in materials that have low carrier mobilities. In selenium and anthracene, for example, it can limit the efficiency of free-carrier production to low values. Mobilities in a-Si:H are also low. The microscopic mobility is the important quantity for this effect. It is estimated [2] to lie in the range 1-10 $cm^2$/V-s. Shallow trapping leads to drift mobilities that are several orders of magnitude less than the microscopic mobility [47].

Figure 80 shows the energy levels in a-Si:H that are involved in excitation and recombination. The optical bandbap is approximately 1.7 eV [35]. The attraction between electron and hole puts them in a potential well that is coulombic at large distances. At room temperature, for example the attractive energy is equal to kT at a distance of 46 Å. Luminescence experiments [12,99-101] indicate that there is a bound state, possibly involving a defect, about 0.3 eV below the ionization level.

92.  R. M. Schaffert, Electrophotography (Focal Press, New York, 1965 ).
93.  A. Rose, Vision, Human and Electronic (Plenum Press, New York, 1973).
94.  R. H. Batt, C. L. Braun, and J. F. Hornig, Appl. Opt. Suppl. (1969) p. 20.
95.  E. A. Davis and N. F. Mott, Philos. Mag. 22, 903 (1970).
96.  M. D. Tabak and P. J. Warter, Phys. Rev. 173, 899 (1968).
97.  D. M. Pai and S. W. Ing. Phys. Rev. 173, 729 (1968).
98.  E. A. Davis, J. Non-Cryst. Solids 4, 107 (1970).
99.  R. A. Street, Philos. Mag. 1337, 35 (1978).
100. T. M. Searle, T. S. Nashashibi, I. G. Austin, R. Devonshire, and G. Lockwood, Philos. Mag. 13, 39, 389 (1979).
101. D. Engemann and R. Fischer, Proceedings of the Fifth Int'l Conf. on Amorphous and Liquid Semiconductors; Garmisch-Partenkirchen (Springer, Berlin, 1973).

Figure 80.  Energy well due to the attraction between an electron and a hole
in a-Si:H.  The ionization limit is given by the optical bandgap
of 1.7 eV.  Luminescence data indicate that there is a bound
level ∿0.3 eV below the ionization limit.  The shape of the
potential energy well is coulombic at large distances, but is
probably quite different when the electron and hole are very
close together.  Energy loss by high-mobility and low-mobility
electrons is shown.

As an example of the excitation process we consider an electron excited
by a 2.0-eV photon into a level 0.3 eV above the ionization limit.  The elec-
tron will move with a velocity, v, related to its effective mass, $m^*$, assumed
equal to the free electron mass, and its excess energy, U, above the ionization
limit by:

$$v = (2U/3m^*)^{1/2} = 1.9 \times 10^7 \text{ cm/s} \tag{45}$$

It is then scattered by phonon emission or absorption, after a time, $\tau_s$, that
can be estimated from the usual relation between scattering time and the
mobility, μ:

$$\mu = e\,\tau_s/m^* \tag{46}$$

When μ is 1 cm$^2$/V-s, $\tau_s = 6 \times 10^{-16}$ s.  When $\mu = 1000$ cm$^2$/V-s, $\tau_s - 6 \times 10^{-13}$ s.
The electron moves a distance, $L_s$, before it is scattered, where:

$$L_s = v\tau_s \tag{47}$$

For the scattering length in a-Si:H we estimate $L_s = 1.1$ Å, and, in a good
semiconductor such as crystalline Si, $L_s = 1100$ Å.

In the high-mobility material the electron is well beyond the reach of the attractive force before it is scattered for the first time. Therefore, it has no chance to lose energy within the well, and all the electrons excited above the threshold ionization energy become free carriers. In the low-mobility material the electron begins to lose energy while it is still strongly attracted to the hole. It will lose energy until it has fallen to the highest bound electronic state. This is about 0.3 eV below the ionization limit and, since, by hypothesis, the electron starts out with an energy 0.3 eV above the ionization limit, it must lose, altogether, 0.6 eV to reach the bound state. Taking the dominant optical phonon energy as 0.05 eV, the electron must emit 12 phonons to do this. It may either absorb or emit phonons, but emission will predominate so that this will require a time somewhat larger than $12 \ \tau_s$. During this time it diffuses a distance $L_D$ given by:

$$L_D^2 \overset{\sim}{=} D(12 \ \tau_s) \overset{\sim}{=} (\mu kT/e)(12 \ \tau_s) \tag{48}$$

There is no true temperature for this process. The electron begins with kinetic energy of 0.3 eV and rapidly loses it by successive phonon emissions. To make a rough estimate, we take a temperature, $T^*$, that corresponds to the median energy during this process, such that $kT^* = 0.15$ eV. Using this, together with $\mu = 1$ cm$^2$/V-s and $\tau_s = 6 \times 10^{-16}$ s gives us an estimate of 3.2 Å for $L_D$. If $\mu = 10$ cm$^2$/V-s, $L_D = 32$ Å. Improving the mobility can make a significant improvement in collection efficiency.

By this rapid energy loss, an electron excited in a low-mobility material falls back into the coulomb well and does not separate from its companion hole. In the bound excited state it can recombine with the hole, with or without emission of light, or it may ionize thermally. In selenium and anthracene the probability of thermal ionization at room temperature is small. The photoconductivity quantum yield is small, unless a high-electric field is applied. In a high field the electron and hole can be torn apart by field ionization and the quantum yield increases.

The competition between recombination and ionization can be expressed by a kinetic equation containing the rates, $p_i$, for ionization, which may be thermal or field-assisted, $p_r$, for radiative recombination, and $p_n$, for nonradiative recombination. The quantum yield, $\eta_I$, for ionization is:

$$\eta_I = p_i/(p_i + p_r + p_n) \tag{49}$$

The quantum yield, $\eta_L$, for luminescence is:

$$\eta_L = p_r/(p_i + p_r + p_n) \qquad (50)$$

For a-Si:H at room temperature $\eta_L$ is small, indicating that $(p_i + p_n) \gg p_r$.
In high-mobility semiconductors at room temperature, $\eta_I$ may be nearly unity.
In this case, $p_i \gg (p_n + p_r)$. In a-Si:H and other low-mobility materials,
$\eta_I$ can be very low because of the rapid energy loss and capture in the
coulombic well that we described above. For the electron caught in the well,
the most likely alternatives available are nonradiative recombination and
thermal ionization. If there is also a high electric field, then field-
assisted thermal ionization also becomes important.

4. Field-Assisted Thermal Ionization

To escape from its well, the electron must be thermally excited over a
barrier. The electric field lowers this barrier. The effect is well known and
is illustrated by Fig. 81. The problem has been treated [25,96-98] by applying
the Frenkel-Poole model [102] for the field-assisted escape of an electron from
a bound state. The escape rate, $p_i(E)$, contains three basic terms. One of
these is an attempt frequency, $\upsilon$. The second term, $\exp(-\varepsilon_i/kT)$, expresses
the thermal ionization contribution in relation to the binding energy, $\varepsilon_i$, in
the absence of a field. The field, E, acts by lowering the barrier that the
electron must get over the escape. It comes into the third term, $\exp(E/E_f)^{1/2}$,
where $E_f$ is a constant at a given temperature. The complete equation for the
escape rate is:

$$p_i(E) = \upsilon \exp(-\varepsilon_i/kT) \exp(E/E_f)^{1/2} \qquad (51)$$

In a solar cell, some of the light is absorbed in the high-field region of
the Schottky barrier, and some penetrates beyond. Equation (51) applies in
either case. Some free carriers can be generated in the field-free region
by purely thermal ionization. Those that diffuse to the barrier will then be
collected. There is experimental evidence [24] that the diffusion length for
holes is much less than the barrier thickness in a-Si:H solar cells. This,
together with the lower ionization efficiency in the field-free region, means
that diffusion plays only a small part in the collection of carriers.

---

102. J. Frenkel, Soviet Tech. Phys. Lett., 5, 685 (1938).
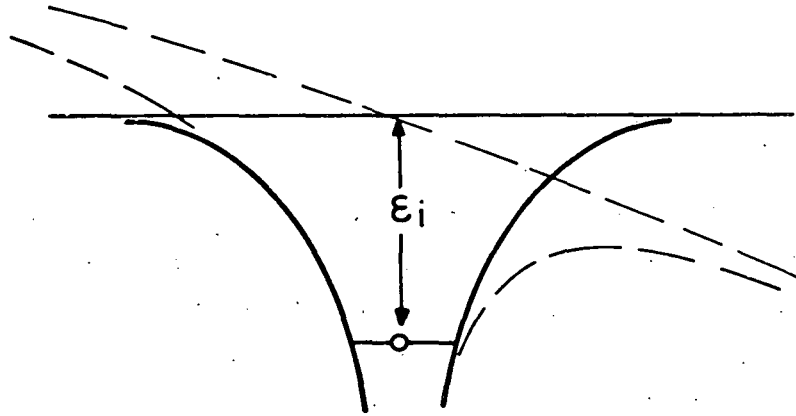
Figure 81. Effect of an electric field on the potential well. The field
lowers the barrier and allows faster thermal ionization.

Both dark photoconductivity and photoconductivity of a-Si:H depend on
electric field for fields above $10^4$ V/cm. The data fit equation (51) and
can be explained as field-lowering of a barrier to thermal ionization.
Field-quenching of the luminescence [99,101] of a-Si:H can be understood
by similar considerations. The electric field facilitates thermal ioniza-
tion of electron-hole pairs before they can recombine radiatively.

These effects are important to solar-cell performance because they deter-
mine the magnitude of the solar-cell collection efficiency, $\eta_{sc}$. We define
$\eta_{sc}$ as the number of electron charges passing through the cell for each ab-
sorbed photon. It has a maximum value of 1 and depends on wavelength and the
field in the barrier. The barrier field depends on the depletion width, W,
and the potential difference across the barrier. For an ideal Schottky
barrier:

$$E(x) = (4\pi N_s e W/\varepsilon_s)(1-x/W) = E_{max}(1-x/W) \qquad (52)$$

Here $N_s$ is the concentration of ionized donors in the barrier, e is the elec-
tronic charge, $\varepsilon_s$ is the dielectric constant, and x is the distance into the
barrier, measured from the metal contact where the field has its maximum value.
By combining Eq. (52) with Eqs (49) and (51) we can show that the molecular
quantum efficiency, $\eta_{sc}$, depends on W in the following way: [25]

$$\eta_{sc} = \alpha(W-W_o) \qquad (53)$$

The expression (53) applies only to the case of uniform light absorption when $\alpha W \ll 1$. $W_o$ depends weakly on W, but is nearly constant. Specifically:

$$W_o = \pi^2 E_f \varepsilon_s / 6 N_s e \tag{54}$$

where

$$E_f = \pi \, K \, e^3 \, (kT)^2 \tag{55}$$

We have data for $\eta_{sc}$ as a function of W for many a-Si:H solar cells [22]. They confirm that equation (53) is a correct description. W can be varied, in a given solar cell, by varying the applied voltages, and $\eta_{sc}$ measured at each voltage. Figure 7 shows representative data. We determined W from measurements of small-signal capacitance, using a measuring frequency of 100 kHz. In the following section we will discuss the validity of capacitance measurements for the determination of W. The results of Fig. 82 and similar data on other samples give strong evidence that free-carrier generation takes place mainly in the Schottky barrier, and that we are dealing with the geminate-recombination process treated above.
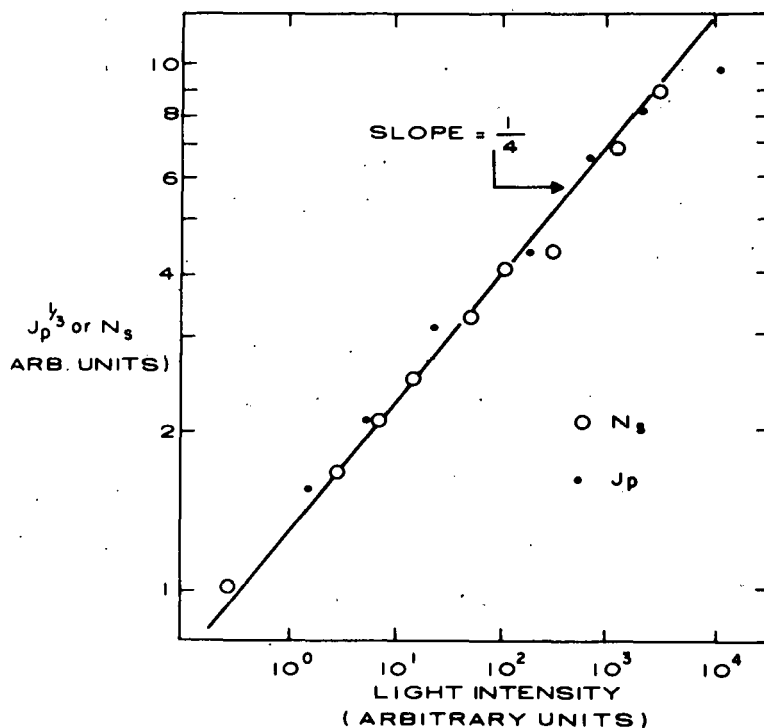


Figure 82.  Dependence of space charge density, $N_s$, and photocurrent, $j_p$, on light intensity, I. Circles show $N_s$; Squares show $j_p$. Pt-a-Si:H solar cell. Further details of the experiment are described in the text.

127

Details of the data are consistent with the picture we have developed. For example, at a given level of illumination, the magnitude of $W_o$ is fixed. However, it varies with illumination, because $N_s$ varies. The product, $N_s W_o$, however should be independent of intensity, since $E_f$ and $\varepsilon_s$ are material properties, independent of light. By varying light intensity we can vary $N_s$ by two orders of magnitude. At this time, the product $N_s W_o$ remains constant, within experimental error.

## 5. Barrier Thickness

Hole diffusion lengths in a-Si:H are short [24]. Therefore, collection of free carriers takes place mainly in the depletion layer where there is a high field. The depletion width depends on solar-cell bias and on light intensity. For an ideal Schottky barrier:

$$W = (2e\varepsilon_s V/N_s)^{1/2} \qquad\qquad (56)$$

$V$ is the total voltage drop across $W$, $N_s$ the space charge, assumed uniform. It can depend on light level because holes and electrons are not necessarily trapped in equal numbers. Usually, more holes than electrons are trapped, and, with increasing light intensity, there is an increase in $N_s$, along with a decrease in $\eta_{sc}$. Both $\eta_{sc}$ and $N_s$ vary weakly with light intensity, I. We show an example of this in Fig. 82 where we have plotted $N_s$ vs I for a Pt-a-Si:H Schottky-barrier solar cell illuminated with uniformly absorbed light. To determine $N_s$ we measure the capacitance C, as a function of applied voltage. The data, plotted on a log-log scale, fit a straight line with a slope of 1/4.

We want to use this relation to test the consistency of the values of W that we determine from capacitance measurements and that went into our determination of $N_s$. To do this, we have measured the photoconductivity current, $j_p$, as a function of I for the same sample shown in Fig. 82. The photoconductivity can be related to $N_s$ by a simple conventional model and the results compared with those that we get from capacitance data. If the results are consistent, this supports the validity of capacitance measurements as a tool to measure W.

The photoconductivity depends on $N_s$ because the lifetime of majority carrier electrons is determined by their recombination with trapped holes.

Specifically, the electron lifetime, $\tau_e$, is proportional to $1/N_s$. We can relate $j_p$ to the photogeneration rate G, for free-hole-electron pairs, the mobility, $\mu$, and the sample length, L by:

$$j_p = eG\mu\tau_e V/L \qquad (57)$$

Since G is proportional to light intensity we can write, for the overall intensity dependence, $j_p \propto (I/N_s) \propto I^{3/4}$. Thus, $j_p$ should vary with light intensity as $I^{3/4}$. A sublinear variation of $j_p$ with light intensity has previously been reported [80] for a-Si:H. We have done a different kind of measurement, using a solar cell under forward bias, to measure the ohmic secondary current as a function of I. The results are plotted in Fig. 82, as the quantity, $j_p^{1/3}$. According to the above arguments, this should be proportional to $I^{1/4}$. The graph shows that this is, indeed, the case. The good agreement between these data and the theoretical model supports the validity of capacitance measurements as a tool to determine W.

Another way to estimate the depletion layer thickness is to measure collection efficiency for different wavelengths of light. If efficient collection takes place only within the depletion layer, then we can expect a close relation between $\eta_{sc}$ and the penetration depth of the light. By comparing values of W estimated this way with those obtained from capacitance measurements on the same sample we can make a further consistency check. In one case [80] $\eta_{sc}$ was found to be proportional to the penetration depth of the light. In another kind of experiment, $j_{sc}$ was measured for different wavelengths, along with the slope of the j-V curve near V = 0. This can be related to W if one assumes that collection is confined to the barrier region [103]. Again, values of W found were in good agreement with those estimated from capacitance measurements on the same sample. Therefore, we conclude that capacitance measurements on illuminated samples, using a measuring frequency around $10^5$ Hz, give a valid measure of W.

Measurements of capacitance at low frequencies (<100 Hz) often indicate a much smaller W than one would infer from other measurements on the same sample, such as optical properties. This may be due either to deep states in the silicon or an oxide layer at the interface [104]. There has been

---

103. G. Swartz and R. Williams, to be published.
104. I. Balberg and D. E. Carlson, Phys. Rev. Lett. 43, 58 (1979).

some controversy [21,105,106] about the proper interpretation of capacitance measurements in a-Si:H diodes. One problem is that C depends strongly on the measuring frequency, particularly at very low frequencies. Part of this is due to the emptying and filling of the high concentration of states that lie deep in the forbidden gap. At high frequencies (>100 Hz) these states cannot follow the ac measuring signal and make no contribution to the measured C. At lower frequencies they make a significant contribution. The series capacitance of the oxide layer that is often found between metal and semi-conductor begins to dominate at low frequencies. Most of the controversy centers around measurements made in the dark. In this case, the Fermi level is near midgap and deep states near the Fermi level make an important con-tribution. Results on samples measured under illumination are usually simpler. The Fermi level is now closer to the conduction band and the dielectric re-laxation time shorter, $10^{-8}$ s in sunlight. There is now enough charge in shallow centers for $\Delta Q$ to respond to a change of $\Delta V$ fast enough to follow a measuring signal of $10^{5}$ Hz and the resistance of material in series with the barrier is not a problem. At the same time, the deep centers do not respond. In this way differential capacitance measurements can give a true measure of W if the measuring frequency and experimental conditions are properly chosen. At too low a frequency the series capacitance of the oxide will give a spurious result.

6. Carrier Recombination in the Barrier

As we have shown above, most of the photovoltaic current is due to carriers excited in the barrier region. What happens to the free electrons and hole, once they are formed? The separated carriers move off in opposite directions to be collected at the electrodes. Ideally, all would reach the contacts and give a current flow equivalent to one electron passing all the way through the sample for each hole-electron pair excited by the light. In practice, electrons and holes may recombine along the way and never reach the electrodes. This reduces the current by the ratio of the distance traveled before recom-bination to the total solar-cell thickness. We would expect little direct

105. C. R. Wronski and T. Tiedge, 8th International Conference an Amorphous and Liquid Semiconductors, Cambridge Mass. Aug. 27-31 (1979).
106. W. E. Spear, P. G. LeComber, and A. J. Snell, Philos. Mag. 38, 303 (1978).

recombination of holes and electrodes with each other in the barrier. The high field that prevents geminate recombination probably acts to prevent recombination of the free carriers, once they are separated. However, more complicated processes may take place, such as capture by a neutral center, followed by recombination.

We can understand some of the possible effects of recombination on solar-cell performance by references to Fig. 83. The barrier region is similar to an insulator with one blocking contact and one ohmic contact. Both holes and electrons can <u>leave</u> freely through the contacts, but only electrons can <u>enter</u> freely. If there is no trapping or recombination every free hole and electron produced leaves the barrier and makes its full contribution to the photovoltaic current. This is the ideal behavior, and, in silicon single-crystal solar cells, to a high degree of approximation, it is achieved. In a-Si:H there is shallow trapping [47] to complicate this picture and, possibly, significant recombination. Where there is shallow trapping, carriers jump in and out of traps repeatedly. The drift mobility is greatly reduced. Nevertheless, carriers can reach the contacts and make their full contribution to the current. Recombination is more serious. How serious depends on how far carriers go, on the average, before recombining. In insulator physics this distance is defined as the "Schubweg," the product mobility, $\mu_p$, electric field, E, and recombination lifetime. We consider holes with recombination lifetime, $\tau_p$.

$$S = \mu E \, \tau_p \qquad\qquad (58)$$

The effect on the solar-cell current can be shown by a simple analysis. For this, we use as the model a "Mott Barrier" [107], drawn in Fig. 83. It is the same as the usual Schottky barrier, except that the field within the barrier is constant. This has little effect on the physics, but makes the problem mathematically simpler. Actually, this is a good description of the best solar cells.

We consider a separated electron-hole pair, formed at a distance, x, from the interface by the combined action of the barrier field and light. The probability that the electron will reach the interface before recombination is

107.  N. F. Mott and Gurney, <u>Electronic Processes in Ionic Crystals</u> (Dover Publications, New York, 1964) p. 179.

131
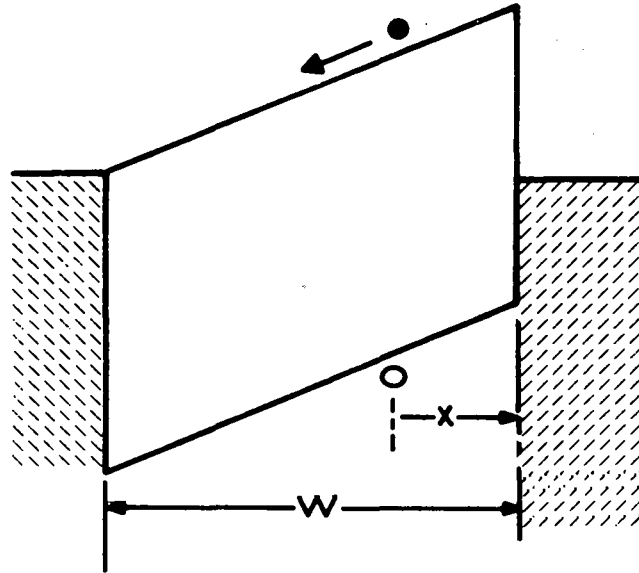
Figure 83. Mott barrier.

$\exp(-x/S)$. By averaging this over all values of x through the barrier thickness, W, we get the fraction, f, which is the ratio of the actual current to that which would flow if all carriers passed all the way through the barrier. For simplicity, we take the case of uniform illumination, for which carriers are produced uniformly through the barrier [108].

$$f = \frac{\int_0^W e^{-x/S} dx}{\int_0^W dx} = (S/W)(1 - e^{-W/S}) \tag{59}$$

Table 13 shows the magnitude of this function for several values of S/W. The schubweg must be several times W to avoid serious effects on solar-cell current and efficiency due to recombination. For highest efficiency one needs $S/W \simeq 10$. This means that the concentration of recombination centers must be controlled.

TABLE 13. EFFECTIVE RECOMBINATION ON COLLECTION EFFICIENCY

| S/W | f |
|---|---|
| 0.1 | 0.1 |
| 0.5 | 0.43 |
| 1.0 | 0.63 |
| 2.0 | 0.79 |
| 10 | 0.95 |

108. K. Hecht, Z. Phy. 77, 235 (1932).

132

We can estimate the upper limit to the concentration of recombination centers that can be tolerated in a solar cell without loss of efficiency. In a good a-Si:H solar cell, W is $10^{-4}$ cm and the barrier height is 1 eV, giving a mean field in the barrier of $10^4$ V/cm. $\mu_p$ is around 1 cm$^2$/V-s [47] and $\mu E \tau_p/W$ should be greater than 10. Thus $\tau_p > 10^{-7}$ s $\tau_p$ is related to the concentration, $N_r$, of recombination centers, their capture cross section, $\sigma$, and the thermal velocity, $v_{th}$, of the electron or hole by:

$$\frac{1}{\tau_p} = N_r v_{th}\sigma \qquad - \quad (60)$$

The order of magnitude of $v_{th}$ is $10^7$ cm/s, giving us the criterion that $N_r\sigma$ should be less than 1 for a good solar cell. For a neutral center $\sigma$ is typically $10^{-15} - 10^{-16}$ cm$^2$. For this kind of recombination center the concentration can be of order $10^{15} - 10^{16}$ cm$^{-3}$ without deterioration of solar-cell performance, but the concentration must not be allowed to exceed this range.

To apply the above ideas to an actual solar cell, we need some way to measure S/W. We cannot easily measure this for holes, but useful information can be gained by measuring S/W for electrons. This can be done by measuring the saturation photocurrent of the cell under reverse bias, and the ohmic secondary photocurrent under forward bias. The saturation reverse current gives the number of hole-electron pairs generated per unit time by the light. Under forward bias there may be photoconductive gain, leading to a large photocurrent. The ratio of the forward current to the saturation reverse current is equal to S/W and is proportional to the applied voltage. Figure 84 shows photoconductivity data obtained in this way.

## 7.  Metal-Insulator-Semiconductor Devices

Silicon Schottky-barrier diodes often have a thin layer of insulating oxide between metal and semiconductor. This may either be grown intentionally or appear naturally during device fabrication. In air, at room temperature, a 10-Å thick layer of oxide grows in 1 min, increasing to 20 Å within a few days. The oxide has a significant effect on electron transport across the interface, and on solar-cell performance. To assure uniformity and the desired results, it must be either carefully controlled or eliminated. Some of the results on a-Si:H solar cells can only be explained by the presence
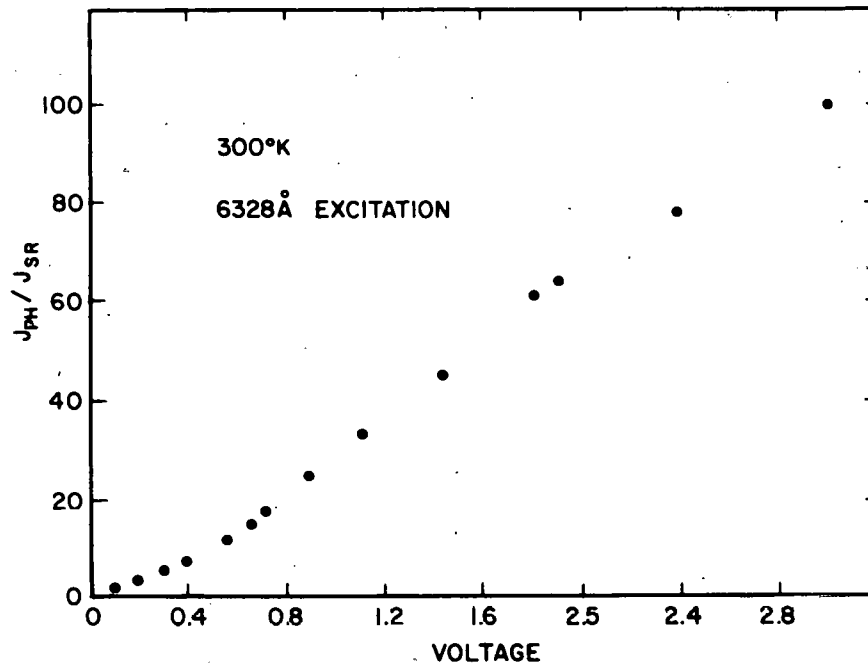
Figure 84. Ratio of forward-bias photocurrent $j_{ph}$ to saturation reverse current $j_{sr}$ as a function of applied voltage.

of such an oxide layer. For example, some Pt-a-Si:H Schottky-barrier diodes, under 1 sun illumination, have $V_{oc} \geq 0.80$ V. According to the ideal diode formula, $V_{oc}$ is related to the short-circuit current, $j_{sc}$, and the saturation current, $j_o$:

$$V_{oc} = (kT/e) \ln (j_{sc}/j_o) \tag{61}$$

For good diodes, $j_{sc}$ is around $10^{-2}$ amp/cm$^2$, and $j_o$ is $10^{-12}$ amp/cm$^2$. Thus, $V_{oc}$ should be 590 mV. The larger $V_{oc}$ actually found can most easily be explained by assuming that there is an insulating layer at the surface.

The effect of an insulating layer on solar-cell performance has been discussed in several articles [109-112]. We will use a simplified model to show the essential physics of the effect on $V_{oc}$ and will point out some of the limitations involved. Figure 85(a) shows a metal-semiconductor inter-face and 85(b) shows the same interface with a thin insulating layer between

109.  H. C. Card and E. H. Rhoderick, J. Phys., D4, 1589 (1971).
110.  R. J. Stirn and Y. C. M. Yeh, Appl. Phys. Lett. 27, 95 (1975).
111.  M. A. Green, F. D. King and J. Shewchun, Solid-State Electron. 17, 551 (1974).
112.  R. B. Godfrey and M. A. Green, Appl. Phys. Lett. 34, 790 (1979).
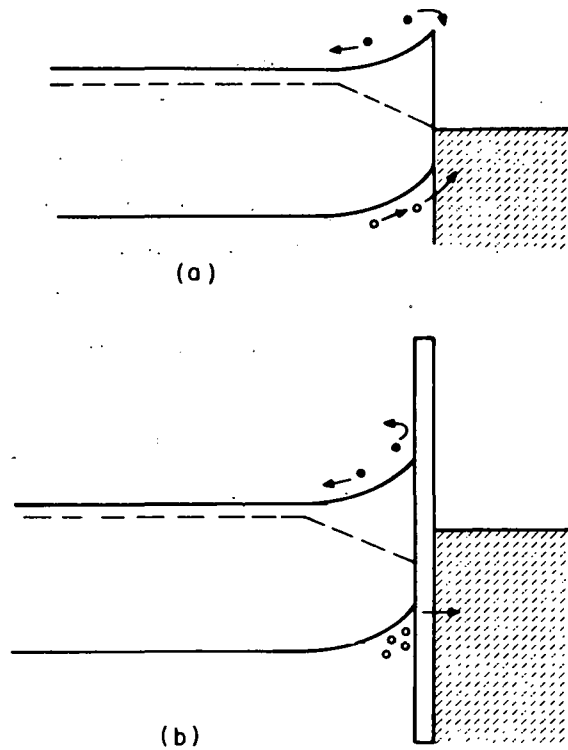
Figure 85. Schottky barriers with and without intermediate oxide layer.
(a) No oxide layer. There is no obstruction to free passage
of holes and and electrons between metal and semiconductor,
provided they have enough energy to get over the semiconductor
barrier. (b) Oxide layer turns back most carriers that arrive.
Some get through by tunneling. Effects on electrons and holes
by the barrier field.

metal and semiconductor. We assume that the presence of the insulator does

not change the amount of band-bending in the semiconductor. In both cases,

there is an exchange current of electrons back and forth, due to thermionic

emission over the barrier. The magnitude of the current in either direction

is $j_o$. In Fig. 85(a) all electrons that reach the interface with enough to

get over the semiconductor barrier pass on through the interface unimpeded.

A photoexcited hole is also shown passing freely through the interface. The

oxide layer is an obstacle to the free passage of electrons through the inter-

face. In Fig. 85(b) most of the electrons that arrive at the interface are

reflected, even those that have enough energy to get over the barrier. Some

can tunnel through the insulator with a probability given by the transmission

coefficient, T. We assume that T has the same magnitude for both electrons

and holes. However, what happens to electrons and holes is different. When

an electron arrives from the semiconductor side it is reflected, and diffuses

away from the interface. For this reason, only a small fraction, T, of the electrons coming to the interface can pass through. This is not the case for the holes. When they reach the interface they are confined there by the barrier field. They collide with the interface again and again, eventually getting through, even if T is very small. Furthermore, the recombination probability is small during their stay near the interface because the electron concentration at the top of the barrier is small. As a result, it may be possible for nearly all the holes that reach the interface to pass on through, even for small T. The effect on $V_{oc}$ comes about because we have reduced $j_o$ to $Tj_o$, while making little or no change in $j_{sc}$. In the example introduced above, $V_{oc}$ would, ideally, be 590 mV, in the absence of an insulating layer. With the insulating layer:

$$V_{oc} = (kT/e) \ln (j_{sc}/Tj_o) \tag{62}$$

To bring $V_{oc}$ up to the 800 mV actually observed requires that $T = 2.5 \times 10^{-4}$. For this, the insulating layer must be about 10 Å thick. To produce a uniform, stable layer of this thickness is a considerable achievement in technology [113].

It seems paradoxical that one can increase solar-cell efficiency by putting in an obstacle to electron transport through the interface. It is possible because the barrier separates holes and electrons, so that $j_o$ can be reduced without changing $j_{sc}$. How far can one go, in principle, to increase solar-cell efficiency in this way? There is the practical difficulty of making the thin insulator and several limitations based on the physics: (a) Once the bands in the semiconductor are flattened under illumination, nothing more can be gained. (b) Charge Separation. Holes confined near the insulator interface are imaged by an equal number of electrons that collect on the opposite side of the insulator for electrostatic reasons. This gives an electric field across the insulator and a voltage drop that is subtracted from the useful output voltage of the cell. (c) Recombination. Some of the confined holes may recombine with electrons in the semiconductor, reducing the current in the cell. We will make some estimates of the effects of these last two processes.

113.    A. M. Goodman and J. M. Breece, J. Electrochem. Soc. 117,982 (1970).

(1) <u>Charge Separation</u>. The electrostatic problem can be analyzed by considering the lifetime, $\tau_{pi}$, that a hole spends, confined near the interface, before tunneling through the insulator. The number $N_p$, of holes $cm^{-2}$ is related to $j_{sc}$ by:

$$N_p/\tau_{pi} = j_{sc}/e \qquad (63)$$

For numerical estimates we take $j_{sc} = 16$ mA/cm$^2$. We can estimate $\tau_{pi}$ from T and an attempt frequency, $\upsilon$:

$$\frac{1}{\tau_{pi}} = \upsilon T \qquad (64)$$

We assume that $\upsilon$ is $1 \times 10^{14}$ s$^{-1}$ and calculate the values of $N_p$ and $\tau_{pi}'$ that correspond to any given value of T. For a given $N_p$ we can calculate the voltage drop, $V_{ox}$, across the insulator if we know its thickness and dielectric constant. We assume an insulator 15 Å thick having a dielectric constant of 4.0. Table 14 shows the relation between T,$N_p$, $\tau_{pi}$, and $V_{ox}$ that we get in this way.

TABLE 14.   THE RELATION BETWEEN T, $N_p$, $\tau_{pi}$, AND $V_{ox}$

| T | $N_p$ (cm$^{-2}$) | $\tau_{pi}$(s) | $V_{ox}$ (V) | $N_p\sigma_{max}$ |
|---|---|---|---|---|
| $10^{-3}$ | $10^6$ | $10^{-11}$ | | $10^{-7}$ |
| $10^{-6}$ | $10^9$ | $10^{-8}$ | | $10^{-4}$ |
| $10^{-7}$ | $10^{10}$ | $10^{-7}$ | $7 \times 10^{-4}$ | $10^{-3}$ |
| $10^{-8}$ | $10^{11}$ | $10^{-6}$ | $7 \times 10^{-3}$ | $10^{-2}$ |
| $10^{-9}$ | $10^{12}$ | $10^{-5}$ | $7 \times 10^{-1}$ | $10^{-1}$ |
| $10^{-10}$ | $10^{13}$ | $10^{-4}$ | $7 \times 10^{-1}$ | $1$ |

As long as T is larger than $10^{-8}$ the build-up of charge due to the holes waiting to get through the layer of insulator will be negligible and will not affect the collection of current in short-circuit operation. At the same time, the reduction in $j_o$ achieved by the presence of the insulating layer will be substantial.

(2) <u>Recombination</u>. When a solar cell without an insulator layer, Fig. 85(a), operates at the maximum power point, the flow of holes to the

surface is accompanied by a smaller current of electrons going in the same direction. Holes and electrons enter the metal and recombine. As a result, the net current at the maximum power point is less than $j_{sc}$. For an ideal diode the current lost to this kind of recombination is about 7% of $j_{sc}$.

In the MIS diode, Figure 85(b), most of the electrons that arrive at the insulator from the semiconductor side are reflected. However, it is possible for them to recombine with the holes localized near the interface. This decreases the current and the solar-cell efficiency. To estimate the amount of recombination, we assume that the holes are localized in a plane at the interface, and that they have a capture cross section, $\sigma_e$ for electrons. The largest effect would be for a coulomb-attractive cross section $\sigma_{max}$, which is of order $10^{-13}$ $cm^2$. On each square cm of interface an area $N_p \sigma_{max}$ is blocked out by recombination centers having this capture cross section. This product, $N_p \sigma_{max}$, gives the fraction of all electrons striking the surface that recombine. As we described above, in the absence of an insulating layer, all electrons that reach the surface recombine. As long as $N_p \sigma_{max} \ll 1$, recombination of electrons with the holes at the surface will not be a serious problem in the MIS diode. The last column of Table 14 shows $N_p \sigma_{max}$ as a function of T. For values of $T > 10^{-8}$ this kind of recombination does not reduce the performance of the solar cell.

C.  CHARACTERISTICS OF Pd-SCHOTTKY-BARRIER CELLS

1.  Introduction

Hydrogenated amorphous silicon (a-Si:H) was first shown to be a promising material for low-cost solar cells by Carlson and Wronski [11]. One structure that has been used by several investigators [13,114-116] is the Pd Schottky barrier on undoped a-Si:H. While this structure is not a serious candidate for an efficient solar cell due to its low open-circuit voltage [13], it has

114.  C. R. Wronski, D. E. Carlson, and R. E. Daniel, Appl. Phys. Lett. 29, 602 (1976).

115.  W. A. Anderson, J. K. Kim, S. L. Hyland, and J. Coleman, Conf. Record of the 13th IEEE Photovoltaic Specialists Conf., Washington, DC, June 5-8, 1978, p. 755.

116.  M. J. Thompson, J. Allison, M. M. Al-Kaisi, and I. P. Thomas, Proc. ESSDERC 78, Montpelier Revue de Physique Applique, 12, 1978.

been considered a useful diagnostic tool for analyzing some properties of a-Si:H.

The structure is easy to fabricate since Pd can be thermally evaporated onto undoped a-Si:H to form near-ideal diodes [114]. Moreover, some studies at RCA Laboratories indicated good stability for unprotected Pd-Schottky-barrier cells for periods of more than one year [117].

The purpose of the present investigation is to examine the electrical and chemical properties of Pd-Schottky-barrier cells and to identify any electrical degradation mechanisms.

## 2. Experiment

The cells were fabricated by first sputter-cleaning stainless-steel substrates in an Ar dc glow discharge and then depositing $\sim$0.1 μm of phosphorus-doped a-Si:H from a discharge in a $SiH_4$ atmosphere containing $\sim$1.0 vol % $PH_3$ (corresponding to $\sim$0.6 at. % phosphorus in the film) [118]. These n+ contacting layers were usually deposited in a dc cathodic mode (with the steel substrate as the cathode) at a substrate temperature $(T_s)$ of $\sim$330°C.

The undoped a-Si:H layer ($\sim$0.6 μm thick) was deposited in either a dc cathodic or proximity mode at $T_s \sim$ 300°C; the proximity mode utilized a stainless-steel screen cathode located $\sim$1 cm above the substrates. The discharge pressure was in the range of 0.7-0.9 Torr, and the applied potential was $\sim$800-1000 V. The deposition rate was $\sim$0.45 μm/min in the cathodic mode and $\sim$0.15 μm/min in the proximity mode. In the proximity mode the substrate was allowed to float electrically so that the substrate was typically +600 V with respect to the cathode screen.

Pd dot contacts ($\sim$10 nm thick) were deposited by thermal evaporation through a metal mask (dot areas $\sim$2x10$^{-2}$ cm$^2$). No antireflection or encapsulation coatings were used on these cells. Some of the cells were stored in room ambient for periods up to two years while others were kept at 80°C for three weeks in either a rough vacuum ($\sim$10 mTorr) or a $D_2O$ saturated atmosphere. The current-voltage (I-V) characteristics of the cells were measured with an electrometer (Keithley, Model 610 C). The illumination

117. D. E. Carlson, Annual Report prepared for DOE under Contract No. EY-76-C-03-1286, Sept. 1977.
118. J. H. Thomas III, to be published.

for the photovoltaic measurements was supplied by a tungsten lamp calibrated for the same short-circuit currents produced by AM1 sunlight ($\sim$100 mW/cm$^2$).

The chemical composition of the Pd-Schottky-barrier region was examined by secondary ion mass spectroscopy (SIMS) [119], Auger electron spectroscopy (AES) and x-ray photoelectron spectroscopy (XPS or ESCA) [120]. SIMS was used to determine the compositional profiles of these devices stored in the above noted atmospheres since it is sensitive to both H [121] and D as well as Pd, Si, and O. AES and XPS were used to obtain quantitative compositional profiles for Pd, Si and O, and also to investigate the chemical bonding of these species.

3. Results for dc Proximity Films

Since our experimental results differed depending on the type of discharge used to deposit the undoped layer (dc proximity vs dc cathodic), we first consider the results for Pd contacts on undoped films made in a dc proximity discharge. Figure 86 shows the I-V characteristics in the dark for Pd contacts on undoped dc proximity films. Annealing the devices for 15 min at 200°C in 90% $N_2$, 10% $H_2$, caused some improvement in the characteristics; the diode quality factor improved slightly and the reverse saturation current density ($J_o$) decreased by almost an order of magnitude. However, storing the devices for three weeks at 80°C in saturated $D_2O$ vapor caused a significant degradation in the characteristics; the rectification ratio at $\pm$1.0 V decreased by almost three orders of magnitude. Moreover, the series resistance of the diode increased by more than an order of magnitude.

The I-V characteristics of the same devices in AM1 illumination are shown in Fig. 87. The annealing treatment increased the open-circuit voltage ($V_{oc}$) from $\sim$370 to $\sim$460 mV. The storage in $D_2O$ vapor at 80°C caused a large decrease in the cell performance. The fill factor (FF) decreased significantly (from 0.55 to 0.24), and the short-circuit current density ($J_{sc}$) decreased from 3.9 to 2.0 mA/cm$^2$.

A compositional profile obtained by AES is shown in Fig. 88 for the sample stored in $D_2O$ vapor. A SIMS analysis of the same sample showed that

119. C. W. Magee, W. L. Harrington, and R. E. Honig, Rev. Sci. Instrum. 49, 477 (1978).
120. J. H. Thomas III and D. E. Carlson, to be published.
121. G. C. Clark, C. W. White, D. D. Allred, B. R. Appleton, C. W. Magee, and D. E. Carlson, Appl. Phys. Lett. 31, 582 (1977).
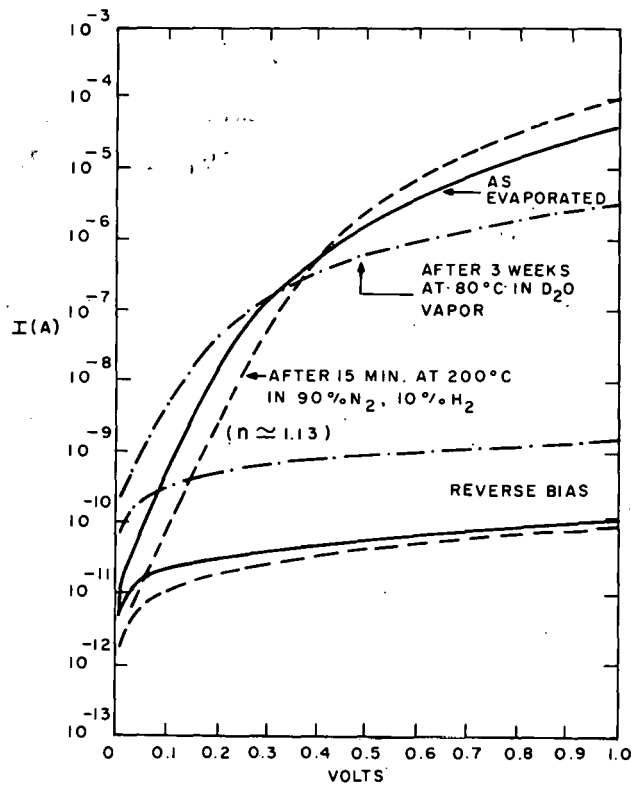
Figure 86.  I-V characteristics in the dark for a Pd contact on a
dc proximity film (Pd is + in forward bias).
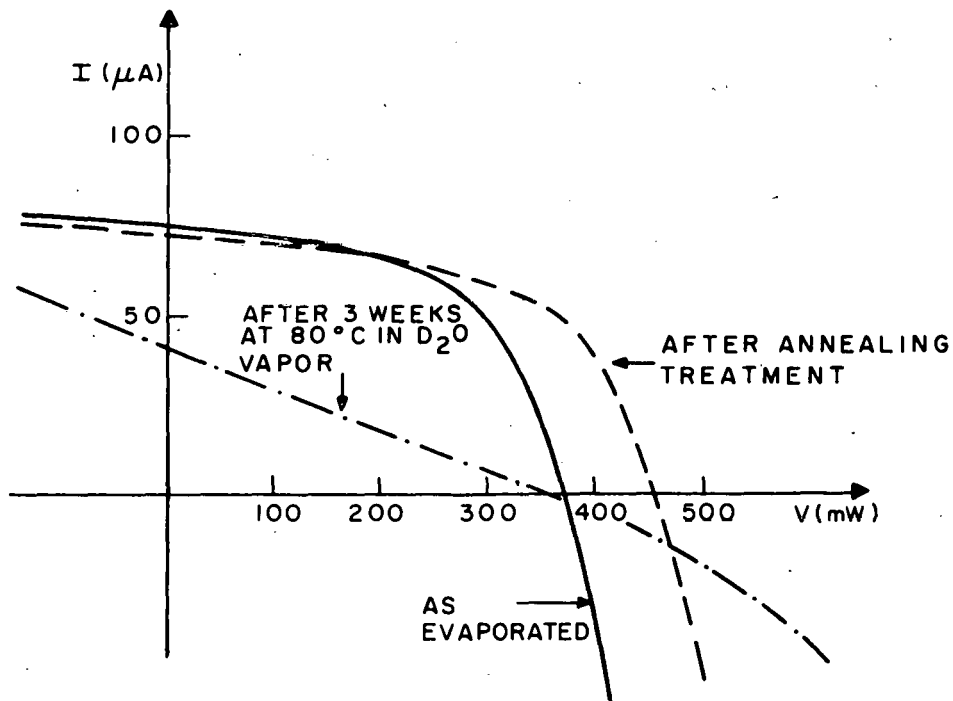


Figure 87.  I-V characteristics under ~AM1 illumination for a Pd
contact on a dc proximity film.

Figure 88. A compositional profile obtained by Auger electron spectroscopy of a Pd contact on a dc proximity film after exposure to $D_2O$ vapor at 80°C for three weeks. The D profile was determined by SIMS.

the D concentration peaked at ~4 at. % and followed the O profile. The H concentration in the a-Si:H film was ~20 at. %. The SIMS analysis showed that an accumulation of D and O occurred only beneath the Pd contact. This behavior is similar to that observed for Pt contacts on a-Si:H. The O concentration was determined by AES to be ~10 at. % near the interface [122]. Some Pd silicide was found by XPS in the Pd/a-Si:H interfacial region for the heat-treated devices (~20 at. % for the devices heated at 80°C for three weeks in $D_2O$ vapor) [120]. The O is probably present in a mixture of $SiO_x$ and OD (or OH) species.

4. Results for dc Cathodic Films

Our preliminary studies of Pd contacts on undoped dc cathodic films indicated good device stability [117]. However, the contacts changed reflective colors with time, from silver to brown to blue to yellow, over a period of two

122. D. E. Carlson and C. W. Magee, 1979 Photovoltage Solar Energy Conference, Berlin, April 23-26 1979.

years. As shown in Fig. 89, the I-V characteristic in the dark shows no signi-
ficant change in the diode quality factor (n $\sim$ 1.10) but the cell does exhibit
a higher series resistance and more leakage in reverse bias. The I-V charac-
teristics under illumination show an increase in $V_{oc}$ (by 9%) and a decrease
in $J_{sc}$ (by 14%), but the conversion efficiency is approximately unchanged
(see Fig. 90). In general, the short-circuit current densities are less
than those observed for Pd contacts on dc proximity films by a factor of
$\sim$2.
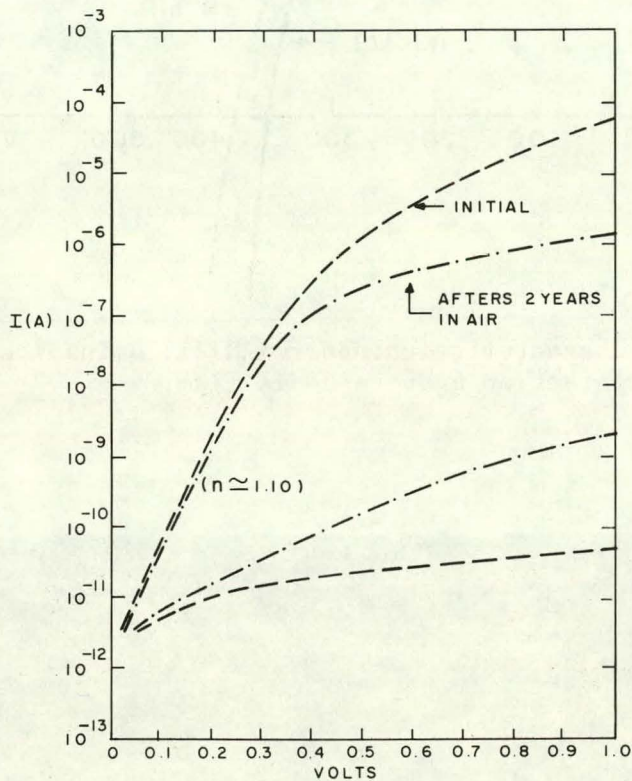


Figure 89.  I-V characteristics in the dark for a Pd contact
on a dc cathodic film.

Examination of these colored dots with scanning electron microscopy (SEM)
and stylus profilometer traces revealed that the dots were elevated with respect
to the surrounding region. As the reflective colors changed from silver to
yellow, the elevation changed from $\sim$10 nm (for as-deposited Pd contacts) to
$\sim$150 nm. Figure 91 shows a scanning electron micrograph of a dot that was
elevated $\sim$150 nm.

SIMS and AES profiles revealed considerable penetration of Pd and O into
the dc cathodic films. Figure 92 shows an AES profile of a device that had

143
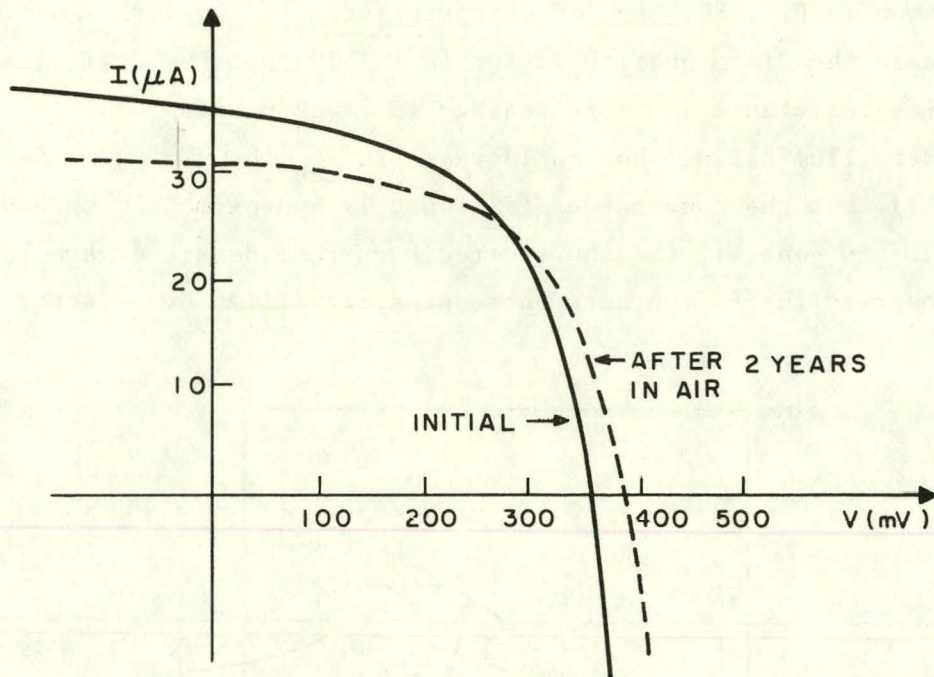
Figure 90.   I-V characteristics under ~AM1 illumination for a
Pd contact on a dc cathodic film.



→| 1μm |←
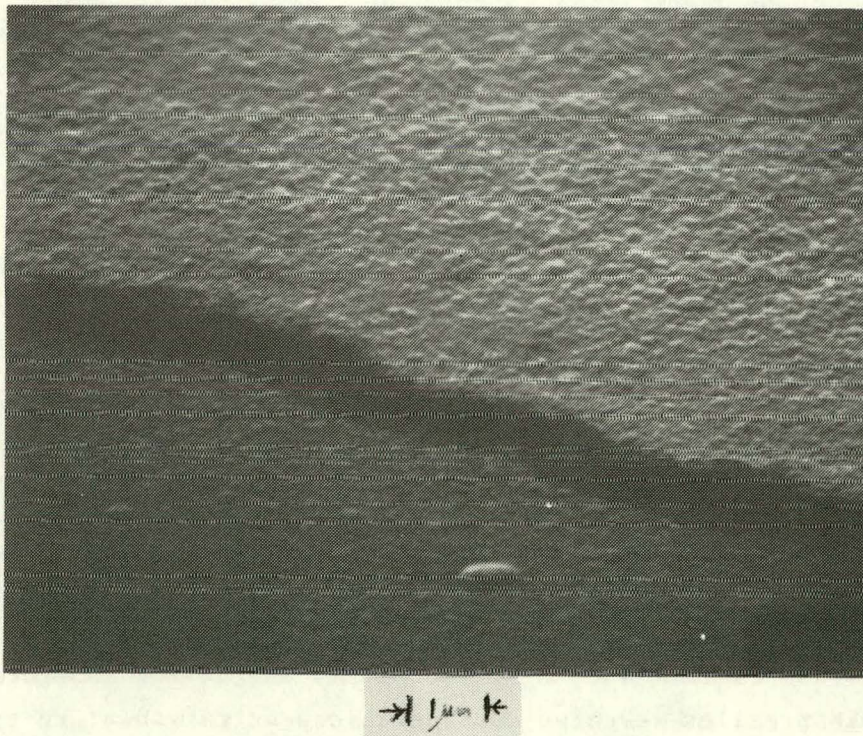
Figure 91.   A scanning electron micrograph of a Pd dot that was
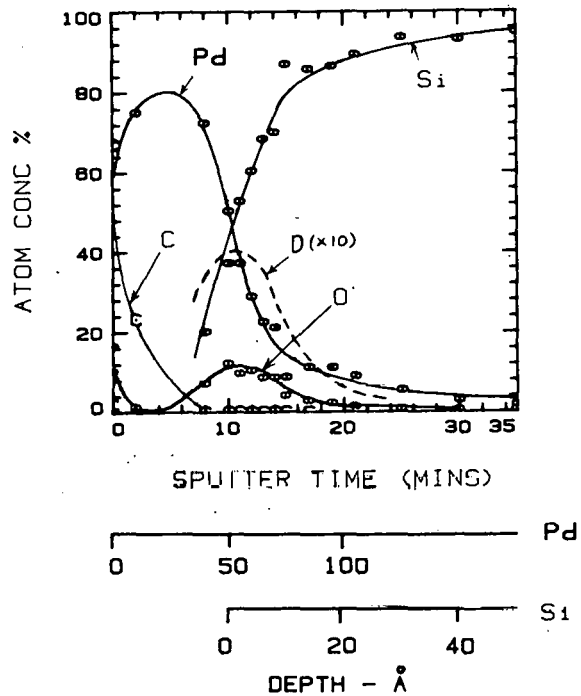exposed to air for two years.

144
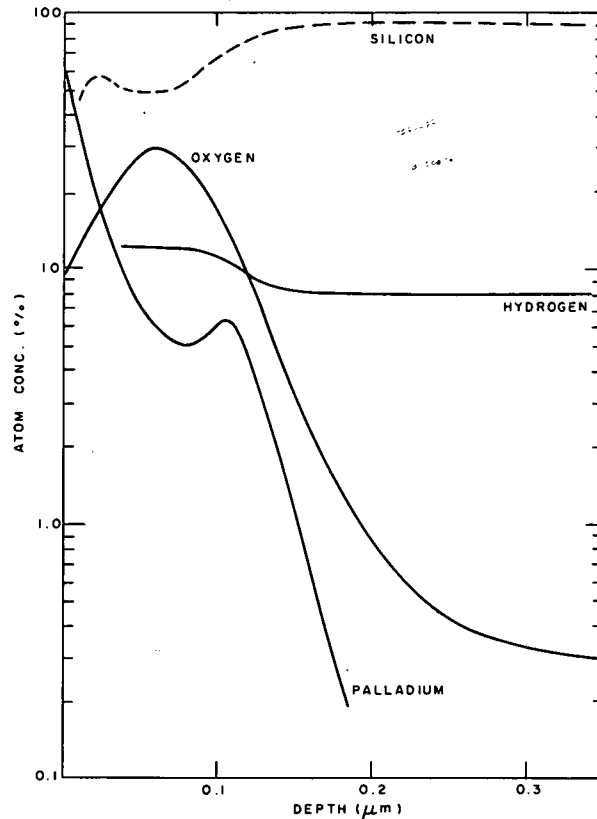
Figure 92.  A compositional profile obtained by Auger electron spectroscopy
of a Pd contact on a dc cathodic film after exposure to air for
two years.  The H profile was determined by SIMS.

been exposed to air for two years (the H profile was obtained by SIMS).  Signi-
ficant penetration of Pd, O, and H are observed.  The peaks in the Pd profile
at a depth of ∿100 nm and in the O profile at ∿60 nm were also present in
the SIMS profile.  Since the dot was elevated ∿70 nm, either the O or the Pd
peak may be located near the original interface.

Figure 93 shows a SIMS profile of a device that was stored at 80°C for
three weeks in $D_2O$ vapor.  The signals near the surface were perturbed by
charging effects due to the high resistivity of the layer.  However, the
figure shows that Pd, O, and D all penetrated into the sample to a depth
of ∿300 nm from the surface of the dot.  The dot was also elevated ∿100
nm compared to the uncoated a-Si:H surface.  The Pd concentration at a
depth of ∿200 nm was estimated to be ∿5 at. % and the oxygen concentration,
∿10 at. % from AES; the D concentration was estimated to be ∿3 at. % at the
same depth from SIMS.

COUNTS/s

$10^5$

$10^4$

$10^3$

$10^2$

10

—·—·—HYDROGEN

------SILICON

OXYGEN

DEUTERIUM

PALLADIUM

0      0.1      0.2      0.3      0.4      0.5      0.6      0.7
DEPTH ($\mu$m)
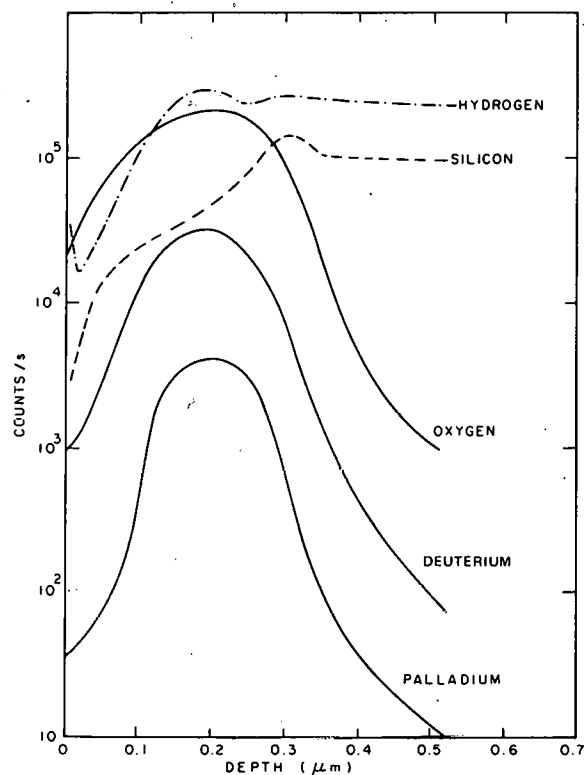
Figure 93.   A compositional profile obtained by secondary ion mass spectro-
scopy of a Pd contact on a dc cathodic film after exposure to
$D_2O$ vapor at 80°C for three weeks.

No significant penetration of Pd or O was observed by SIMS for an identical device stored at 80°C for three weeks in a rough vacuum ($\sim$10 mTorr).   In another experiment, several devices were placed in hot $H_2O$ (61°C) for 16 h with a forward bias of 1 V on one device.   Although some Pd and O penetration occurred for all dots, there were no significant differences in the SIMS profiles of unbiased and biased dots.

5.   Discussion

The results presented in Sections VI.C.3 and VI.C.4 show that Pd contacts can exhibit a wide range of behavior depending on the deposition conditions of the a-Si:H and the history of the device.   An interesting observation is that Pd contacts appear to chemically react with dc cathodic films in the presence of water vapor.   However, Pd contacts on the dc proximity films exhibit a behavior similar to that reported for Pt contacts on a-Si:H [122]

(we have never observed reflective colors for Pt contacts nor significant penetration of Pt into a-Si:H in SIMS or AES profiles).

The chemical reaction that occurs for Pd contacts on dc cathodic films does not appear to involve OH$^-$ ion injection since the bias experiment had no effect on the SIMS profiles. Moreover, the Pd interface moves inward concurrently with and D and O, and thus the Schottky-barrier region in the a-Si:H moves inward also. This penetration of the Schottky-barrier region into the a-Si:H accounts for the relative preservation of the I-V characteristics, even though the outer surface layer undergoes a significant chemical change.

The chemically modified outer layer is relatively transparent since the short-circuit density decreases only slightly ($\sim$14%), even when the modified layer is $\sim$300 nm thick. Moreover, this layer must have a density of $\sim$1.8-1.9 gm/cm$^3$ since it is $\sim$40% larger than the original volume of a-Si:H and Pd. The layer is a resistive semiconductor since we often encounter difficulties in contacting colored dots and charging effects were often observed during the initial stages of SIMS profiling. It does not appear to be a unique compound but rather a material of varying composition as shown by the profiles in Figs. 92 and 93 (i.e., the interface is not sharp but varies slowly).

Why does this chemical reaction occur for Pd contacts on dc cathodic films but not for Pd contacts on dc proximity films? We suspect the chemical reactivity is related to the microstructure of the a-Si:H films. The cathodic films are grown $\sim$3X faster than the proximity films, and thus, larger defect densities might be expected (cathodic films are bombarded by positive ions while these ions lose much of their energy before reaching a proximity film). Larger defect densities are confirmed by generally lower values of $J_{sc}$ (see Section VI.C.4).

While the hydrogen content of cathodic and proximity films are similar ($\sim$8-25 at. %), the higher defect density of cathodic films suggests that they may be more porous. The surface morphology appears to be similar to that observed by Knights et al. [19], and the "roughness" increases as the deposition rate and discharge pressure increase. However, the morphology of our films may be determined more by gas phase nucleation effects [123] due to the generally higher pressures in the dc discharges. Scanning electron

---

123. M. H. Brodsky, Thin Solid Films 40, L23 (1977).

micrographs such as shown in Fig. 91 have shown similar morphology for both cathodic and proximity a-Si:H films, and in both cases the morphology changes with deposition parameters such as power, pressure, and substrate temperature.

Although Pd does not penetrate the dc proximity films to any great extent, exposure to humidity causes both H and O to accumulate in the vicinity of the Pd/a-Si:H interface. As in the case of Pt contacts [122], this accumulation causes a severe degradation in the device characteristics (see Figs. 86 and 87).

In summary, it is evident that water vapor can adversely affect the behavior of Pd-Schottky barriers on a-Si:H. In the case of dc cathodic films, the presence of water vapor promotes a chemical reaction even at room temperature to form a new material containing Pd, Si, O, and H. While this reaction does not appear to occur for our dc proximity films, both O and H accumulate near the Pd/a-Si:H interface upon exposure to humidity. This latter phenomenon causes a larger degradation in device characteristics than does the chemical reaction observed for Pd on cathodic films. In general, Pd-Scottky-barrier cells should be encapsulated or stored in a dry environment to prevent degradation.

SUMMARY

In the past year, our research program has made significant progress in understanding the physics and chemistry of a-Si:H. We have improved the quality of undoped a-Si:H so that collection regions of $\sim$0.5 $\mu$m have been observed under illumination. Although the conversion efficiency of p-i-n cells is only on the order of $\sim$3.2% at present, we should be able to increase the efficiency of $\sim$6.5% by improving the light transmission into the collection region. Improving the quality of doped a-Si:H should allow even higher conversion efficiencies.

Transient current techniques have been used to obtain information about deep traps in undoped and lightly phosphorus-doped a-Si:H (see Section II). The experiment involves the use of injection pulses to fill deep traps in a-Si:H and extraction pulses to empty traps. The experimental data indicates that the density of trapped electrons does not saturate as the injection pulse length is increased, and thus, only the capture probability can be inferred from the measurements. The logarithmic time dependence of the trapped electron density suggests that the films are inhomogeneous with electron trapping occurring preferentially in specific regions of the sample. The analysis does place a lower limit of $\sim$10$^{14}$ cm$^{-3}$ eV$^{-1}$ for the density of bandgap states in undoped a-Si:H for states $\sim$0.20 to $\sim$0.35 eV below the conduction band. Moreover, the phosphorus-doped film does exhibit a larger density of trapped charge due either to a larger density of states or a larger electron-capture probability, or both.

An analysis of the collection efficiency as a function of the depletion width indicates that geminate recombination is occurring in a-Si:H. At a wavelength of 0.63 $\mu$m, $\sim$56% of the electron-hole pairs geminately recombine in a field-free region. However, this recombination decreases to $\sim$30-37% in the depletion region. At shorter wavelengths, the recombination in the depletion region should be even less. In fact, collection efficiencies in excess of 80% have been measured in a-Si:H solar cells at $\lambda$ = 0.5 $\mu$m. The geminate recombination may be influenced by defects in the a-Si:H, and we will look for variations in this recombination with changes in the material quality.

We have organized a coordinated fabrication and characterization program involving four different glow-discharge systems. We have found that

the optimum phosphorus-doping level corresponds to $PH_3/SiH_4 \simeq 2\times10^{-2}$ for most systems. Moreover, the conductivity increases with substrate temperature up to the highest temperatures investigated ($\sim370°C$). In the rf discharge systems, the conductivity was improved by a factor of $\sim2-10x$ when the discharge atmosphere constituted 90% $SiF_4$ and 10% $SiH_4$ (+1% $PH_3$). However, these conductivities are still a few orders of magnitude less than those observed by Ovshinsky and Madan [32]. One possible explanation for this descrepancy is that the films made in the latter work are closer to polycrystalline material due to the high rf discharge power employed.

Good quality undoped a-Si:H has been made in both an rf and dc discharge system; the a-Si:H films exhibit collection regions $\sim0.5$ μm thick when Schottky-barrier devices are exposed to AM1 illumination. Films have been made in a dc proximity discharge that exhibit essentially no IR absorption due to $SiH_2$ or $(SiH_2)_n$ groups; $\alpha(890$ cm$^{-1})/\alpha(2000$ cm$^{-1})$ is less than 0.05. Some preliminary data indicate that oxygen and nitrogen contaminants are detrimental to device performance due to a decrease in the collection region.

The rf magnetron discharge system must operate at low pressures (>10 mTorr) to produce hard, adherent a-Si:H films. However, these films exhibit a higher density of $SiH_2$ and $(SiH_2)_n$ groups than films made in other systems. Mass spectromoscopic analysis of the $SiH_4$ discharge in the rf magnetron unit indicates that $SiH_3^+$ is the dominant species incident on the substrate. Significant amounts of clusters $(Si_xH_y^+)$ are also observed in these discharges. When the discharge gas is $SiF_4$, the dominant ion species is $SiF^+$.

Adding $SiF_4$ to an $SiH_4$ discharge causes a reduction in the photoluminescence intensity of the resulting film. In general, the photoluminescence emission peak moves to lower energies as the substrate temperature increases if the $SiF_4$ content of the discharge exceeds 50%.

Photoconductivity spectra have been measured for many samples, and varying structure has been found. In some samples, a monotonic decrease of the photoconductivity occurs for $h\upsilon <1.4$ eV while in others a shoulder or a peak is observed at $h\upsilon \simeq 1.2$ eV. The observation of a peak suggests a donor-acceptor optical transition.

The photoelectromagnetic effect is being investigated as a tool to measure minority carrier diffusion lengths in a-Si:H; preliminary results indicate that the hole diffusion length in undoped a-Si:H is <400 Å. We are also investigating the photo-Hall effect as a means of measuring mobilities in a-Si:H.

Another technique that has been used to study a-Si:H is that of tunneling in MOS junctions. Structure has been found in the density of state distribution with a peak occurring ∿0.5 eV below the conduction band. This peak appears to be present both in the bulk and surface states and may be associated with dangling bonds.

A detailed study of the deposition of Pt on a-Si:H also has been performed. On crystalline Si the Pt first covers one monolayer and then islands form on top of this monolayer (the Stranski-Krastanov growth mechanism). However, on a-Si:H the Pt appears to adsorb in complete monolayers (the Frank-van der Merwe process). On oxidized a-Si:H, the Pt first adsorbs uniformly but then tends to agglomerate (the Volmer-Weber process).

Surface photovoltage measurements have been used to estimate the density of surface-state distribution for phosphorus-doped and undoped a-Si:H. In phosphorus-doped a-Si:H, the distribution has two peaks, ∿0.95 and ∿1.28 eV below the conduction band (see Fig. 54). In undoped a-Si:H, peaks are found at ∿0.7 eV and ∿1.0-1.4 eV below the conduction band. Dehydrogenation of the a-Si:H quenches all surface photovoltage effects at room temperature probably as a result of increased communication between the surface states and the band states.

Stacked (or multiple junction) cells have been fabricated with several types of interconnections between the cells. The best open-circuit voltage (1.57 V for a 2-cell stack) was obtained with a $Ti/(Pt-SiO_2$ cermet) interconnection between the n+ and p+ layers.

One specific p-i-n structure utilizing a $Pt-SiO_2$ front cermet has been partially optimized using two-dimensional graded structures and automated testing procedures. This procedure has led to p-i-n cells with conversion efficiencies of 3.2%; the efficiency is limited mainly by poor light transmission into the collection region (the average collection efficiency is <40%).

A p-i-n structure was fabricated with the undoped layer graded in thickness from ∿0 to ∿1.4 μm and then back-illumined with a HeCd laser to provide a means for estimating the hole diffusion length. This experiment places an upper limit of ∿400 Å for the hole diffusion length in undoped a-Si:H.

The operation of the a-Si:H solar cell is discussed in Section VI.C. in terms of carrier generation, field-assisted thermal ionization, the barrier thickness and carrier recombination in the barrier. We also consider some of the physics that applies to MIS devices.

Finally, we present some data for Pd-Schottky-barrier devices showing that the I-V characteristics depend strongly on the type of a-Si:H film, the thermal history and exposure to humidity.

# REFERENCES

1. R. C. Chittick, J. H. Alexander, and H. F. Sterling, J. Electrochem. Soc. 116, 77 (1969).

2. P. G. LeComber and W. E. Spear, Phys. Rev. Lett. 25, 509 (1970).

3. W. E. Spear and P. G. LeComber, J. Non-Cryst. Solids 8-10, 727 (1972).

4. P. G. LeComber, D. I. Jones, and W. E. Spear, Philos. Mag. 35, 1173 (1977).

5. D. I. Jones, P. G. LeComber, and W. E. Spear, Philos. Mag. 36, 541 (1977).

6. W. E. Spear and P. G. LeComber, Solid State Commun. 17, 1193 (1975).

7. A. Triska, D. Dennison, and H. Fritzsche, Bull. Am. Phys. Soc. 20, 392 (1975).

8. M. H. Brodsky, M. A. Frisch, J. F. Ziegler, and W. A. Lanford, Appl. Phys. Lett. 30, 561 (1977).

9. J. I. Pankove and D. E. Carlson, Appl. Phys. Lett. 31, 450 (1977).

10. D. E. Carlson, U.S. Pat. 4,064,521 (1977).

11. D. E. Carlson and C. R. Wronski, Appl. Phys. Lett. 28, 671 (1976).

12. J. I. Pankove and D. E. Carlson, Appl. Phys. Lett. 29, 620 (1976).

13. D. E. Carlson, IEEE Trans. Electron Devices ED-24, 449 (1977).

14. D. V. Lang, J. Appl. Phys. 45, 3023 (1974).

15. W. E. Spear and P. G. LeComber, Philos. Mag. 33, 935 (1976).

16. R. S. Crandall, submitted for publication.

17. J. S. Uranwala, T. G. Simmons and H. A. Mar, Solid-State Electron. 19, 375 (1976).

18. S. M. Sze, Physics of Semiconductor Devices (Wiley Interscience, New York, 1969).

19. J. C. Knights, G. Lucovsky and R. J. Nemanich, J. Non-Cryst. Solids 32, 393 (1979).

20. H. J. Wintle, IEEE, Trans. Elect. Insul. EI-12, 424 (1977).

21. G. H. Döhler and M. Hirose, Proc. 7th Int. Conf. Amorphous and Liquid Semiconductors, edited by W. E. Spear (CICL, University of Edinburgh, Scotland, 1977), p. 372.

22. R. S. Crandall, R. Williams and B. E. Tompkins, J. Appl. Phys. 50, 5506 (1979).

23. I. Shimizu, T. Komatsu, K. Saito, and E. Inoue, 8th International Conference on Amorphous and Liquid Semiconductors, Cambridge MA, Aug. 27-31, 1979.

24. D. Staebler, ibid.

25. D. E. Carlson, I. Balberg, R. S. Crandall, J. J. Hanak, J. I. Pankove, D. L. Staebler and H. A. Weakliem, Quarterly Report No. 2, prepared for DOE under Contract No. ET-78-C-03-2219, April 1979.

26. D. M. Pai and S. W. Ing, Phys. Rev. $\underline{173}$, 899 (1968); M. D. Tabak and P. J. Warter, Phys. Rev. $\underline{173}$, 729 (1968).

27. E. A. Davis, J. Non-Cryst. Solids $\underline{4}$, 107 (1970).

28. T. Suzuki, M. Hirose, S. Ogase, and Y. Osaka, Phys. Status Solidi $\underline{42}$, 337 (1977); C. R. Wronski, unpublished data.

29. R. Williams and R. S. Crandall, to be published.

30. D. L. Staebler and C. R. Wronski, Appl. Phys. Lett. $\underline{31}$, 292 (1977).

31. D. E. Carlson, R. S. Crandall, B. Goldstein, J. J. Hanak, A. R. Moore, J. I. Pankove, and D. L. Staebler, Final Report, prepared for DOE under Contract No. EY-76-C-03-1286, October 1978.

32. Stanford R. Ovshinsky and Arun Madan, NATURE $\underline{276}$, 482 (1978).

33. R. W. Griffith, F. J. Kampas, P. E. Vanier, and M. D. Hirsch, 8th International Conference on Amorphous and Liquid Semiconductors, Cambridge, MA, Aug. 27-31, 1979.

34. E. C. Freeman and W. Paul, Phys. Rev. B, $\underline{18}$, 4288 (1978).

35. P. J. Zanzucchi, C. R. Wronski, and D. E. Carlson, J. Appl. Phys. 48, 5227 (1977).

36. G. D. Cody, B. Abeles, C. R. Wronski, and B. Brooks, 8th International Conference on Amorphous and Liquid Semiconductors, Cambridge, MA, Aug. 27-31, 1979.

37. J. W. Coburn and E. Kay, J. Appl. Phys. $\underline{43}$, 4965 (1972), and references contained therein.

38. A. J. Purdes, B.F.T. Bokler, and J. D. Bucci, and T. C. Tisone, J. Vac. Sci. Technol. $\underline{14}$, 98 (1977).

39. S. Dushman, Vacuum Techniques, (J. Wiley & Sons, New York, 1966).

40. F. E. Saalfeld and H. J. Svec, Inorg. Chem. $\underline{2}$, 46 (1963).

41. T. Y. Yu, T.M.H. Cheng, V. Kempter, and F. W. Lampe, J. Phys. Chem. $\underline{76}$ 3321 (1972) and earlier work cited therein.

42. J.M.S. Henis, G. W. Stewart, M. K. Tripodi, and P. P. Gaspar, J. Chem. Phys. $\underline{57}$, 389 (1972).

154

43. G. Nolet, J. Electrochem. Soc. 122, 1030 (1975).

44. P. G. LeComber, A. Madan and W. E. Spear, J. Non-Cryst. Solids 11, 219 (1972).

45. P. G. LeComber, W. E. Spear and D. Allan, J. Non-Cryst. Solids 32, 1 (1979).

46. K. Weiser, Comments Solid State Phys. 6, 81 (1975).

47. A. R. Moore, Appl. Phys. Lett. 31,762 (1977).

48. A. Rose, Concepts in Photoconductivity and Allied Problems (Wiley Interscience, New York, 1963).

49. L. Friedman, Philos. Mag. 38, 467 (1978). D. Emin, Philos. Mag. 35, 1189 (1977).

50. P. G. LeComber, D. I. Jones and W. E. Spear, Philos. Mag. 35, 1173 (1977).

51. A. Mell, B. Movagher and L. Schweitzer, Phys. Status Solidi 88, 531 (1978).

52. P. V. Gray, Phys. Rev. 140 A179 (1965).

53. J. Shewchun, A. Waxman, and G. Warfield, Solid-State Electron. 10 1165, 1187 (1967).

54. L. B. Freeman and W. E. Dahlke, Solid-State Electron. 13 1483 (1970).

55. S. Kar and W. E. Dahlke, Solid-State Electron. 15 221 (1972).

56. For many references and detailed data see J. W. Osmun, Phys. Rev. B11 5008 (1975).

57. For a critical review, see H. Fritzche in Electronic and Structural Properties of Amorphous Semiconductors, edited by P. G. LeComber and J. Mort (Academic Press, London, 1973) p. 55.

58. Z. S. Jan, R. H. Bube, and John C. Knights, to be published in J. of Elect. Mat.

59. B. Henderson, Defects in Crystalline Solids Vol. I. (Crane, Russak & Co., New York, 1972) p. 133.

60. J. Derrien et al., Appl. Phys. Lett. 33, 881 (1978).

61. R. J. Loveland et al., J. Non-Cryst. Solids 13, 55 (1973/74).

62. A. Madan and P. G. LeComber, Proc. 7th Int. Conf. Amorphous and Liquid Semiconductors, edited by W. E. Spear (CICL, University of Edinburgh, Scotland, 1977).

63. R. Beyers et al., ibid.

64. B. Van Roedern et al., Solid State Commun. 29, 415 (1979).

65. H. K. Henisch, Rectifying Semiconductor Contacts (The Clarendon Press, Oxford, England, 1957).

66. For recent references on the subject of stacked cells see R. L. Moon, L. W. James, H. A. Van der Plas, T. O. Yep, G. A. Antypas, and Y. Chai, Conf. Record 13th IEEE Photovoltaic Spec. Conf., IEEE, New York, p. 859, 1978.

67. E. D. Jackson, Trans. Conf. on the Use of Solar Energy, Tuscon, Arizona, 1955, (U. of Arizona Press, Tuscon, 1958) Vol. 5, p. 122.

68. M. F. Lamorte and D. Abbot, Ref. 66, p. 874.

69. L. M. Fraas and R. C. Knechtli, Ref. 66, p. 886.

70. M. Arienzo and J. J. Loferski, Ref. 66, p. 898.

71. S. M. Bedair and M. F. Lamorte, Appl. Phys. Lett. $\underline{34}$ (1), 38(1979).

72. J. J. Hanak, P. J. Zanzucchi, D. E. Carlson, C. R. Wronski, and J. I. Pankove, Proc. 7th Intern. Vac. Congr. and 3rd Intern. Conf. Solid Surfaces, edited by R. Dobrozenski et al., (F. Berger and Sohne, Horn, Austria, 1977) p. 1947.

73. J. J. Hanak, V. Korsun, and J. P. Pellicane, 1979 Photovoltaic Solar Energy Conf., Berlin (West) Germany.

74. Y. Marfaing, ibid.

75. A. Onton, H. Wieder, J. Chevallier, and C. R. Guarnieri, Proc. 7th Intern. Conf. Amorphous and Liquid Semicond., W. E. Spear, edited by G. G. Stevenson (CICL, University of Edinburgh, Scotland, 1977).

76. J. C. Knights, Philos. Mag. $\underline{34}$, 663 (1976).

77. J. J. Hanak, H. W. Lehmann, and R. K. Wehner, J. Appl. Phys. $\underline{43}$,(4) 1666 (1972); J. J. Hanak and B. F. T. Bolker, J. Appl. Phys. $\underline{44}$, (11), 5142, (1973).

78. B. Abeles, Ping Sheng, M. D. Coutts, and Y. Arie, Advances in Physics $\underline{24}$,(3) 407 (1975).

79. D. Flaser and H. D. Cook, J. Electrochem. Soc. $\underline{119}$, 1368 (1972).

80. C. R. Wronski, IEEE Trans. Electron Devices $\underline{ED-24}$, (4), 351 (1977).

81. J. S. Logan, IBM J. Res. Dev. $\underline{14}$, (2), 172 (1970).

82. D. E. Carlson, C. W. Magee, and A. R. Triano, J. Electrochem. Soc. $\underline{126}$, 688 (1979).

83. D. E. Carlson, Private Communication.

84. H. Okamoto, Y. Nitta, T. Adachi, and Y. Hamakawa, ICSFS, Tokyo, Japan, July 5-8, 1978.

85. I. Solomon, J. Dietle, and D. Kaplan, J. Phys. (Paris) $\underline{39}$, 1241 (1978).

86. J. I. B. Wilson, J. McGill, and S. Kinmond, NATURE, $\underline{272}$, 152 (1978).

87. W. E. Spear, P. G. LeComber, S. Kinmond, and M. H. Brodsky, Appl. Phys. Lett. $\underline{28}$, 105 (1976).

88.  B. T. Debney, Solid State and Electronic Devices Special Issue, June 1978 S-15 (1978).

89.  Y. Hamakawa, H. Okamoto, and Y. Nitta, Appl. Phys. Lett. 35, 197, (1979); M. J. Thompson, J. Allison, M. M. Al-Kaisi, Solid State Electron Devices 2 (1978); B. Abeles, G. D. Cody, T. Tiedje, and C. R. Wronski, 21st Electronic Materials Conference, Boulder, CO, June 17, 1979.

90.  Y. Kuwano, J. Electron. Eng. 16, 65 (1979).

91.  H. J. Hovel, Semiconductors and Semimetals (Academic Press, New York, 1975) edited by R. K. Willardson and Albert C. Beer, Vol. 11 "Solar Cells."

92.  R. M. Schaffert, Electrophotography (Focal Press, New York, 1965.)

93.  A. Rose, Vision, Human and Electronic (Plenum Press, New York, 1973.)

94.  R. H. Batt, C. L. Braun, and J. F. Hornig, Appl. Opt. Suppl. (1969) p. 20.

95.  E. A. Davis and N. F. Mott. Philos. Mag. 22, 903 (1970).

96.  M. D. Tabak and P. J. Warter, Phys. Rev. 173, 899 (1968).

97.  D. M. Pai and S. W. Ing. Phys. Rev. 173, 729 (1968).

98.  E. A. Davis, J. Non-Cryst. Solids 4, 107 (1970).

99.  R. A. Street, Philos. Mag. 1337, 35 (1978).

100. T. M. Searle, T. S. Nashashibi, I. G. Austin, R. Devonshire, and G. Lockwood, Philos. Mag. 13, 39, 389 (1979).

101. D. Engemann and R. Fischer, Proceedings of the Fifth Int'l Conf. on Amorphous and Liquid Semiconductors, Garmisch-Partenkirchen (Springer, Berlin, 1973).

102. J. Frenkel, Soviet Tech. Phys. Lett., 5, 685 (1938).

103. G. Swartz and R. Williams, to be published.

104. I. Balberg and D. E. Carlson, Phys. Rev. Lett. 43, 58 (1979).

105. C. R. Wronski and T. Tiedge, 8th International Conference an Amorphous and Liquid Semiconductors, Cambridge, MA, Aug. 27-31, 1979.

106. W. E. Spear, P. G. LeComber, and A. J. Snell, Philos. Mag. 38, 303 (1978).

107. N. F. Mott and Gurney, Electronic Processes in Ionic Crystals (Dover Publications, New York, 1964) p. 179.

108. K. Hecht, Z. Phy. 77, 235 (1932).

109. H. C. Card and E. H. Rhoderick, J. Phys., D4, 1589 (1971).

110. R. J. Stirn and Y. C. M. Yeh, Appl. Phys. Lett. 27, 95 (1975).

111. M. A. Green, F. D. King and J. Shewchun, Solid-State Electron. $\underline{17}$, 551 (1974).

112. R. B. Godfrey and M. A. Green, Appl. Phys. Lett. $\underline{34}$, 790 (1979).

113. A. M. Goodman and J. M. Breece, J. Electrochem. Soc. $\underline{117}$, 982 (1970).

114. C. R. Wronski, D. E. Carlson, and R. E. Daniel, Appl. Phys. Lett. $\underline{29}$, 602 (1976).

115. W. A. Anderson, J. K. Kim, S. L. Hyland, and J. Coleman, Conf. Record of the 13th IEEE Photovoltaic Specialists Conf., Washington, DC, June 5-8, 1978, p. 755.

116. M. J. Thompson, J. Allison, M. M. Al-Kaisi, and I. P. Thomas, Proc. ESSDERC 78, Montpelier Revue de Physique Appliquée, 12, 1978.

117. D. E. Carlson, Annual Report prepared for DOE under Contract No. EY-76-C-03-1286, Sept. 1977.

118. J. H. Thomas III, to be published.

119. C. W. Magee, W. L. Harrington, and R. E. Honig, Rev. Sci. Instrum. $\underline{49}$, 477 (1978).

120. J. H. Thomas III and D. E. Carlson, to be published.

121. G. C. Clark, C. W. White, D. D. Allred, B. R. Appleton, C. W. Magee, and D. E. Carlson, Appl. Phys. Lett. $\underline{31}$, 582 (1977).

122. D. E. Carlson and C. W. Magee, 1979 Photovoltaic Solar Energy Conference, Berlin, April 23-26, 1979.

123. M. H. Brodsky, Thin Solid Films $\underline{40}$, L23 (1977).